AD-A016 259

MODELING OF CRATERING, CLOSE-IN DISPLACEMENTS, AND EJECTA

D. Maxwell, et al

Physics International Company

Prepared for:

Defense Nuclear Agency

16 July 1975

DNA 3628F

3041 H

MODELING OF CRATERING, CLOSE-IN DISPLACEMENTS, AND EJECTA

Physics International Company
2700 Merced Street
San Leandro, California 94577

16 July 1975

Final Report for Period 2 January 1974—30 August 1974

CONTRACT No. DNA C01-74-C-0151

THIS WORK SPONSORED BY THE DEFENSE NUCLEAR AGENCY
UNDER SUBTASK Y990AXSA001-52.

Prepared for
Director
DEFENSE NUCLEAR AGENCY
Washington, D. C. 20305

UNCLASSIFIED

SECURITY CLASSIFICATION OF THIS PAGE (When Data Entered)

REPORT DOCUMENTATION PAGE		READ INSTRUCTIONS BEFORE COMPLETING FORM
1. REPORT NUMBER DNA 3628F	2. GOVT ACCESSION NO.	3. RECIPIENT'S CATALOG NUMBER
4. TITLE (and Subtitle) MODELING OF CRATERING, CLOSE-IN DISPLACEMENTS, AND EJECTA		5. TYPE OF REPORT & PERIOD COVERED Final Report for Period 2 Jan 74–30 Aug 74
		6. PERFORMING ORG. REPORT NUMBER PIFR-659-2
7. AUTHOR(s) D. Maxwell and K. Seifert		8. CONTRACT OR GRANT NUMBER(s) DNA-001-74-C-0151
9. PERFORMING ORGANIZATION NAME AND ADDRESS Physics International Company 2700 Merced Street San Leandro, California 94577		10. PROGRAM ELEMENT, PROJECT, TASK AREA & WORK UNIT NUMBERS NWED Subtask Y99QAXSA001-52
11. CONTROLLING OFFICE NAME AND ADDRESS Director Defense Nuclear Agency Washington, D.C. 20305		12. REPORT DATE 16 July 1975 13. NUMBER OF PAGES 108
14. MONITORING AGENCY NAME & ADDRESS(if different from Controlling Office)		15. SECURITY CLASS. (of this report) UNCLASSIFIED 15a. DECLASSIFICATION/DOWNGRADING SCHEDULE

16. DISTRIBUTION STATEMENT (of this Report)

Approved for public release; distribution unlimited.

17. DISTRIBUTION STATEMENT (of the abstract entered in Block 20, if different from Report)

18. SUPPLEMENTARY NOTES

This work sponsored by the Defense Nuclear Agency under Subtask Y99QAXSA001-52.

19. KEY WORDS (Continue on reverse side if necessary and identify by block number)

20. ABSTRACT (Continue on reverse side if necessary and identify by block number)

The cratering flows observed in ten computed surface burst cases were modeled to predict time-dependent cratering, displacements, and ejecta. An elastic perfectly plastic material assumption was then used in conjunction with energy balance assumptions to predict final crater sizes and shapes and to expose the roles played by material strength and gravity. Reasonable agreements were found for a variety of cases.

DD FORM 1 JAN 73 1473 EDITION OF 1 NOV 65 IS OBSOLETE

UNCLASSIFIED

SECURITY CLASSIFICATION OF THIS PAGE (When Data Entered)

CONTENTS

CONTENTS (cont.)

ILLUSTRATIONS

ILLUSTRATIONS (cont.)

SECTION 1

INTRODUCTION AND OVERVIEW

1.1 BACKGROUND AND BASIS OF PRESENT STUDY

The present study was prompted as a result of various communications and publications of Cooper (Reference 1 for example). He correlated the close-in horizontal ground displacements of cratering experiments to the apparent crater volumes and suggested that his results were a manifestation of a late time, essentially incompressible flow phenomena that should be explained.

John Lewis* noted the existence of a large body of printout data corresponding to computer simulations of the early cratering flow that occurs before material strength effects appear. He suggested the possibility of discovering properties of these flows which could provide a basis for understanding Cooper's observations and the mechanics of cratering and ejecta to provide scaling rules and superior prediction methods. This is the basis of the computational, experimental, and correlative study that is reported here.

This study was initiated by DNA Contract DNA001-72-C-0063 and a draft final report was submitted in February, 1973. The results at that time were premature and a DNA document number

*Private communication from Mr. Lewis of DNA, presently at RDA.

was not assigned. The efforts were continued without DNA support and a first-order cratering flow model was developed by late 1973. This model, based on five surface burst computations, was in satisfactory agreement with limited experimental and computed data. DNA support returned in late 1973.

The primary objective of the present study was to assess and confirm the first-order flow model. This was accomplished satisfactorily. The second objective was to improve and extend the model to provide improved prediction methods and scaling rules for cratering, displacements, and ejecta. Substantial progress was made toward this objective.

Section 2 reports the steady-state flows that were observed in 10 surface burst cratering calculations and develops and assesses the first-order flow model. A few confirming examples are given. Many others were redundant and were omitted. No serious discrepancies were found.

Section 3 develops and applies an approximate energy balance model to freeze the cratering flow into the final crater size and shape by employing an elastic-perfectly plastic material assumption. Plasticene clay cratering data was predicted satisfactorily by this method. Other real materials appear to have very little shear strength along the flow paths that lead to the final crater radii, and the effect of gravity is significant in these cases.

Section 4 is a potpourri of data and considerations that relate to advanced models. Because the final model does not exist, it was not possible to organize this section in a satisfactory way. A large amount of data of unknown significance has been omitted.

Section 5 presents a summary and conclusion.

Appendix A reports the experimental program that was conducted in support of the theoretical and correlative efforts.

Appendix B gives some of the mathematical details that relate to the energy balance method of Section 3.

The remainder of this section will present an overview of Sections 2 and 3.

1.2 OBSERVATIONS AND MODELING OF STEADY-STATE CRATERING FLOW

Surprisingly simple cratering flows were observed in all cases that were examined. Steady-state flows in the earth (independent of time at a fixed point in space) were set up in the cratering region immediately after shock wave passage when the narrow stress pulse had relaxed and the material density approached its final constant value.

Mass continuity expressed as $\nabla \cdot \rho\vec{u} = 0$ could then be approximated by $\nabla \cdot \vec{u} = 0$ corresponding to incompressible flow. Then a steady-state approximation of one velocity component fixes the other. A first order flow model was constructed using this method.

The first order model employs two constant parameters; an intensity parameter, α, and a shape parameter, Z, to approximate the flow everywhere in space to predict average cratering response.

1.3 TERMINATION OF THE STEADY-STATE FLOW

The steady-state flow, established at a time, t_o, shortly after shock passage, was observed to persist for a long time which could be orders of magnitude larger than t_o (in the case of weak soil or sand). When material strength or gravity effects become significant, the flow slows markedly and stops without appreciably changing direction (Z remains constant). The final crater depth occurs first. The process of slowing and stopping occurs later at higher angles with the final crater radius occurring last.

The method that emerged to predict the termination of the flow employs stream tubes defined by adjacent steady-state stream lines. It is assumed that energy balance can be applied to the mass in a stream tube independent of the others. The kinetic and gravitational energies depend on the flow parameters α and Z. The distortional energy is more complicated and requires a material model. The distortional energies were evaluated by assuming a constant shear modulus, μ, and a constant von Mises yield stress, Y. The resulting expressions for kinetic, gravitational and distortional energies were then used to approximate energy conservation in the stream tube with the flow stopping when the kinetic energy was consumed.

Plasticene (children's modeling clay) is a reasonable approximation of a constant yield stress material (except for creep and temperature dependency) and it was employed in an experimental cratering program with three different explosive heights of burst, HOB. The corresponding values of α, Z obtained by short computer simulations resulted in good agreement between experimental and first-order model crater dimensions. However, few real earth media can be approximated properly with an elastic-perfectly plastic model and a more general method is required.

1.4 MATERIAL STRENGTH PROBLEM AND SOLUTION

Though it is obvious that most earth materials cannot be molded satisfactorily by a constant yield stress assumption, it is not known what models are appropriate for the shock conditioned, severely strained and failing material in the cratering flow. Stress-strain paths encountered in laboratory triax tests are far from those desired. It is thought that the state of the art for strength modeling of earth media is not satisfactory and a new approach must be taken to establish effective material strengths for the cratering process.

A straightforward and attractive solution is to invert the prediction formulas and use experimental crater depths and radii, D and RAD, to establish different effective yield stresses, Y_D and Y_{RAD} to account for the different stress-strain paths encountered in the crater depth and crater radius flows. A table of values of Y_D and Y_{RAD} for a spectrum of materials can be established in this way to provide a means of estimating the effective strengths of similar materials. The predictive methods then correspond to scaling rules where only the α,Z values of the new case are required.

SECTION 2

STEADY-STATE FLOWS, FIRST-ORDER MODELS

2.1 DISCUSSION

The computer simulations of Table 1 provided the bulk of the data that led to the flow models. The first 10 cases are surface bursts computed by two-dimensional, finite-difference codes. The eleventh case is a one-dimensional, spherical computation of PILEDRIVER, a deeply buried nuclear event. It is included to illustrate a feature.

Figure 1 shows schematic examples of a typical two-dimensional case showing an original grid configuration in the crater region and its distortion and velocity field at an intermediate time (after material densities return to a near constant value and before material strength effects appear).

Referring to the spherical coordinate system of Figure 1c, it was observed that the radial velocity was approximately independent of angle in the region below the original ground surface ($\theta \leq \pi/2$). It was also seen that this velocity could be approximated by

$$\dot{R} = \alpha/R^Z \tag{1}$$

Applying the incompressibility approximation, $\nabla \cdot \vec{u} = 0$, the tangential velocity component is

$$R\dot{\theta} = \dot{R}(Z - 2)\ \sin\theta/(1 + \cos\theta) \tag{2}$$

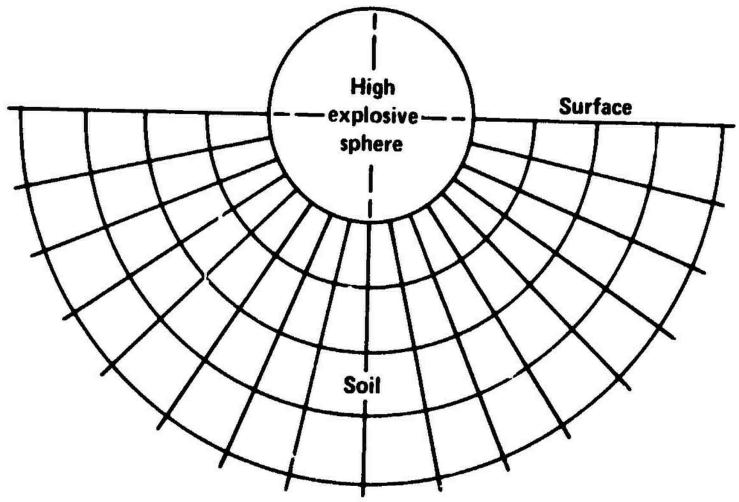

(A) Example of initial grid in crater region

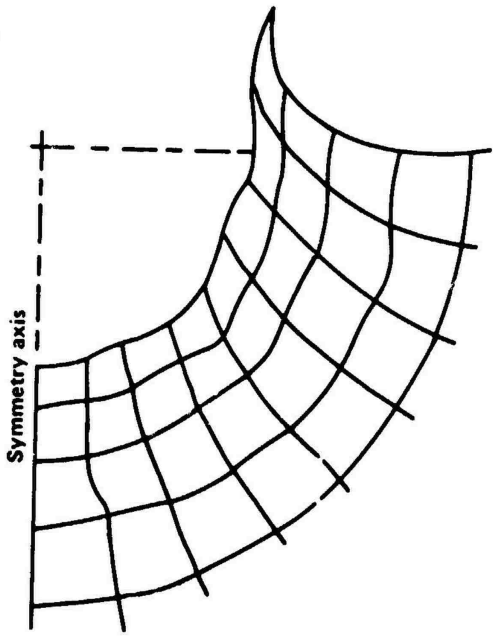

(B) Grid distortion at intermediate time

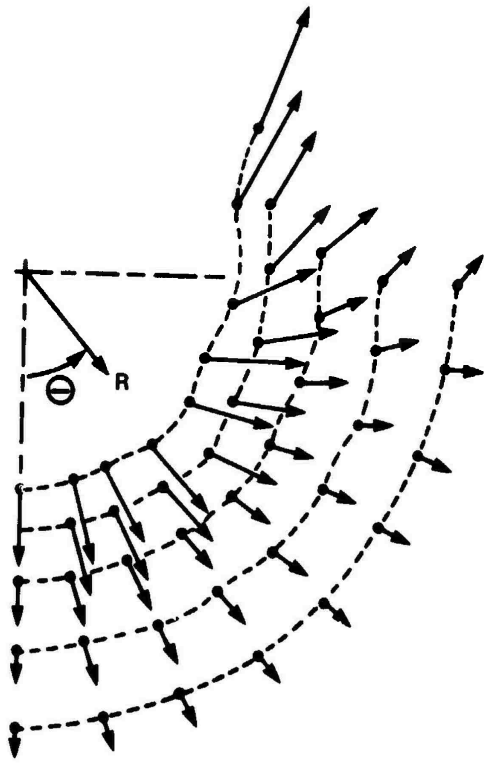

(C) Velocity vector field at intermediate time

Figure 1 Schematics of cratering computation.

TABLE 1

COMPUTER SIMULATIONS

Case	Name	Simulation
1	ELK 64	JOHNIE BOY, 500-ton nuclear event. DOB = 1.9 feet in NTS Area 18 alluvium
2	ELK 67	Z-C6, Plasticene crater experiment scaled to 1 cm radius HE sphere. $HOB/R_{HE} = 0$ (half-buried sphere)
3	ELK 66	Z-C2, same as above except $HOB/R_{HE} = 1$ (tangent sphere)
4	ELK 69	Z-C7, same as above except $HOB/R_{HE} = 2$
5	ELK 65	CACTUS, 17-kt nuclear surface burst over 5.5 feet of coral sand overlaying beachrock
6		NOT DISCUSSED
7	ELK 73	5-Mt nuclear surface burst over layered site of shale and limestone
8	ELK 76	Same as above with slightly enhanced energy due to neutron deposition
9	ELK 70(L)	Surface pressure loading function P(R,t) over coral sand layers with low porosity.
10	ELK 75(H)	Same as above with high porosity layers
11	PILEDRIVER	PILEDRIVER, 61-kt nuclear source buried in granite at 121-bar overburden depth.

The particle motion in this velocity field is

$$R^{Z+1}(t) - R_o^{Z+1} = R_c^{Z+1}(t) = (Z+1)\alpha(t - t_o) \qquad (3)$$

$$\frac{1 - \cos\theta(t)}{1 - \cos\theta_o} = [R(t)/R_o]^{Z-2} \qquad (4)$$

where r_o, θ_o are the particle coordinates at t_o. In most cases of interest the onset time is small and the displacement accumulated during shock passage is negligible. Then $t_o \approx 0$ and R_o and θ_o can be approximated by the undisturbed coordinates of the particle. $R_c(t)$ is defined as the radius of a hypothetical particle that originated at $R_o = 0$. It corresponds to the radius of a crater wall point when no mass has been lost by vaporization or excavation to implant the explosive source.

The steady state equations (1-4) were compared to Table 1 cases and good agreement was observed. A few examples will be presented.

2.1.1 Radial Velocity. Equation (1) was a reasonable approximation of the steady state radial velocity that was observed in all cases. Two cases are reported as examples.

Case 11, PILEDRIVER, was spherically symmetric corresponding to Z = 2. The computed radial velocity $\dot{R}$ versus R at various times is displayed in Figure 2. The narrow propagating peak corresponding to the shock wave can be seen. The transition to approximate steady state flow occurs immediately behind the narrow shock with Equation (1) being an excellent model until slightly after 100 msec when material strength and overburden effects become significant.

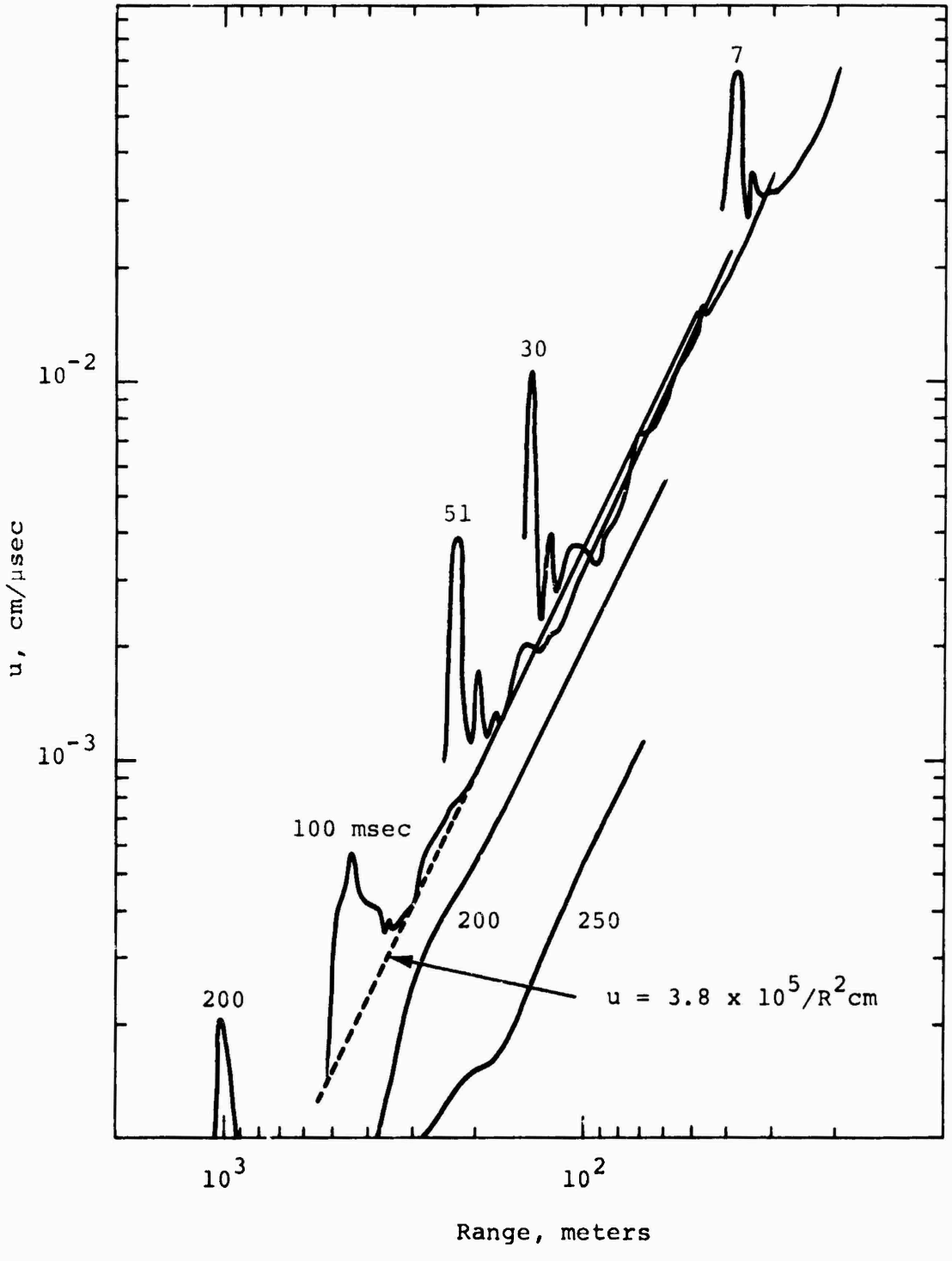

Figure 2 Code result for PILEDRIVER material velocity versus range at indicated times.

A one-dimensional representation of R versus R can also be constructed for the two-dimensional flows in the manner given next.

Referring to Figure 1, let S_i be any of the original hemispherical surfaces that surround ground zero. The volume <u>below</u> the original ground plane and <u>inside</u> S_i is

$$V_i(t) = \frac{2\pi}{3} \int_0^{\pi/2} \int_0^{R_i(\theta,t)} R_i^2(\theta,t) dR_i \sin\theta \, d\theta \tag{5}$$

Similarly, the rate of change of volume $\dot{V}_i(t)$ can be evaluated. The corresponding average radius and radial velocity are then defined.

$$\bar{R}_i = \left(\frac{3}{2\pi} V_i\right)^{1/3} \tag{6}$$

$$\dot{\bar{R}}_i = \dot{V}_i/(2\pi\bar{R}^2) \tag{7}$$

In Case 1, JOHNIE BOY, the original hemispherical grid lines with R_o (meters) = 3.6, 3.8, 4.0, 4.2, ···, were examined at various intermediate times after shock passage and values of $\bar{R}_i$ and $\dot{\bar{R}}_i$ were constructed. The results are displayed in Figure 3. The notations 3.6, 3.8, etc., refer to the value of R_o. Points ahead of and in the shock wave are omitted for clarity. The agreement with Equation (1) is good until shortly after 100 msec.

This method of constructing average values of α and Z was also used for Cases 2 to 5. The results are listed in Table 2.

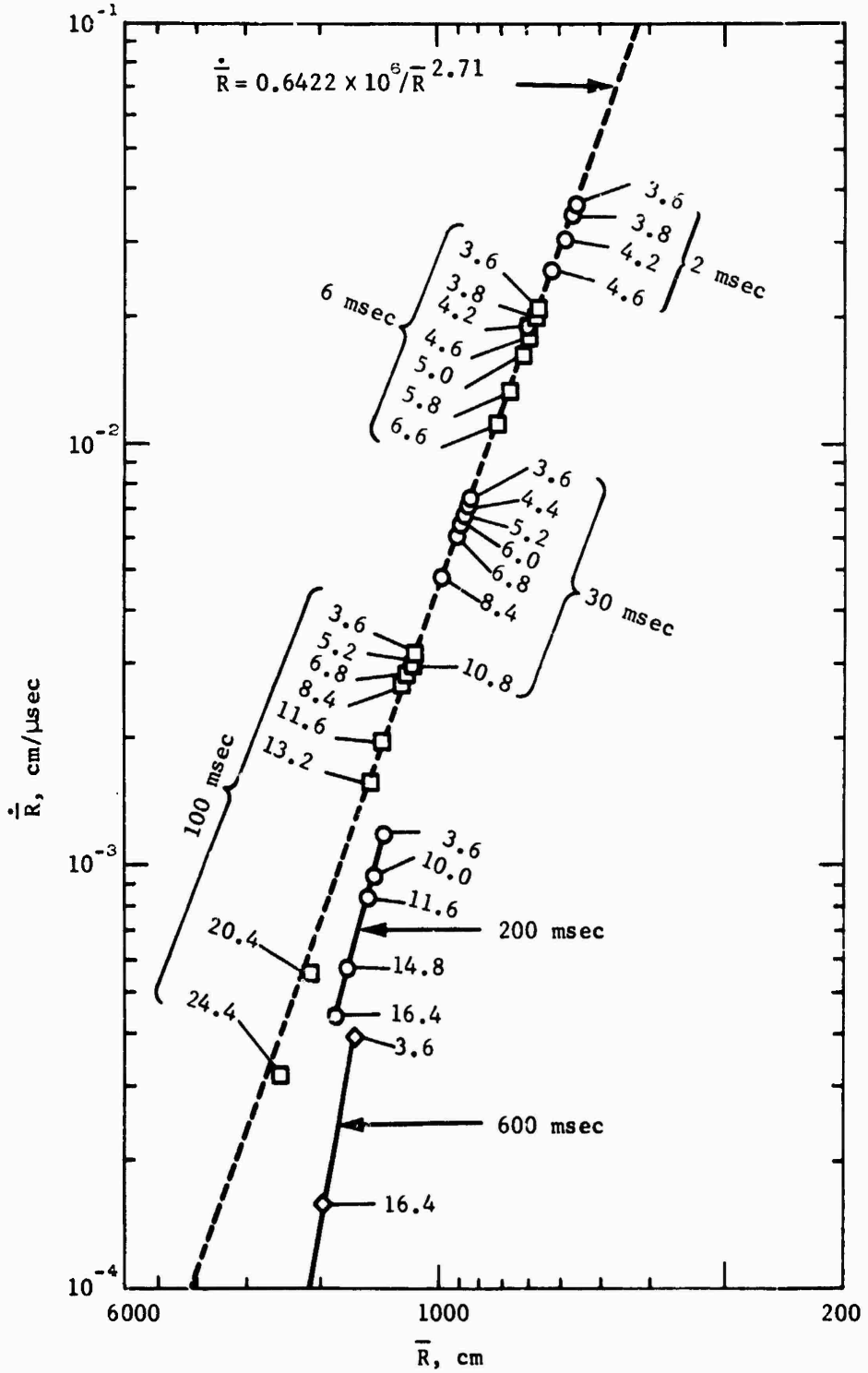

Figure 3 Case 1. $\dot{\bar{R}}$, $\bar{R}$ points at indicated times for various reference surfaces with indicated initial radii (meters).

TABLE 2

AVERAGE VALUES OF α AND Z CONSTRUCTED BY VOLUME METHOD

Case	Name	α ($cm^{Z+1}/\mu sec$)	Z
1	500-ton JOHNIE BOY	0.6422×10^6	2.71
2	Plasticene HOB = 0	0.563	3.0
3	Plasticene HOB = 1	0.151	3.0
4	Plasticene HOB = 2	0.0405	2.7
5	17-kt CACTUS	2.1×10^6	2.75
11	61-kt PILEDRIVER	3.8×10^5	2.0

2.1.2 Velocity Field. Space-averaged values of α and Z used in Equations (1) and (2) correspond to the first-order model of the steady-state flow field. This model was in fair agreement with the observed data in all cases with the largest discrepancies near the surface. Two cases are given next as examples.

Figure 4 displays Case 1, JOHNIE BOY velocity vectors at selected points and selected times as indicated by the symbols and solid arrows. Only a few of the many points are shown. The dashed arrows are the model velocities constructed from Equations (1) and (2) and the average values of α and Z from Table 2. Though the overall agreement is satisfactory, there is a definite tendency to the discrepancies. The model vectors point above the computed vectors at low angles and below the computed vectors at high angles. Z, the flow shape parameter, has an angular dependency. Its radial and time dependency, if present, is not obvious.

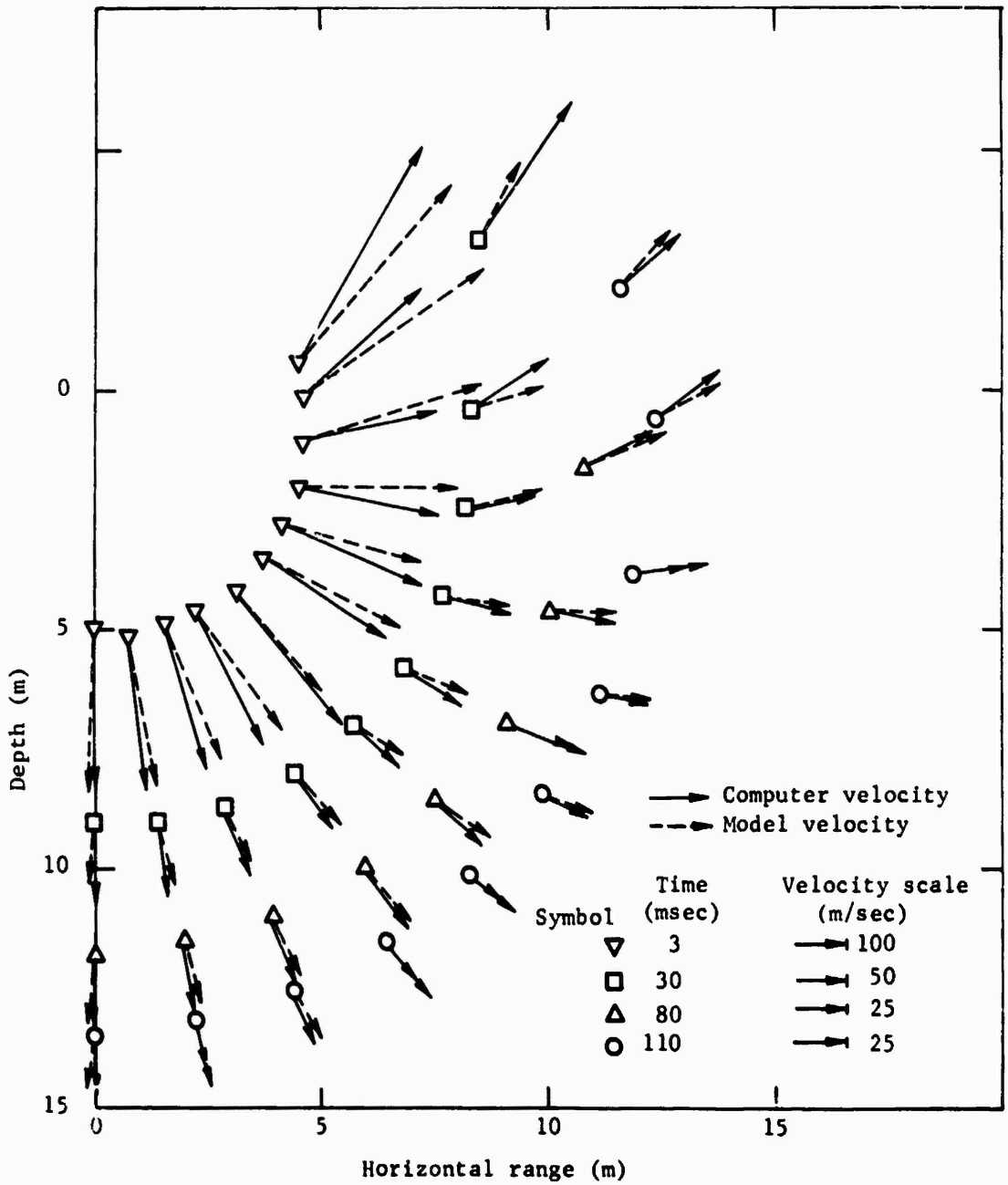

Figure 4 Case 1. Equation (2) velocities (dashed arrows) compared to computed velocities (solid arrows) at selected points and times.

The layered Case 5, CACTUS, is chosen for a similar display. The velocity fields are shown in Figure 5. The discrepancies are similar to those of the unlayered case discussed above and the same remarks apply.

2.2 STREAM LINES AND DISPLACEMENT FIELD

The stream lines modeled by Equations (3) and (4) are shown in Figure 6 for Z = 2.71. This model is clearly non-physical at high angles where the stream lines become vertical and then curve back to the symmetry axis.

The time dependent displacements of selected points at various times are displayed in Figure 7 for Table 2, JOHNIE BOY values of α and Z. The very thin ejecta lip shape cannot be expected to occur for a variety of physical reasons. The smoother portions of the surface upthrust were in satisfactory agreement with the computer-simulated counterpart.

2.2.1 Trajectories. The steady-state velocity vector fields prescribe the particle trajectories and a satisfactory model of one necessarily is satisfactory for the other. One trajectory example will be displayed, however, to validate an approximation used later. The approximation is that the stream tubes, defined by adjacent stream lines, do not interact so that the flow stopping in one does not change the direction of the others. This assumption decouples the flow that defines final crater depth (which occurs first) from that of the final crater radius (which can occur much later).

The time-dependent crater profile of Case 1, JOHNIE BOY, is shown at various times in Figure 8. The final crater depth is reached in about 200 msec with the final radius occurring at

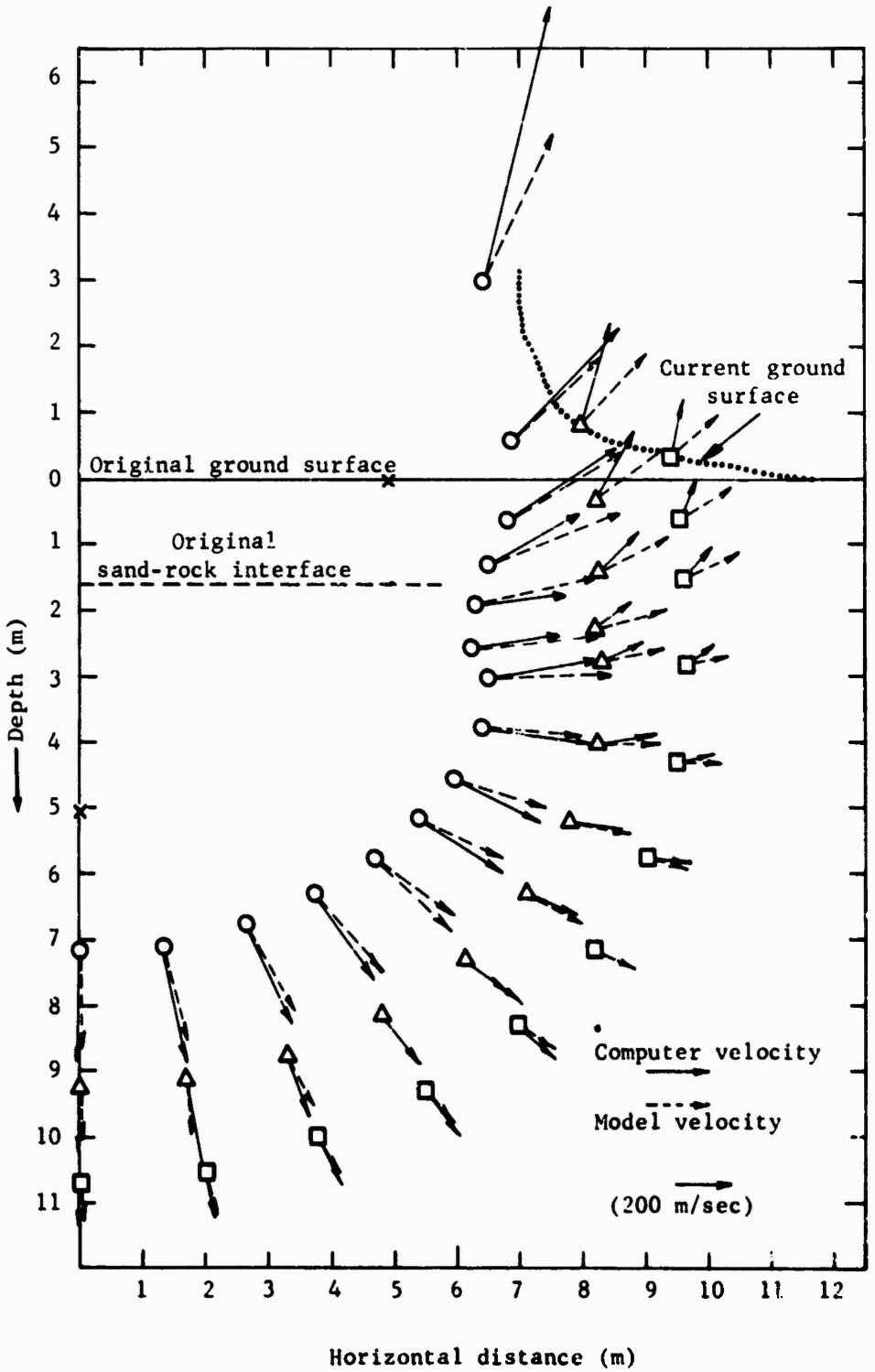

Figure 5 Case 5. Equation (2) velocities (dashed arrow) compared to computed velocities (solid arrows) at selected points at 5 msec.

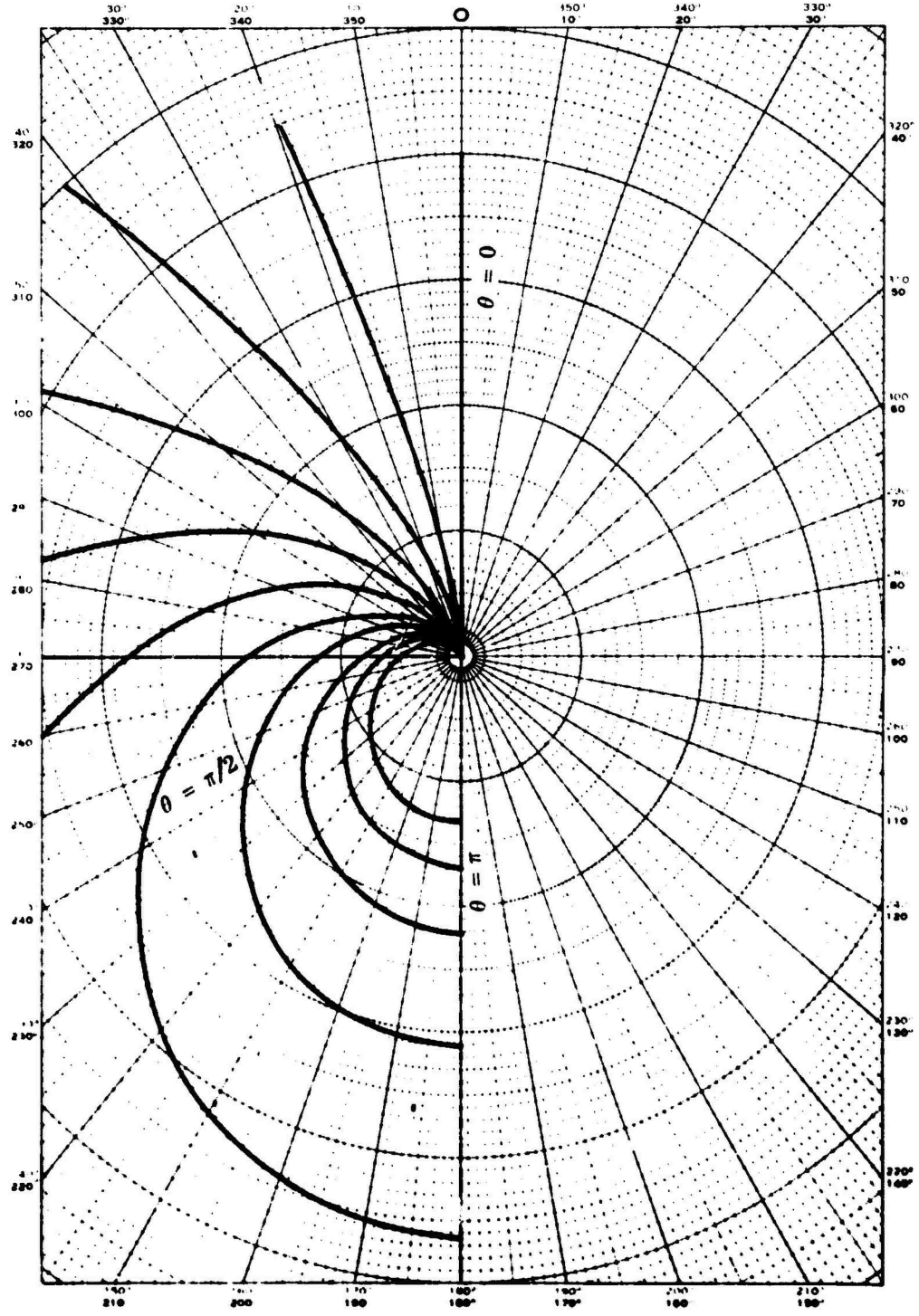

Figure 6 Model streamlines for z = 2.71.

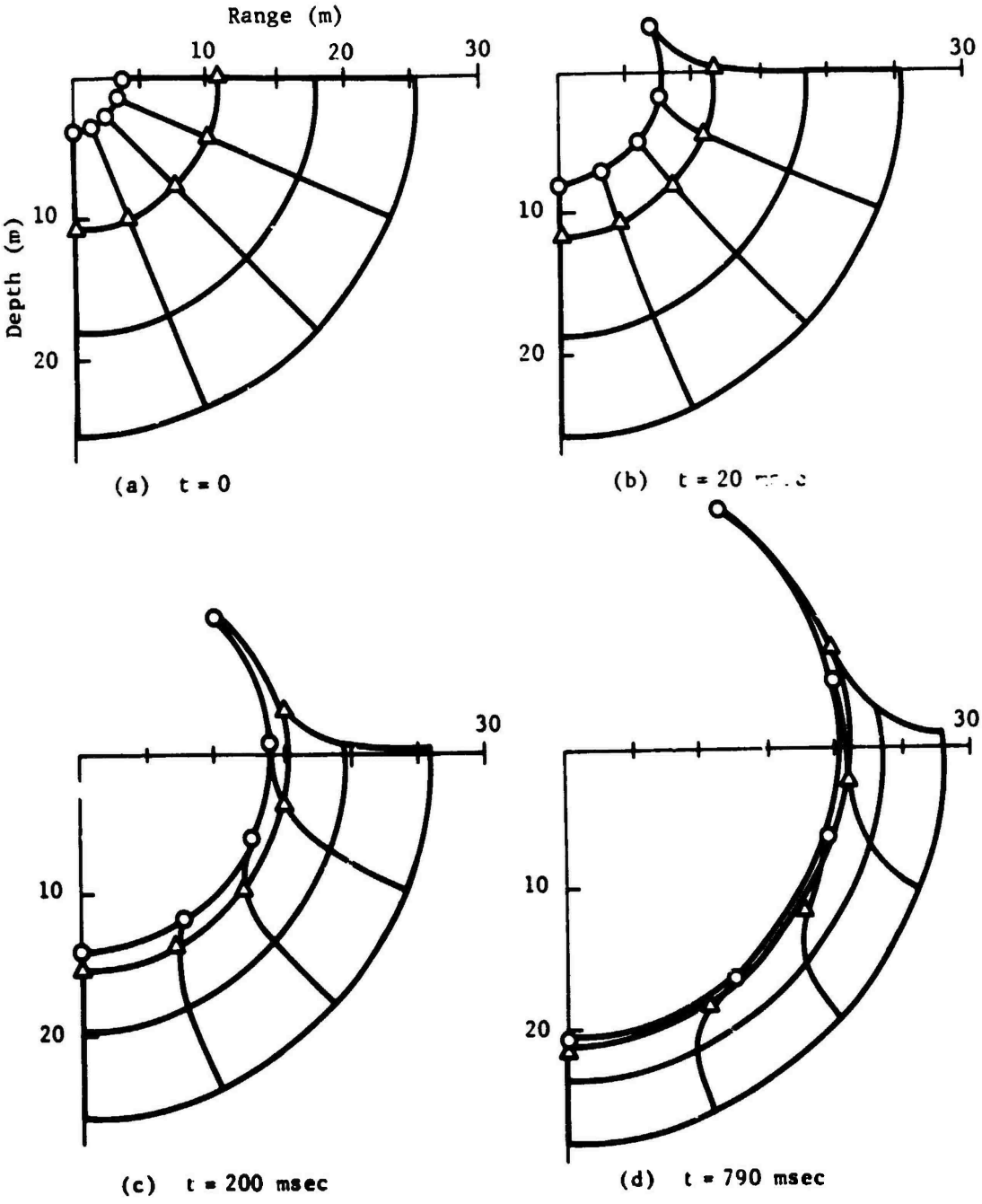

Figure 7 Progressive stages of cratering by Equation (3) model (see text).

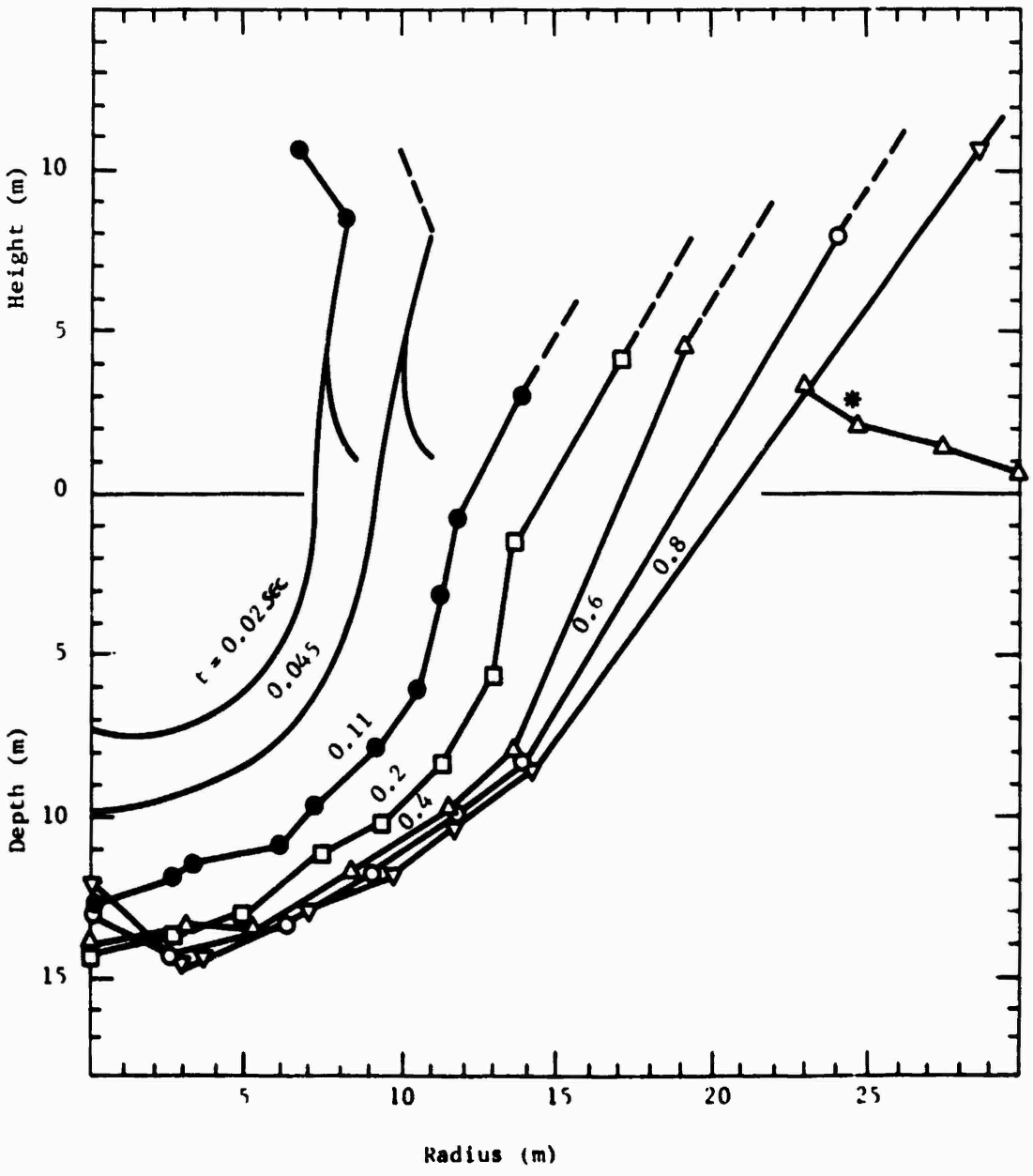

Figure 8 Case 1. Computed crater profiles at indicated times (seconds).

about 800 msec. The trajectories of points on the crater wall and inside the crater wall were examined and were found to agree satisfactorily to the Equations (3) and (4) model when the constant α, Z values of Table 2 were employed. Figure 9 displays this comparison for particles that originated at a spherical radius of 10 meters. As expected, the discrepancies are consistent with those of the velocity fields of Figure 4. The computed particle radii at 200 msec are in good agreement with the model. Material strength effects then appear and the computed motion slows and stops, first in the crater depth region ($\theta \simeq 0$) and later at higher angles. The particles do not depart substantially from their steady-state streamlines during the termination of the flow.

2.3 EJECTA

The steady-state flow approximation applied at the surface ($\theta = \pi/2$) can be used to model the process of mass ejection through this surface. Figures 10a and 10b are schematics showing the surface velocity vectors and the vertical components at a time t_1. Figures 10c and 10d are corresponding displays at a later time, t_2. The flows are identical in regions where mass is present.

It is convenient to define a vertical velocity cutoff, $\dot{x}_{cut}$, to identify mass that is ejected with vertical velocities equal to or greater than a prescribed value. The following definitions and expressions are used:

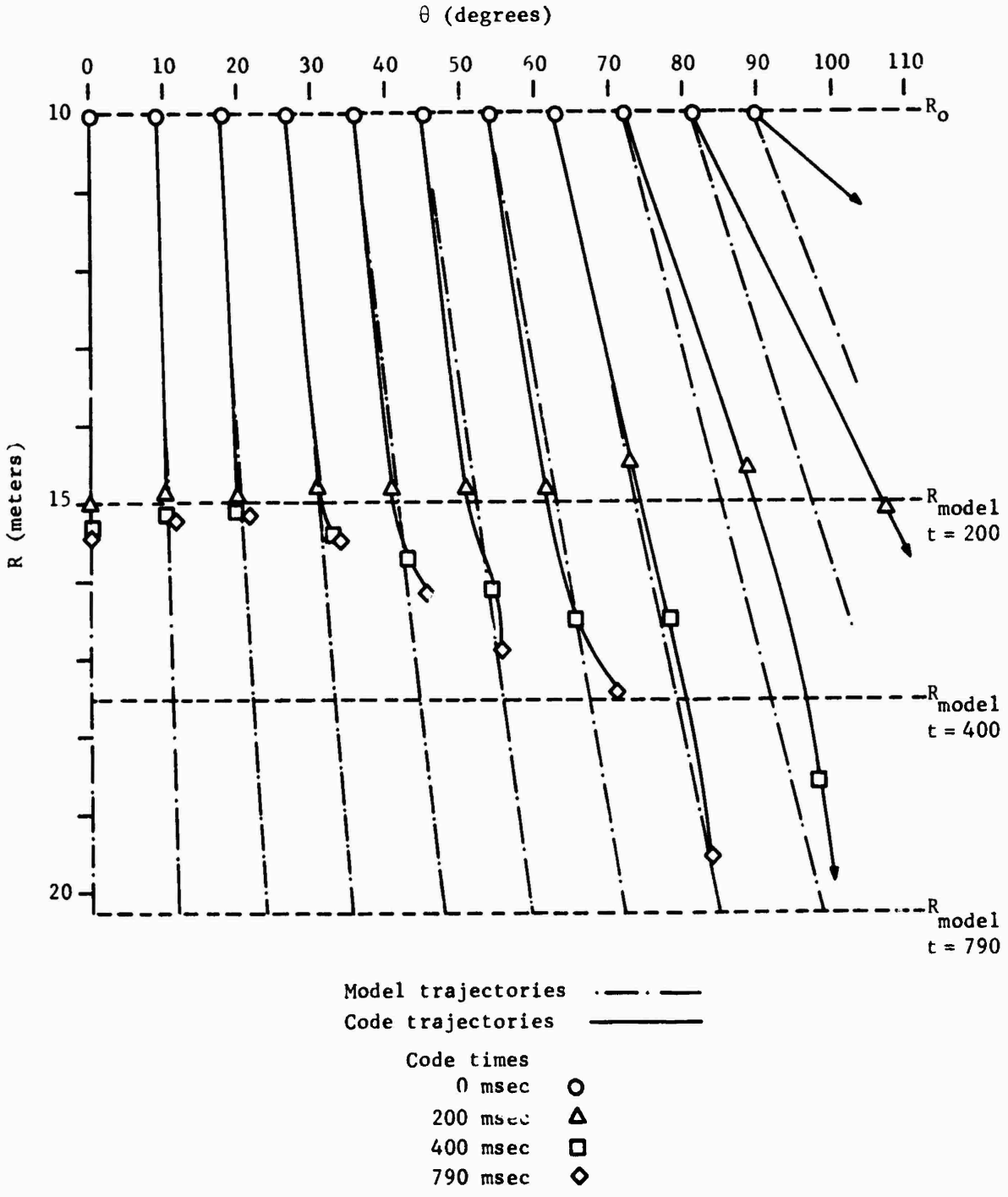

Figure 9 Comparison of model trajectories and computed results for Case 1 (see text).

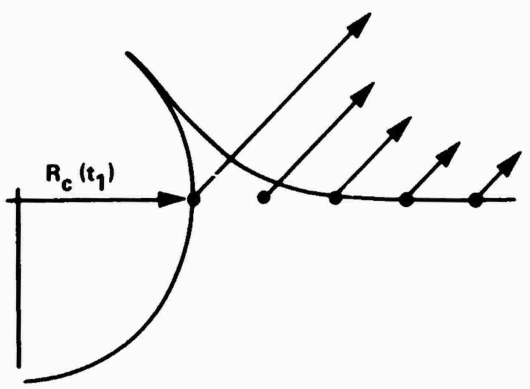

(A) Surface velocities at t_1

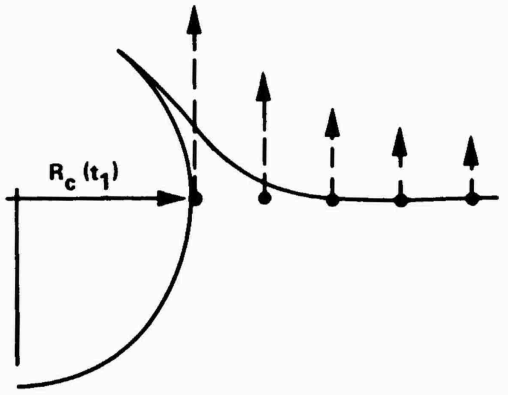

(B) Surface vertical velocity components at t_1

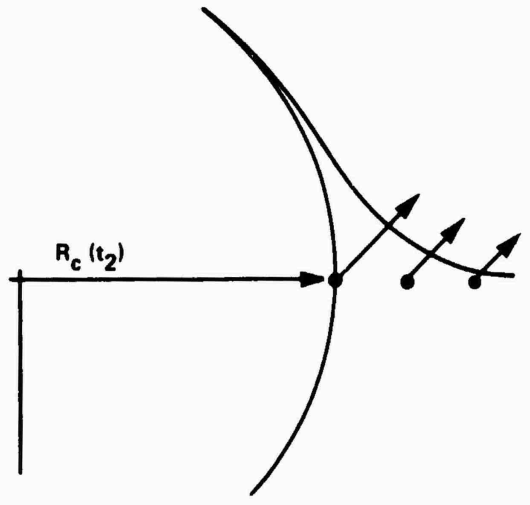

(C) Surface velocities at t_2

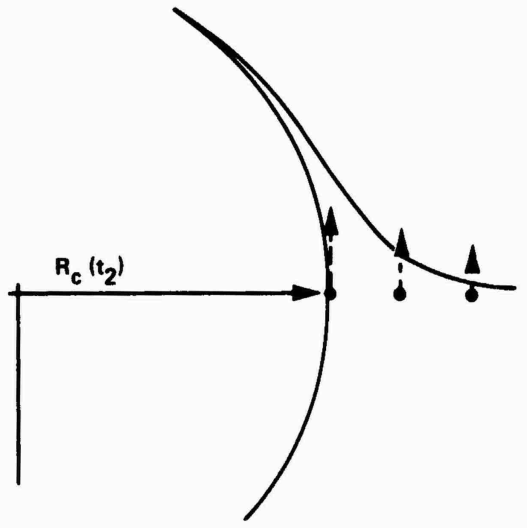

(D) Surface vertical velocity components at t_2

Figure 10 Schematics of surface ejection sequence.

ρ = average density during ejection

$\dot{x} = (Z - 2)\,\alpha/R^Z$ = steady-state vertical velocity at $\theta = \pi/2$

$\dot{y} = \alpha/R^Z$ = steady-state horizontal velocity at $\theta = \pi/2$

$\phi = \tan^{-1}(Z - 2)$ = ejection angle measured from horizontal

$\dot{x}_{cut}$ = reference cutoff for vertical velocity

$R_{cut} = (Z - 2)\,\alpha/\dot{x}_{cut}^{\,1/Z}$ = radius at which $\dot{x}_{cut}$ occurs

$R_c(t) = \left[(Z + 1)\,\alpha t\right]^{1/(Z+1)}$ = crater radius at time t

RAD = final crater radius, known or estimated

$t_f \cong RAD^{Z+1}/[(Z + 1)\,\alpha] \cong$ time of final crater

The steady-state velocity expressions are not valid when R_c approaches RAD (or t approaches t_f). In particular, the velocities are 0 at $t = t_f$ and ejection stops. However, the mass ejected with velocities $\dot{x} \geq \dot{x}_{cut}$ is unaffected by the final crater size or final crater time provided that $R_{cut} < RAD$. This is the reason why R_{cut} and x_{cut} are particularly useful parameters.

A variety of ejecta expressions can be derived by simple integrations. Three of these will be given as examples. The explicit time dependencies in these ejecta expressions are replaced by the more convenient parameter, $R_c(t)$. Similarly, $\dot{x}_{cut}$ is replaced by R_{cut}.

$\dot{M}(\dot{x}_{cut},t) = \dot{M}(R_{cut},R_c)$ = rate of mass ejection at time t with $\dot{x} \geq \dot{x}_{cut}$

$M(\dot{x}_{cut},t) = M(R_{cut},R_c)$ = mass ejected up to time t with $\dot{x} \geq \dot{x}_{cut}$

$M(\dot{x}_{cut}, t_f) = M(R_{cut},RAD)$ = total mass ejected with $\dot{x} \geq \dot{x}_{cut}$

The results are

$$\dot{\dot{M}}(\dot{x}_{cut},t) = \frac{2\pi\rho\alpha}{R_c^{Z-2}}\left[1 - \left(\frac{R_c}{R_{cut}}\right)^{Z-2}\right] \quad R_c \leq R_{cut} \tag{8}$$

$$\dot{M}(\dot{x}_{cut},t) = 2\pi\rho\,\frac{R_c^3}{3}\left[1 - \left(\frac{3}{Z+1}\right)\left(\frac{R_c}{R_{cut}}\right)^{Z-2}\right] R_c \leq R_{cut} \tag{9}$$

$$\dot{M}(\dot{x}_{cut},t_f) = 2\pi\rho\,\frac{R_{cut}^3}{3}\left[1 - \left(\frac{3}{Z+1}\right)\right], \quad R_{cut} \leq RAD \tag{10}$$

These expressions do not discriminate between the surface upthrust mass (which stays in contact with the earth at all times) and the true ejecta which is lofted on ballistic trajectories. However, it can be shown that Equation (10) essentially predicts the lofted mass when R_{cut} = RAD. The upthrust mass is then the difference between the total mass displaced by the crater and the lofted mass.

Only Case 1 (JOHNIE BOY) and Case 8 (ELK 76) were computed to final crater time to provide enough ejecta data for sensitive comparison to Equation (10). The agreements were fair when volume averaged α and Z values were used (first-order model) and would be improved if surface average values of α and Z were used.

The comparisons for JOHNIE BOY, with the α and Z values of Table 2, will be displayed. Recalling previous remarks, the JOHNIE BOY velocity vectors were above those of the first-order model at high angles (see Figure 4). Then at a cutoff range,

R_{cut}, the ratio $\dot{x}/\dot{y}$ will not equal the volume average value $Z - 2$. Therefore, the expressions $M(\dot{x}_{cut}, t_f)$ and $M((Z-2)\dot{y}_{cut}, t_f)$ are not identical and it is instructive to compare both to the computed data.

The model results are shown as the dashed line in Figure 11. The circle points were obtained summing the computed ejecta mass with the constraint $\dot{x} \geq \dot{x}_{cut}$. The diamond points correspond to the sum with $\dot{y}(Z-2) \geq \dot{x}_{cut}$. The large discrepancies that occur above velocities of about 10^{-2} may be due to spall and the associated error in the constant density assumption. Otherwise the discrepancies between the model and either of the expressions is less than a factor of 2 in mass at a fixed $\dot{x}_{cut}$.

It should be noted that the results of Figure 11 can be displayed in a variety of ways, each answering different questions. For example, the amount of mass ejected up to time t can be obtained by replacing $\dot{x}_{cut}$ with

$$\dot{x} = \alpha/R_c^{Z} = \alpha/\left[(Z+1)\alpha t\right]^{Z/(Z+1)}$$

and Equation (9) can be verified. Similarly, the amount of mass ejected between $\dot{x}_1$ and $\dot{x}_2$, or R_1 and R_2, or t_1 and t_2 can be obtained.

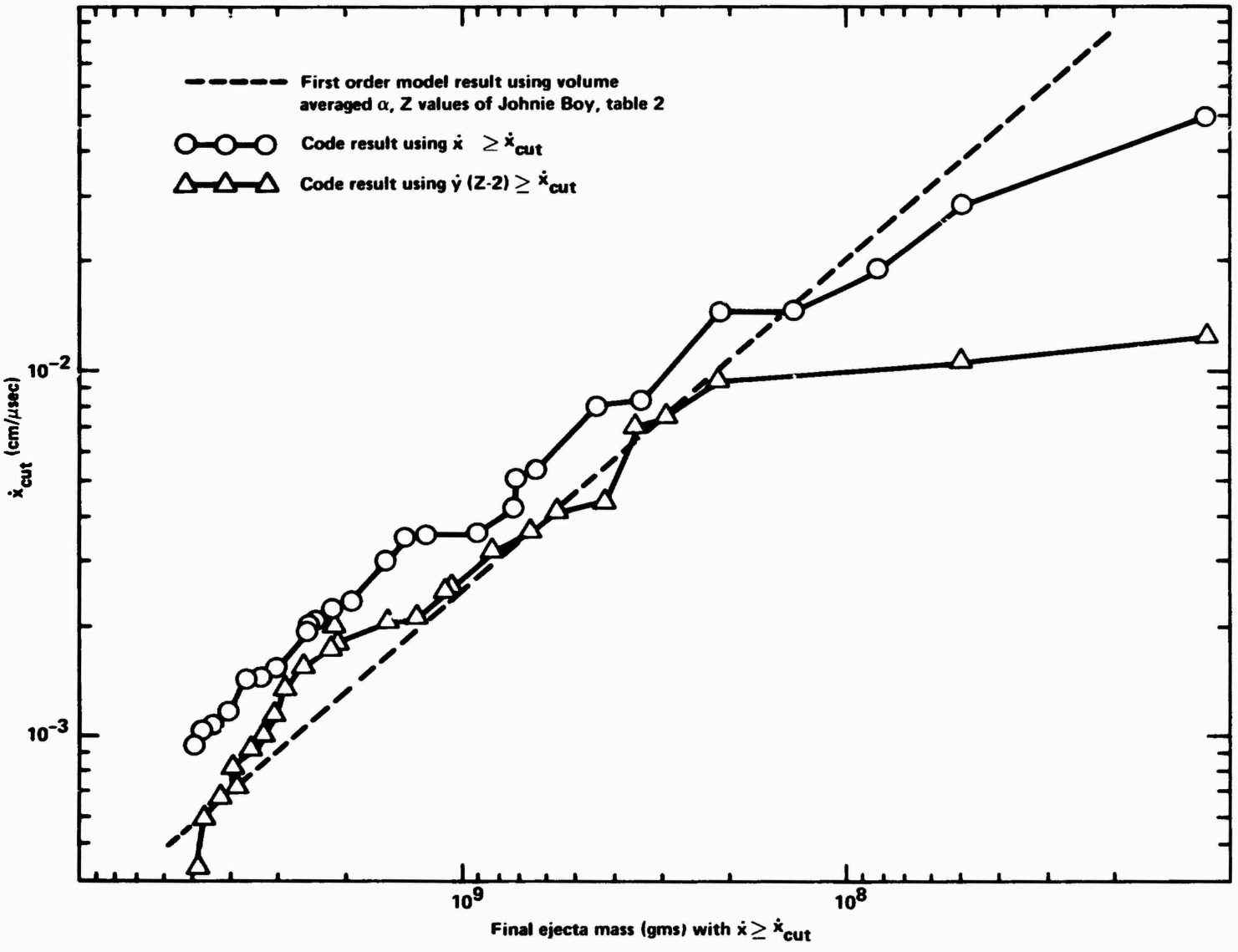

Figure 11 Equation (10) results compared to computed JOHNIE BOY ejecta.

The experimental measurements of the JOHNIE BOY crater are:

R_a = 21 meters = apparent crater radius

R_T = 22 meters = true crater radius

V_e = 4900 m^3 = ejecta volume (including fallback but excluding upthrust)

The ejecta bulk density was about 25 percent less than that of the in situ soil. Then the ejecta volume predicted by Equation (10) is

$$V_e = 1.25 \quad \frac{2\pi}{3} R^3_{final} \left[1 - \frac{3}{2.71+1}\right] = 0.5R^3_{final}$$

$$= 4630 \ m^3 \text{ for } R_a$$

$$= 5324 \ m^3 \text{ for } R_T$$

where is in good agreement with the measured value with either choice of crater radius.

SECTION 3

ENERGY BALANCE AND FINAL DIMENSIONS

The final displacement model assumes that the stream line directions do not change when the flow slows and that energy balance approximations can be applied independently in each stream tube to stop the flow. The final configuration of the mass in the various stream tubes then defines the final crater and displacement field. This process is shown schematically in Figure 12. The method is described next.

The kinetic energy, KE, the gravitational energy, GE, and the total distortional energy, DE, in the steady state flow model are expressed as a function of R_c, the inner radius of the mass in a stream tube. The total energy in the stream tube is estimated by first defining the condition

$$KE(R_c^+) = GE(R_c^+) + DE(R_c^+). \qquad (11)$$

The value of R_c^+ is obtained from Equation (11) and is used to estimate the total energy, E_o.

$$E_o = \text{constant} = KE(R_c^+) + GE(R_c^+) + DE(R_c^+). \qquad (12)$$

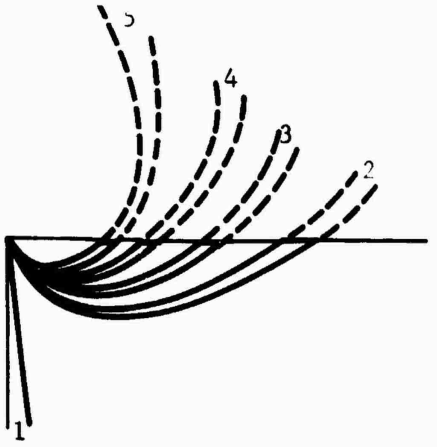

(a) Initial configuration

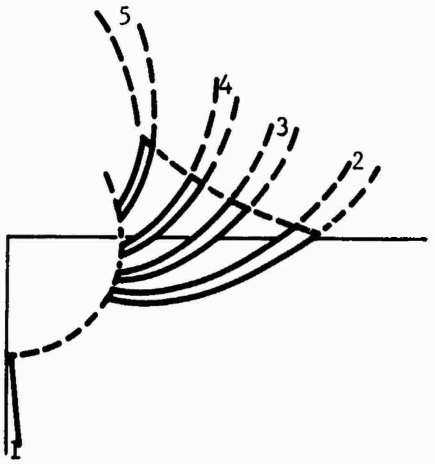

(b) Stream tube 1 flow stops, defining crater depth

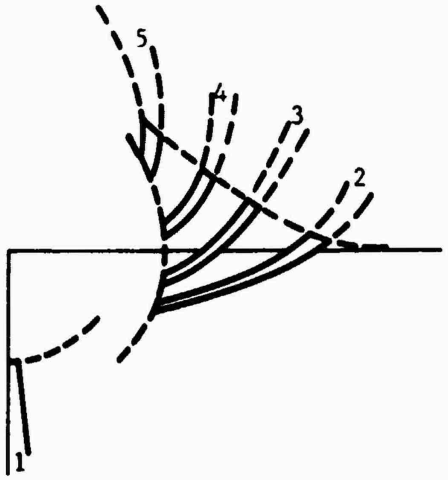

(c) Stream tube 2 flow stops defining another final crater vector

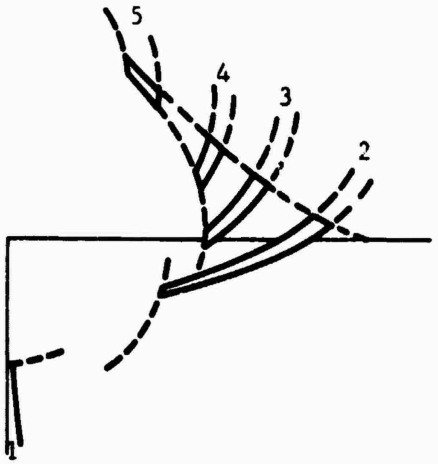

(d) Stream tube 3 flow stops, defining crater radius and another upthrust point

Figure 12 Schematic configurations of mass inside various stream tubes. a, b, c, and d correspond to increasing times.

The final inner radius, R_f, of the mass in the tube is then evaluated at the condition

$$GE(R_f) + DE(R_f) = E_o. \tag{13}$$

This method was applied to two stream tubes: the axis tube (in which case R_f is the final crater depth), and the crater radius tube (in which case R_f = RAD). The latter tube was defined by the condition that the final angle θ_c equals $\pi/2$ consistent with the usual definition of crater radius.

The mathematical development associated with $KE(R_c)$, $GE(R_c)$, and $DE(R_c)$ is given in Appendix B and only selected features and results are presented here. The distortional energy assumptions are the most severe, and require a constant yield stress approximation to obtain a closed-form solution.

3.1 THE CRATER DEPTH AND RADIUS MODEL

The Appendix B model predicts the crater depth

$$D = \alpha^{1/Z} \gamma_a^{1/(2Z)} \tag{14}$$

where

$$\gamma_a = \frac{0.5\rho/(Z-1)}{\frac{Y Z 6}{(Z+1)^2}\left(\frac{1}{2}\right)^{2Z/(Z+1)} + \frac{D\rho g}{(Z+2)}\left(\frac{1}{2}\right)^{(2Z+1)/(Z+2)}}$$

The corresponding expressions for crater radius are

$$RAD = \alpha^{1/Z} \gamma_b^{1/(2Z)} \tag{15}$$

where

$$\gamma_b = \frac{0.2\rho \left[1+(Z-2)^2\right]/(Z-1)}{0.275 \frac{Y Z 6}{(Z+1)^2}\left(\frac{1}{2}\right)^{2Z/(Z+1)} + RAD \frac{c\rho g}{(Z+2)}\left(\frac{1}{2}\right)^{(2Z+1)/(Z+2)}}$$

and

$$\varepsilon = 0,\ 0.158,\ 0.268,\ 0.349,\ \text{and } 0.41,\ \text{respectively}$$

for

$$Z = 2,\ 2.5,\ 3,\ 3.5,\ \text{and } 4.$$

Velocity Cutoff--Cauchy and Froude Scaling

The steady state velocities that existed at the pc .tions D and RAD before strength and gravity slow the flow are

$$\dot{D} = \alpha/D^Z = 1/\sqrt{\gamma_a} \tag{16}$$

$$\dot{RAD} = \alpha/RAD^Z = 1/\sqrt{\gamma_b} \tag{17}$$

It can be verified that γ_a and γ_b have no dependency on α if the gravity term can be neglected. Then Equations (16) and (17) predict that all cratering flows with the same shape (Z) will freeze at the same cutoff velocities. This is consistent with Cauchy scaling.

When the gravity term dominates, then the cutoff velocities are proportional to the square root of the depth (or radius). This is consistent with Froude scaling.

3.2 CORRELATION OF DATA BY VELOCITY CUTOFF

Before surface burst cratering data are displayed in the velocity cutoff representation, it is necessary to note some qualifications of Table 1 cases.

(a) Case 1, JOHNIE BOY has reliable experimental crater data, apparent and true. The computation employed a weak strength model with a 1.6-bar cohesion that vanished in the regions of surface spall. The computed crater radius was satisfactory. The computed depth was about 40 percent too deep.

(b) Cases 2, 3, and 4 had reliable experimental crater data. The measured value of the plasticene yield strength at atmospheric pressure was about one bar (at the 76°F ambient temperature of the experiments), with a large error due to creep and a large temperature dependency. The calculations were terminated when about 60 percent of the energy coupling to the ground was not complete. The subsequent errors in α and Z values are not known.

(c) Case 5, the CACTUS crater dimensions were measured after some water action and have unknown reliability except that the depth and radius measurements are thought to correspond respectively to minimum and maximum limits. The final crater was not computed.

(d) Cases 7 and 8 were very similar and will not be distinguished. There is no experimental data. The computed crater dimensions were dominated by yield models with yield strengths that were very large compared to the successful JOHNIE BOY model in the low pressure, highly strained region of the cratering flow.

Cases 9 and 10 have no crater data and Case 11 is not a surface burst. These will not be displayed.

(e) A dry sand cratering experiment (Z-S1 of Appendix A, Table A1) was conducted in the scaled geometry of Case 3 (plasticene with HOB = 1). The flash X-ray photographs of the time-dependent ejecta lips were identical in the same scale. Therefore, the α,Z values of Case 3 were scaled to the size of the sand experiment and the sand crater depth and radius are included as data.

The cutoff velocity results for all of the above cases are displayed in Figure 13. The various lines and symbols are explained next.

(a) The slanted solid lines correspond to the steady state radial velocities using the volume average values of α and Z.

$$\dot{R} = \alpha/R^Z$$

(b) The dashed lines labeled $\dot{D}(Y)$ and $\dot{RAD}(Y)$ are the Equations (16) and (17) cutoff velocities as a function of Y in bars for the case Z = 3, ρ = 2. $\dot{D}(0)$ and $\dot{RAD}(0)$ are the gravity controlled limits.

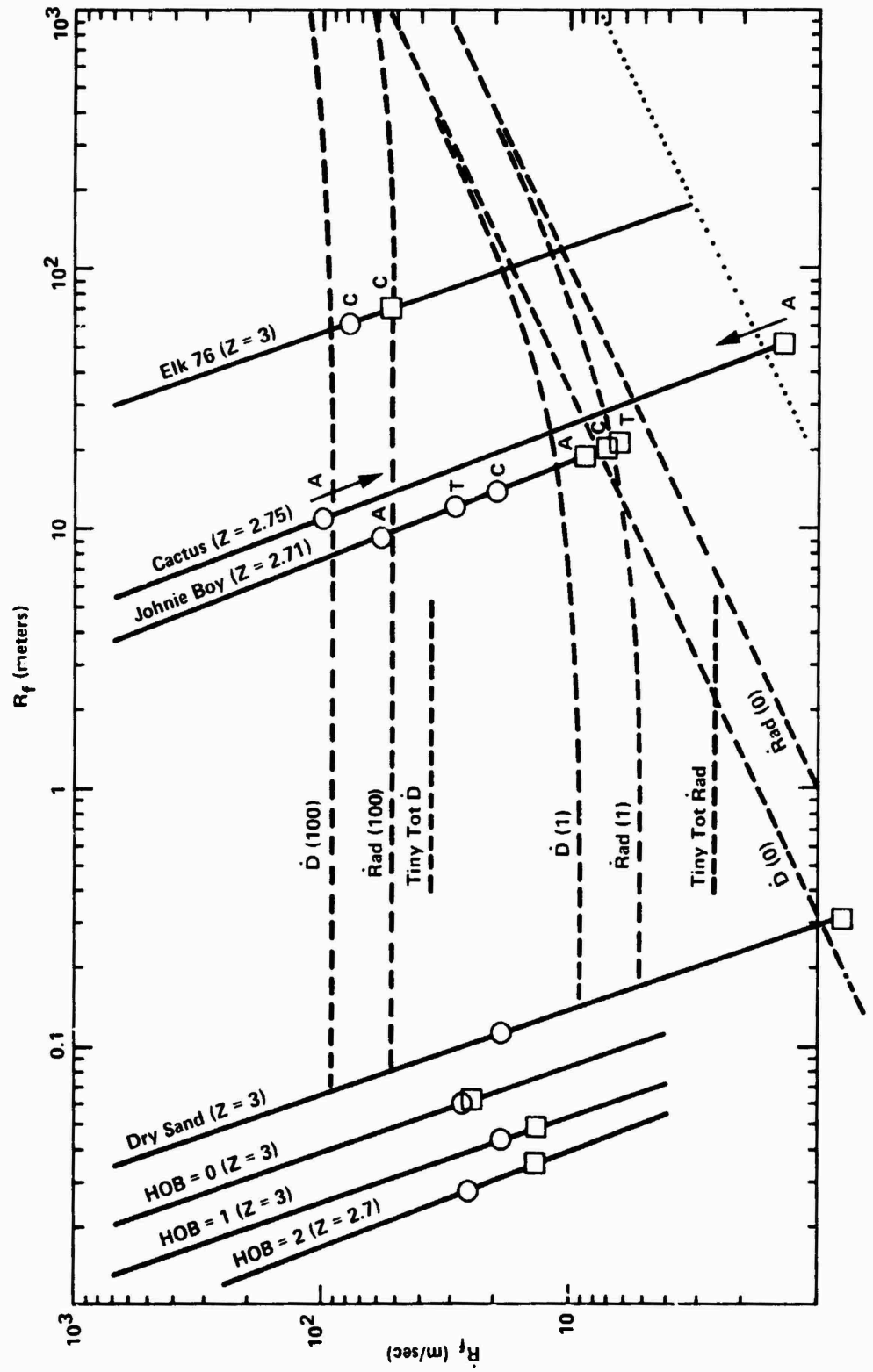

Figure 13 Velocity cutoff data summary--see text for symbols.

(c) The circle and square data points correspond to apparent crater depth and radius, respectively. The labels A, T, and C are used when necessary to distinguish the apparent, true, and computer craters.

(d) The dotted line is discussed later.

The prediction equations were inverted to define the effective yield stresses Y_D and Y_{RAD} from the measured crater depth and radius. The results are given in Table 3. As before, the symbols A, T, and C are used when necessary.

TABLE 3

EFFECTIVE YIELD STRESS (BARS) FOR DEPTH AND RADIUS

Case	Y_D	Y_{RAD}	Remarks
CACTUS	142.0	-1.5	Pacific test crater after some water action
ELK 76	76.0 (C)	87.0 (C)	Strong model of layered shales
JOHNIE BOY	41.0 (A)	1.6 (A)	NTS Area 18 alluvium
	9.5 (T)	0.3 (T)	
	4.0 (C)	0.6 (C)	Alluvium model with 1.6 bars cohesion
HOB = 0	8.0	18.0	Plasticene clay at 76°F
HOB = 1	3.4	5.1	Plasticene clay at 76°F
HOB = 2	6.8	4.5	Plasticene clay at 76°F
ZS-1	4.1	0.01	Dry sand

It can be confirmed that the 6 plasticene dimensions can be predicted within 14 percent by a single value of Y. It appears to be a nearly ideal plastic. The other real materials of Table 3 are not. They appear to have very little strength with respect to the crater radius formation. This is consistent with the moderately successful state-of-the-art procedures that predict crater radii from ballistic trajectories based on early computed flows.

3.3 ALTERNATIVE GRAVITY CONTROLLED RADIUS MODEL

Before describing the alternative method, it is useful to note the features of the usual ballistic method which is applied to the flow field at the time that the computer crater depth is reached. The mass points are assumed to be non-interacting as they travel along ballistic trajectories into mathematical buckets which are fixed in space, usually along the curved surface corresponding to zero vertical velocity at crater bottom time. The collected mass is then converted into volume which fills the buckets to different heights to define the final crater contour.

The moderate success of this method prompted the development of an alternative method, intermediate in assumptions between the stream tube energy balance method and the ballistic method. In this new method, it is assumed that the particles proceed on stream lines (rather than ballistic paths) but that spall or some other effect removes the particle interactions so that energy balance applies to independent particles (rather than the entire stream tube). The final crater radius is then defined by the particle that has the smallest range and zero velocity as it reaches the surface. The flow model provides a simple way of selecting this particle.

The locus of particles with purely horizontal velocities lies along the line $\cos \theta_H$ = constant = $(Z-2)/Z-1)$ in the first order flow model. Consider the set of particles i = 1,2,3,...along this line with coordinates R_i, θ_H and velocities u_i. The kinetic energy per gram at the i^{th} position is $0.5\ u_i^2$. The gravitational potential is $gR_i \cos \theta_H$. The stream line intersects the surface at R_{Si} given by $(R_i/R_{Si})^{Z-2} = 1 - \cos \theta_H$. It can be shown that only one of the particles on the line θ_H has the property $gR_i \cos \theta_H = 0.5\ u_i^2$. The crater radius prediction is then

$$RAD = R_i \left[1 - \cos \theta_H\right]^{1/(Z-2)} \tag{18}$$

with the constraint

$$R_i = u_i^2/(2g \cos \theta_H).$$

Equation (18) can be expressed in a variety of convenient ways, depending on the form of the velocity field data. If α and Z are known, then

$$RAD = (Z-1)^{1/(Z-2)} \left\{ \frac{\alpha^2}{2g} \frac{Z-1}{Z-2} \left[1+(Z-2)^2/(2Z-3)\right] \right\}^{1/(2Z+1)} \tag{19}$$

$$(\dot{RAD}) = \frac{RAD\ 2g(Z-2)/(Z-1)}{\left[1+(Z-2)^2/(2Z-3)\right]} \left(\frac{1}{Z-1}\right)^{(2Z+1)/(Z-2)} \tag{20}$$

The velocity cutoff of Equation (20) for Z = 3 is plotted on Figure 13 as the dotted line. It can be seen that this method predicts substantially larger crater radii than the previous method [RAD(0) of Figure 13]. For ELK 76, the former method predicts a gravity controlled radius of about 115 meters, compared to about 175 meters for the alternative method.

SECTION 4

ADVANCED MODELS AND DATA

The cratering flows of the inspected cases could be approximated with fair accuracy by the first-order flow model. This simple model provided a framework so that additional assumptions could be included to predict ejecta properties and crater dimensions.

A variety of data indicates that a second-order model, allowing for spatial variations in α and Z, would reduce the prediction discrepancies. Though this improved order model has not been developed, data will be presented to indicate reasonable features that should be included. This section will also present miscellaneous data and observations which are not understood but which may be significant.

4.1 POROSITY

It was thought initially that porosity effects would be severe in the cratering process. Computed and experimental data denies this. These data will be presented next.

Reference 2 reports two surface burst calculations that were identical except for the material models. The first, ELK 70(L), employed low porosity coral layers with very little permanent compaction. The second, ELK 75(H), had corresponding layers with high porosity and substantial permanent compaction. The

differences in the two shock waves were large but the stresses and velocities behind the shocks were very similar. The horizontal velocities versus time and stresses versus time at a common point are displayed in Figures 14 and 15. The large differences in the shock waves (due to porosity) are not observed in the steady state flows that begin at about 5 msec.

The displacement fields in the cratering regions were also similar at 12 msec when the calculations were terminated. This can be seen by comparing the grid distortions displayed in Figures 16 and 17. The current crater depth and radius of the low porosity case are larger than those of the high porosity case by 1 percent and 3 percent, respectively.

These computation observations are supported by flash X-ray photographs of the time-dependent crater lip growth seen in the plasticene and sand experiments that had identical sources (tangent spheres of HE). The results are displayed as the circle and square points in Figure A-23 of Appendix A. The differences are small in spite of the large differences in porosity.

Apparently the cratering flows are controlled primarily by the source parameters, with material properties becoming important only at late times when strength effects appear.

The fact that the crater lip growths are the same for the non-porous plasticene and the very porous dry sand also has implications with respect to the conjecture that the airblast, seeping into the porous material, will change the ejection rate. Experimental high explosive airblast data, scaled to the size corresponding to Figure A-23 enters the negative pressure phase at 45 μsec at the ranges of the ejecta. If air is entrained in the sand at high pressure, it does not appear to affect the

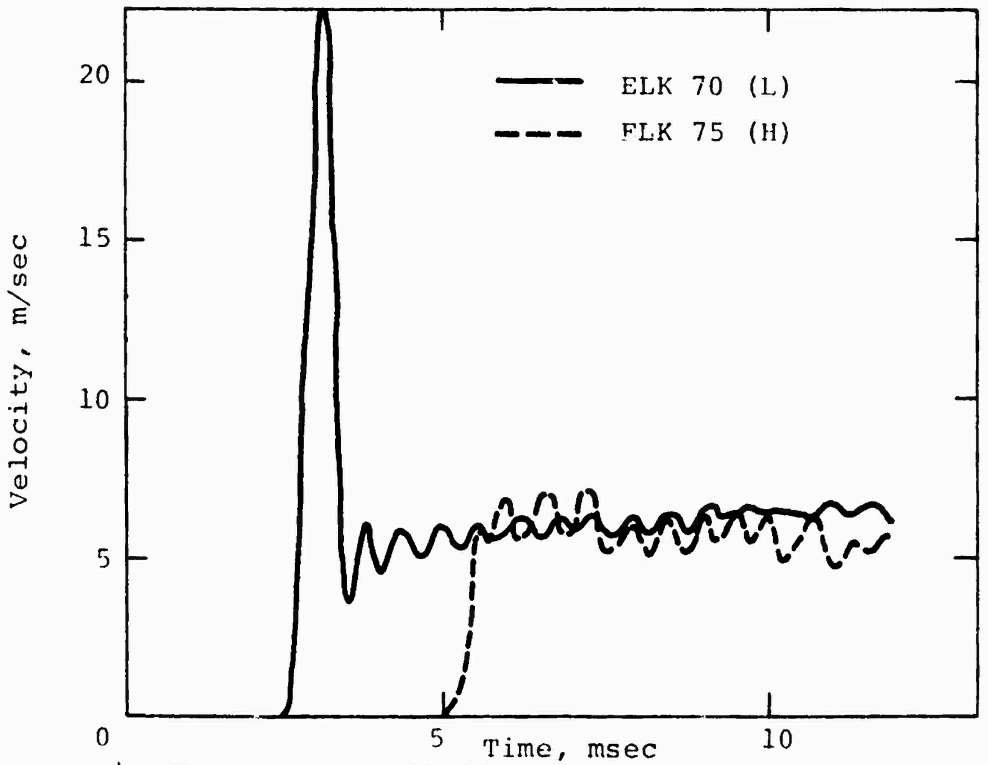

Figure 14 Horizontal velocity histories--10-foot depth, 14-foot range.

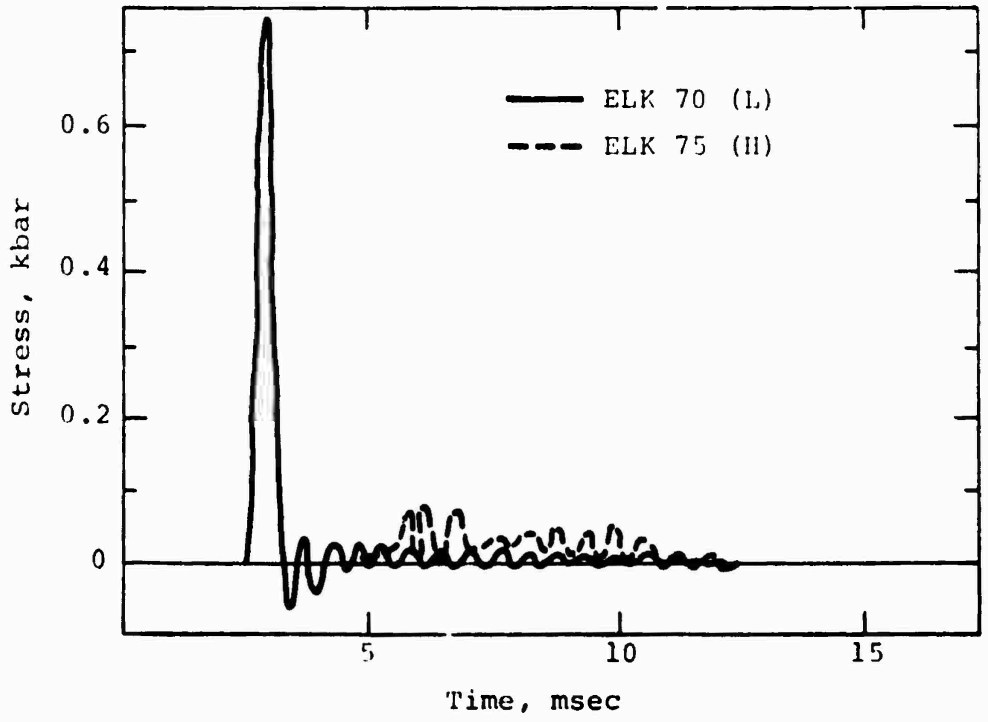

Figure 15 Stress histories--10-foot depth, 14-foot range.

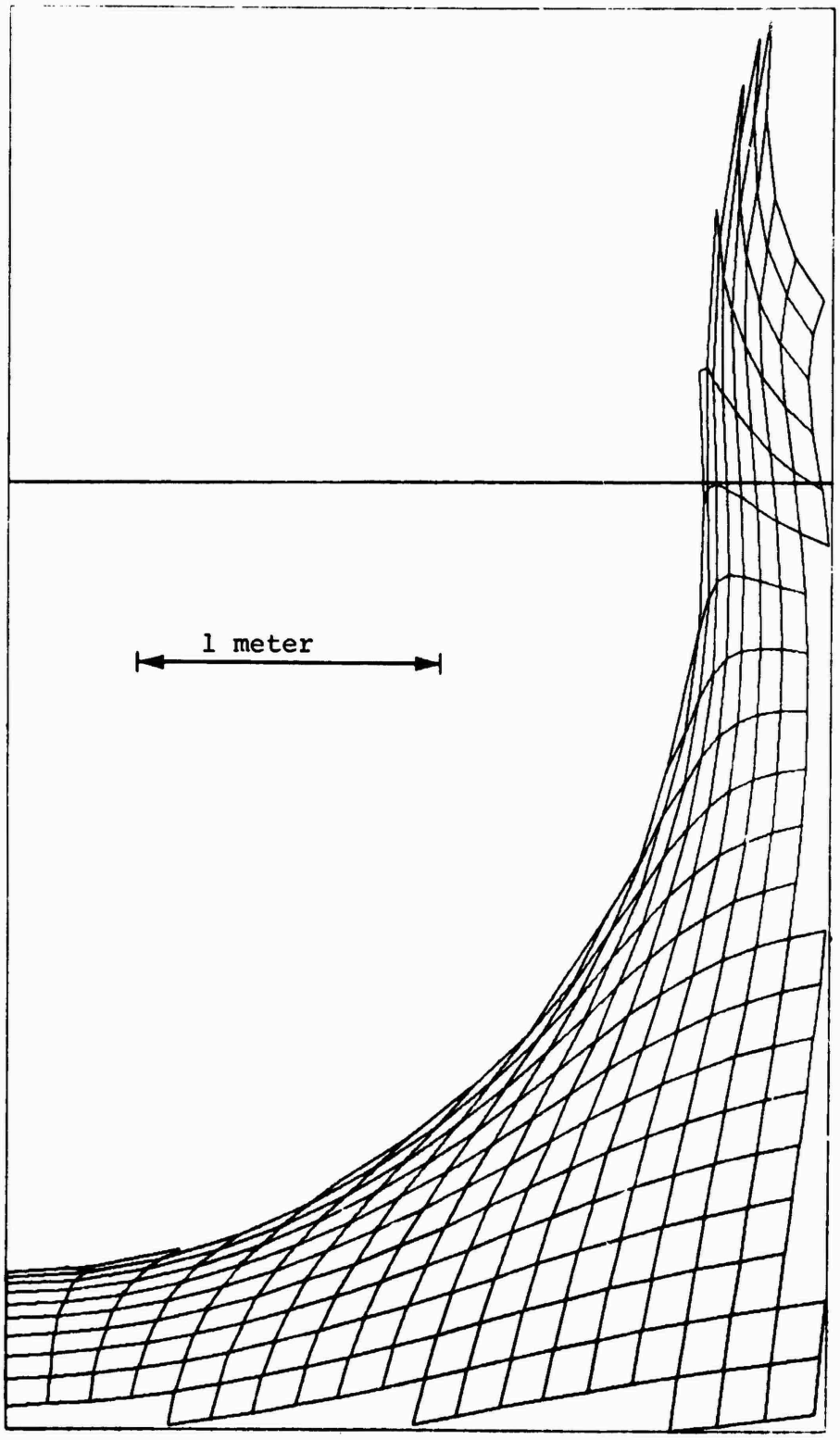

Figure 16 ELK 70 (L) crater at 12 msec.

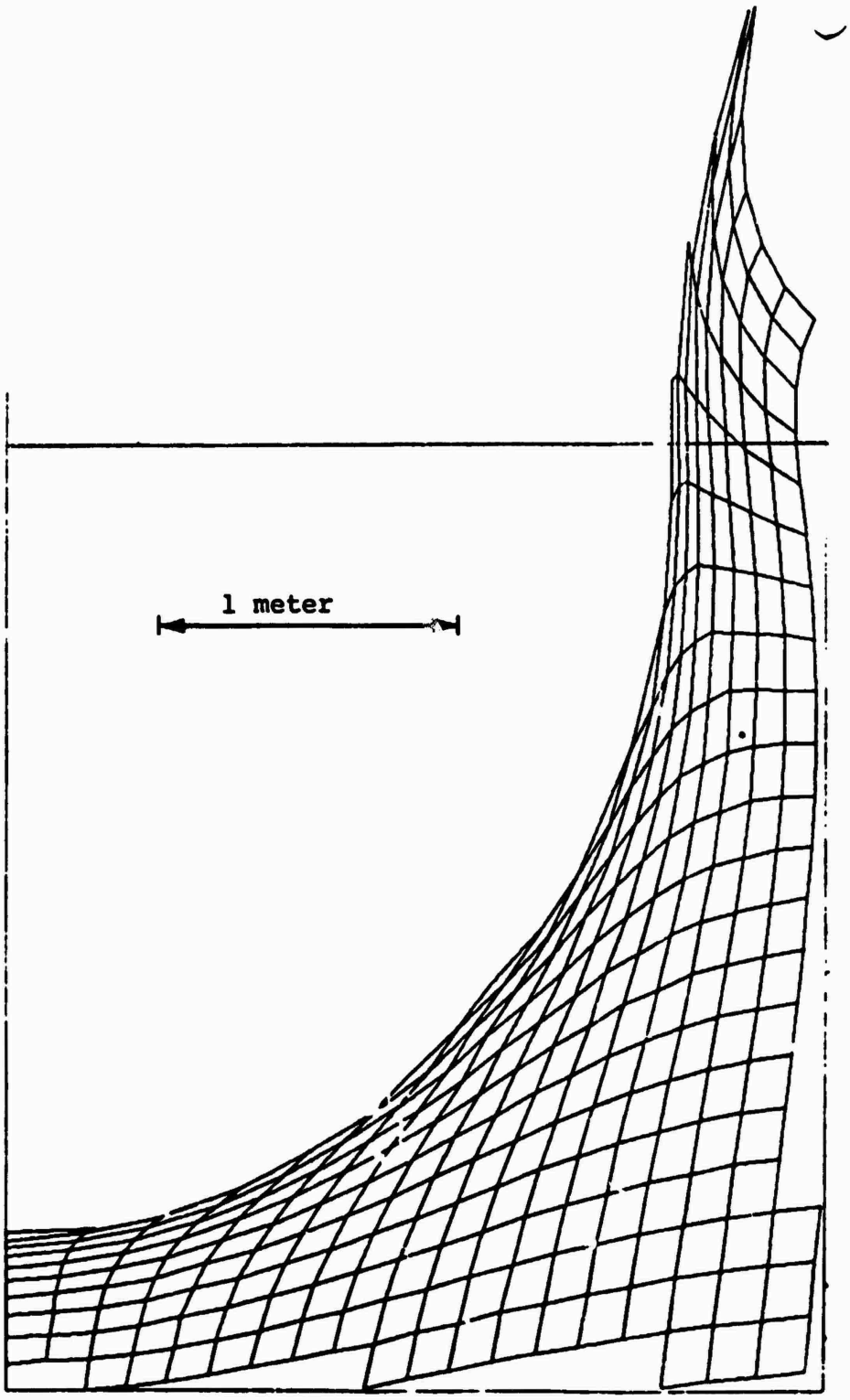

Figure 17 ELK 75 (H) crater at 12 msec.

ejection rate compared to that of the corresponding plasticene within the scatter of the data.

4.2 PLASTICENE DISPLACEMENTS AND VARIABLE Z

Several of the cratering experiments of Appendix A had color banding in the medium to establish the final displacement fields. These can be seen in Figures A-5 through A-8 of Appendix A. The points shown on Figure A-5 for a plasticene case were compared to the Equations (3) and (4) expressions

$$R^{Z+1} - R_o^{Z+1} = R_c^{Z+1} \tag{3}$$

$$(R/R_o)^{Z-2} = (1-\cos\theta)/(1-\cos\theta_o) \tag{4}$$

with Z and R_c being unknown. Trial and error fits were performed and it was found that the best fit values of Z and R_c were essentially constant at given value of θ when Equation (3) was employed. The value of R_c was found to agree well with the measured crater radius at this angle.

The fits for the 14 points on the axis are displayed in Figure 18a. It can be seen that the best fits are

$$Z(0^o) = 1.9 \pm 0.1$$
$$R_c(0^o) = 11.2 \pm 0.1 \text{ cm}$$

The measured crater depth was 11.1 ± 0.1 cm which is in good agreement.

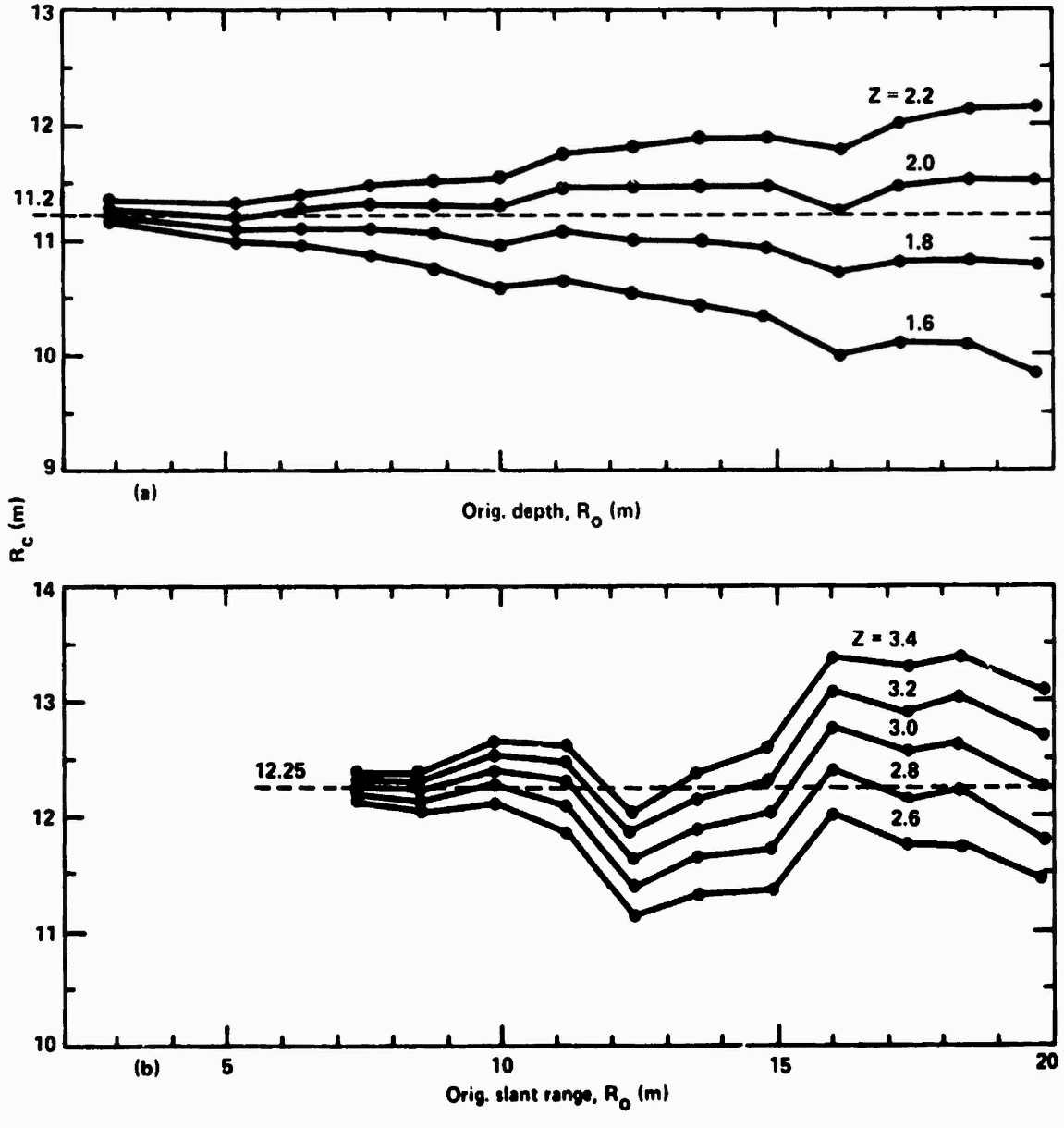

Figure 18 Fits to Equation (3). (a) Top, 14 axis points; (b) Bottom, 11 surface pairs

The 22 surface points were grouped in 11 pairs to eliminate asymmetries. The fits are shown in Figure 18b. The results are

$$Z(90^{o}) = 3.0 \pm 0.2$$
$$R_c(90^{o}) = 12.25 \pm 0.1 \text{ cm}$$

The value of R_c is in good agreement with a crater radius constructed by a smooth extrapolation through the lip spall region.

The 6 points at 60^{o} were fit to Equation (3) as individual points (not in pairs). The results were:

$$Z(\theta = 60^{o}) = 2.9 \pm 0.1$$
$$R_c(\theta = 60^{o}) = 12.0 \pm 0.1 \text{ cm}$$

Again the fit value of R_c agreed well with the experimental radius (slant range) of the crater wall at this angle.

Equation (4) was also applied to these 60^{o} points and the results were surprising. Here the particles were grouped into pairs to show the tendencies more clearly.

Inner pair: $Z(60^{o}) = 1.8 \pm 0.1$, $R_c(60^{o}) = 10.8 \pm 0.1$ cm
Middle pair: $Z(60^{o}) = 1.9 \pm 0.1$, $R_c(60^{o}) = 9.8 \pm 0.1$ cm
Outer pair: $Z(60^{o}) = 2.0 \pm 0.1$, $R_c(60^{o}) = 9.4 \pm 0.1$ cm

These last results are not understood. The other cases (Figure A-6 through A-8) have not been analyzed.

4.3 COOPER DISPLACEMENTS

The final radial displacements of the previous example were consistent with the first order radial displacement model. This suggests a connection between the model and Cooper's displacement correlations that were observed in both soil and rock (see Reference 1 for rock example). Cooper's correlations are:

$$d_H \cong K_H V^{4/3} Y_o^{-3}$$

$$dv \cong K_v V^{4/3} Y_o^{-3}$$

$$\text{for } 2 \lesssim Y_o/V^{1/3} \lesssim 6$$

where d_H and d_v are respectively the horizontal (outward) and vertical (upward) displacements at the horizontal range Y_o. V is the apparent crater volume. K_H and K_v were found to vary with gauge depth and explosive DOB. The values $K_H = K_v = 0.45$ gave reasonable agreement with surface gauge data for above the surface bursts.

The first order model can be used to construct expressions for d_H and d_V. Ignoring higher order terms in d/Y_o, the result is

$$d_H = R_c^{Z+1} Y_o^{-Z} (\sin\theta)^{Z+1} \left| 1 + (Z-2) \cos\theta/(1 + \cos\theta) \right| /(Z+1)$$

$$d_v = R_c^{Z+1} Y_o^{-Z} (\sin\theta)^{Z} \left| (Z-2)(1-\cos\theta) - \cos\theta \right| /(Z+1)$$

where R_c is the inner radius of the displaced mass in a stream tube that passes through the gauge at Y_o and θ. The model expressions have Cooper's form if $Z = 3$ and R_c is proportional to $V^{1/3}$.

However, Cooper's correlations are for sets of gauges at the same depth rather than the same angle and a direct comparison of the methods is possible only for near surface gauges where $\theta \cong \pi/2$. In this case the model results for Z = 3 is $d_H = d_v = 0.25\ RAD^4\ Y_o^{-3}$ where RAD is the displacement crater radius at the surface. A relationship between RAD and $V^{1/3}$ is required in order to proceed.

Cooper (Reference 1) reported that the MINERAL ROCK and MINE ORE apparent crater radii R_A were related to the apparent crater volume by $R_A \cong 1.2\ V^{1/3}$. If R_A is equated to the displacement radius RAD, then the model result is $d_H = d_v = 0.52\ V^{4/3} Y_o^{-3}$ which is 16 percent larger than Cooper's result. Exact agreement is obtained if $RAD = 1.16\ V^{1/3}$

It is concluded that Cooper scaling and the radial displacement model are compatible. It is suggested that the displacement crater can be approximated by the apparent crater, rather than the true crater.

4.4 Z VALUES AND VERTICAL MOMENTUM

Computed and experimental data show that the cratering and ejection process occurs on a very long time scale compared to that of the direct and airblast loading of the cratering region. This implies that the steady state flow field is a coasting process with zero total vertical momentum (up plus down). This places a constraint on allowable values of Z. At early times before surface uplift occurs, it is easy to show that the only constant value of Z that gives zero vertical momentum is Z = 3.

This value is also the only solution of Equations (1) and (2) that gives irrotational flow. The significance of this is not known at this time.

Vertical momentum data were obtained in the flow fields of the 10 surface burst cases of Table 1 as part of the output of the ZEE code (described in Section 4.5). This code processed printout data grouped as concentric surfaces about ground zero (see the dashed lines of Figure 1c for an example). The vertical momenta of the points on a given surface were summed, starting from the axis point, to obtain the accumulated vertical momentum as a function of θ along each surface. More than 100 surfaces were processed in this manner, selected from the 10 surface burst cases of Table 1. Several different times were used in two of the cases. Though this large amount of data has not been thoroughly analyzed, it was seen that the total vertical momentum contained between 0 and 90° was nearly zero in all cases. Apparently, the vertical momentum is nearly zero in concentric shells, as well as over the entire flow. This implies that the angular dependency of Z is such that

$$3 \cong \left[\int_0^{\pi/2} Z(\theta) R^2 \sin\theta \, d\theta \Big/ \int_0^{\pi/2} R^2 \sin\theta \, d\theta \right]_{\text{fixed R}}$$

4.5 THE ZEE CODE AND FLOW CHARACTERIZATION

A code called ZEE was written and used to process printout data to examine flow parameters in detail. The ZEE inputs are point values of coordinates, velocities, and densities. The outputs are values of candidate expressions and graphical displays.

The code first constructs point values of Z from Equation (2) and then finds the corresponding α from Equation (1)

$$Z = 2 + R\dot{\theta}(1+\cos\theta)/(\dot{R}\sin\theta)$$

$$\alpha = \dot{R}\, R^{Z}$$

The Z values are noisy at small θ because of the sin θ denominator. This should be allowed for in the contour plot shown later.

The units of α depend on the value of Z, and α will be noisy if Z varies even slightly. It is more meaningful to measure flow strength at a point in terms of an equivalent crater dimension or velocity cutoff in a standard material. This was done in several ways. One method combined Equations (14) and (15) in a crude way to define

$$R_1 = \left[\alpha^2\, \gamma_a\right]^{1/(2Z)} \left\{\cos^2\theta + \left[1+(Z-2)^2\right] \sin^2\theta\right\}$$

with Y = 1 bar and g = 0. A contour plot of R_1 will be shown later.

Numerous other expressions were processed. The vertical momentum and its properties were described earlier. Another useful expression that will be displayed is

$$\text{ZBAR}(R,\theta) = \left[\int_0^{\theta} Z(R,\theta)\, \sin\theta\, d\theta \Big/ \int_0^{\theta} \sin\theta\, d\theta\right]_{\text{fixed R}}$$

This quantity, evaluated at $\theta = 90^{o}$ and averaged over R should be similar to the volume average Z of the first-order model.

Another promising quantity is

$$\dot{\bar{R}}(R,\theta) = \left[\int_0^{\theta} \dot{R}(R,\theta) \sin\theta \, d\theta \Big/ \int_0^{\theta} \sin\theta \, d\theta \right]_{\text{fixed R}}$$

This quantity, evaluated at $\theta = 90^{o}$, should be similar to the volume average $\dot{\bar{R}}$ used in Figure 3.

The Z, ZBAR, R_1, and $\dot{\bar{R}}$ representations described above are displayed in Figures 19 through 22 for the same flow field. The case is ELK 66 (tangent HE sphere) at 30 μsec. The shock wave is just beyond the range of the data. The shock tail extends inward to about 4.5 cm and accounts for the upward curvatures in this region.

This set of four displays was obtained for all of the 10 surface-burst cases of Table 1. Several times were used in two of the cases to confirm that the time dependencies were small. Although it is not obvious in the early time data of Figures 19 through 22, the other data showed that the variations with R were small in the region well behind the shock. The θ dependency remained, however.

Except for spatial scale, it was seen that the patterns of the 10 cases were similar and could be grouped in order of similarity. The half-buried HE sphere (ELK 67) was at one extreme, and the HE sphere elevated by one radius (ELK 69) was at the other. The other patterns were intermediate with the tangent HE sphere (ELK 66) being most similar to the 5-Mt surface burst (ELK 76).

The data has not been analyzed in sufficient detail to uncover a quantitative means of describing and ranking these four. It is felt that this can be done and that a refined flow model would result.

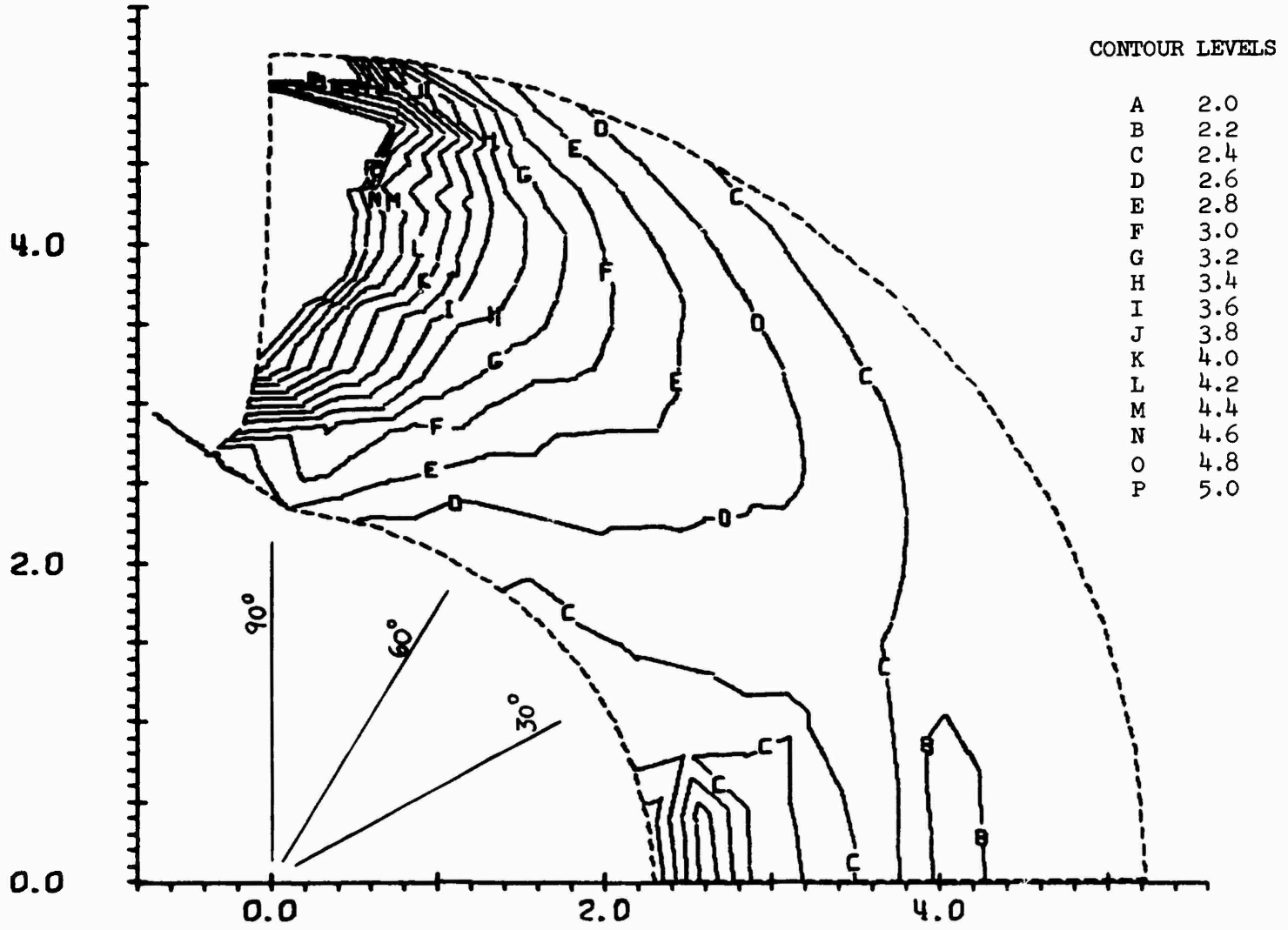

Figure 19 Contours of constant Z for ELK 66.

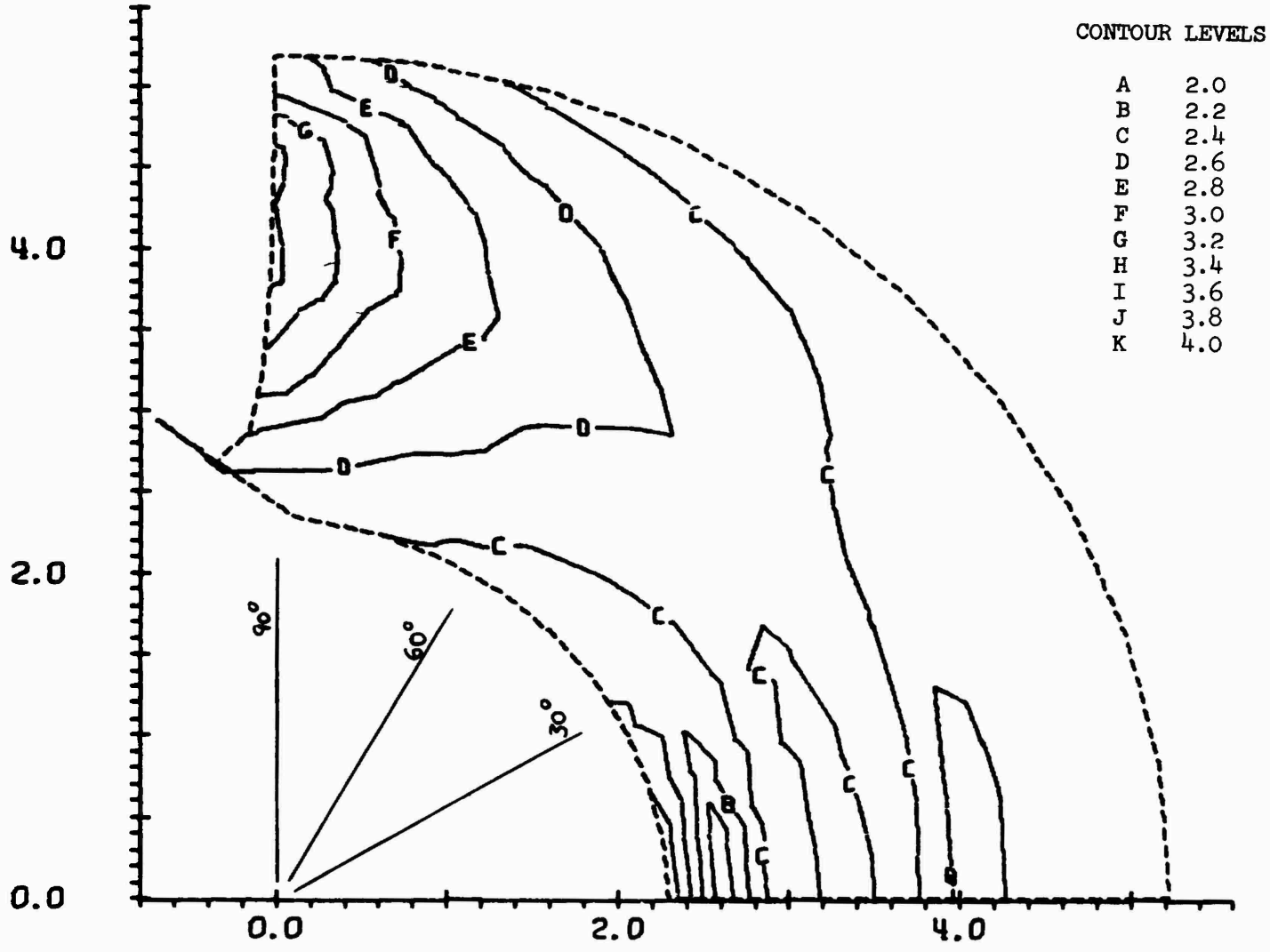

Figure 20 Contours of constant ZBAR for ELK 66.

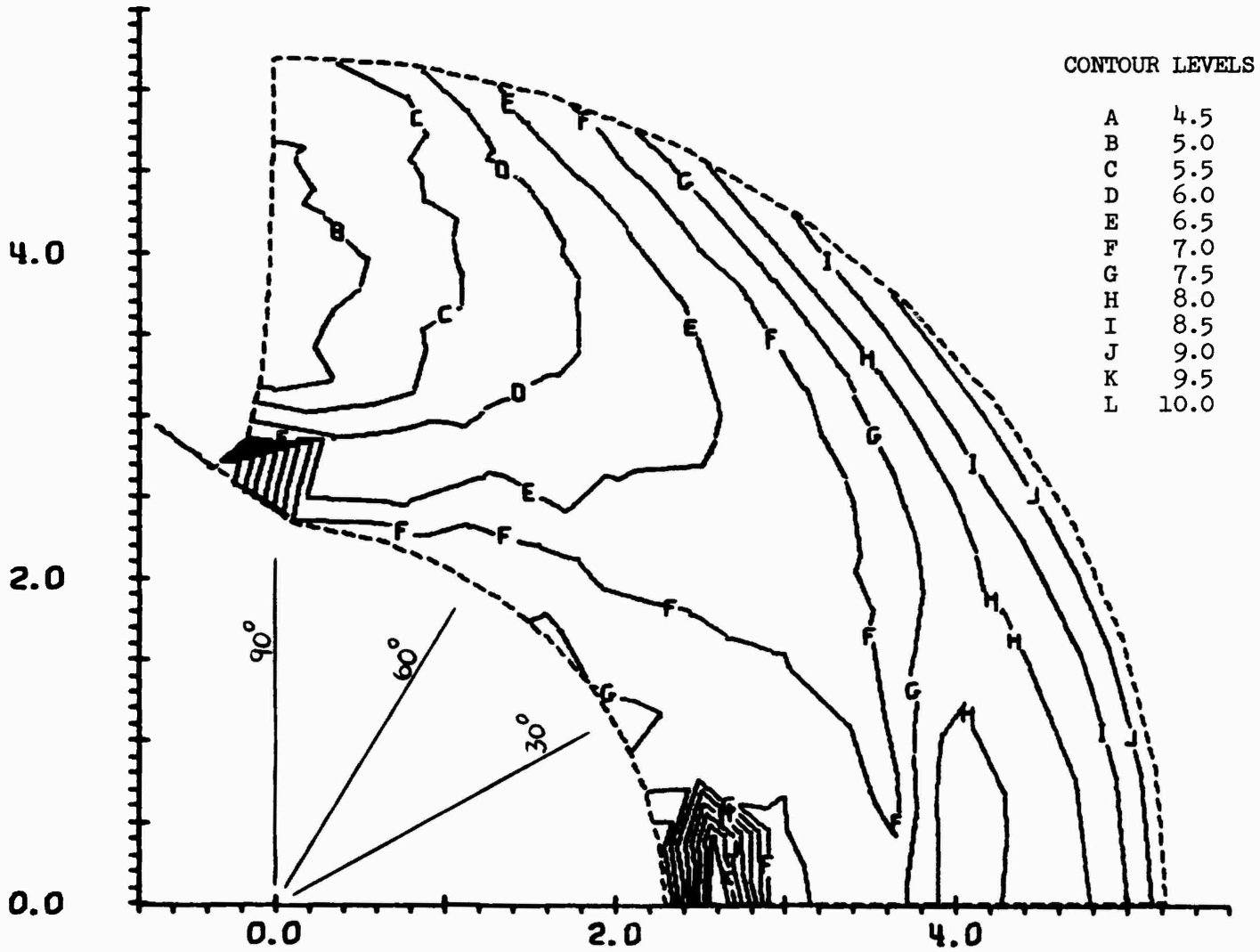

Figure 21 Contours of constant R_1 for ELK 66.

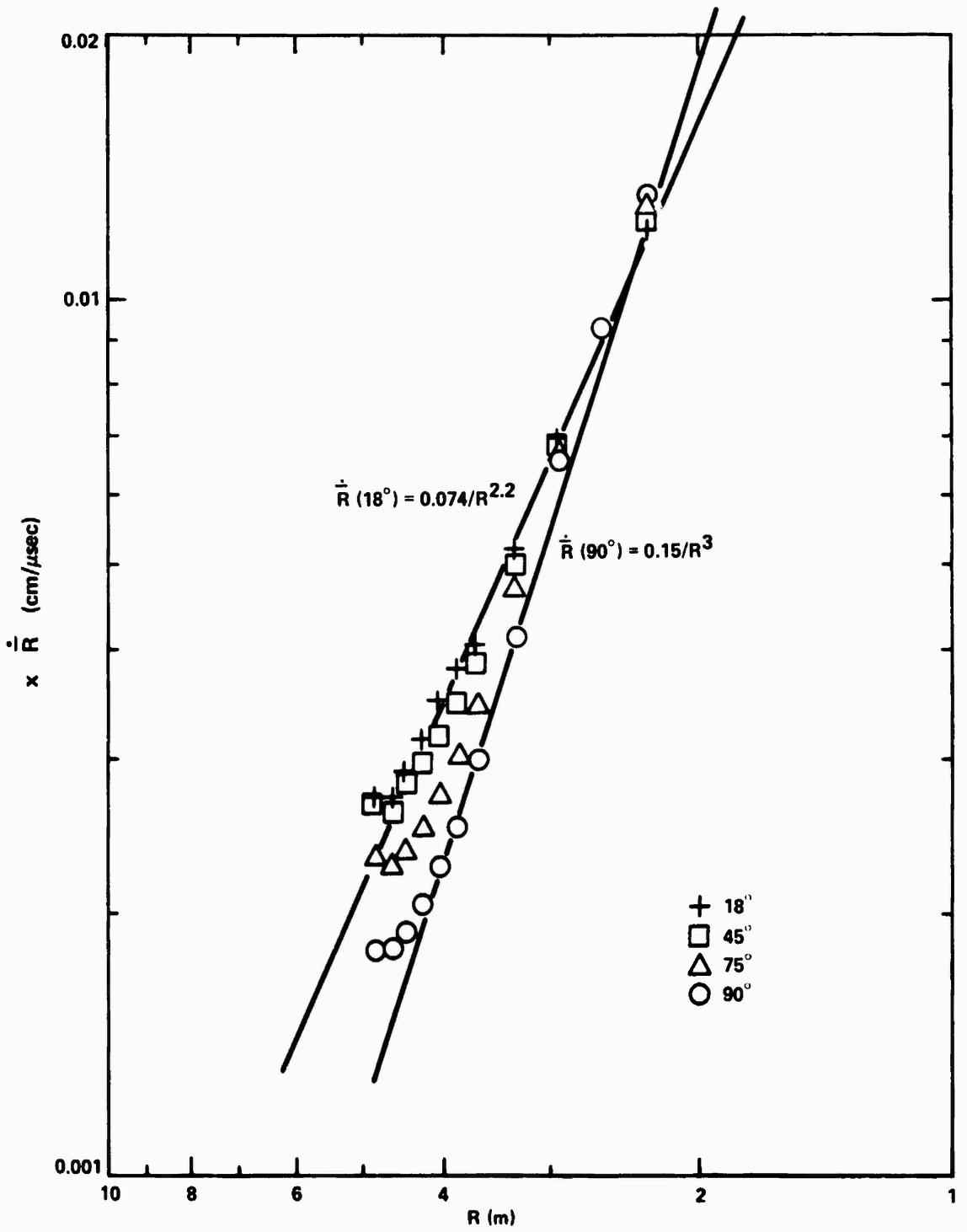

Figure 22 $\dot{\bar{R}}(0)$ versus R for ELK 66.

SECTION 5

SUMMARY AND CONCLUSION

5.1 SUMMARY

It was found that the cratering flows observed in the ten computed surface burst cases* could be approximated by a first-order model to predict time-dependent trajectories, displacements, and ejecta. An elastic-perfectly plastic material assumption together with an energy balance approximation was used to predict final crater sizes and shapes and to explore the scaling rules and the roles played by material strength and gravity.

Data for extending and improving the models were collected and processed but not adequately analyzed. Some general features of an improved description were established though the final model was not.

5.2 CONCLUSION

The approximate agreement of the existing models to a variety of cases and applications is the most signifcant result of this study. It is concluded that a reasonable framework has been established that unifies the processes of cratering, close-in displacements and ejecta, and provides a basis for improving understanding.

---

*The MINE ORE computed flow was also examined. The ground shock from the high explosive source was not strong enough to initiate a significant region of steady state flow due to an unrealistically strong granite model.

REFERENCES

1. H. F. Cooper, Jr., "Empirical Studies of Ground Shock and Strong Motions in Rock," R and D Associates document RDA-TR-3601-002. Defense Nuclear Agency number DNA-3245F, October 1973.

2. J. Reaugh and F. Borden, "Cratering and Ground Motion Calculations for Project MICRO ATOLL," PIFR-411 (draft), Physics International Company, San Leandro, California, November 1973.

APPENDIX A

EXPERIMENTAL REPORT OF CRATERING, DISPLACEMENT, AND EJECTA PROCESSES

Various experimental tests were performed using specially prepared test beds and small charges to examine the dynamics of crater development and the permanent post-shot deformations that occur as a result of crater formation under controlled laboratory conditions.

Two materials that simulate earth media were selected for the experimental test bed. Plasticene clay, a suspension of white marble dust in a petrolatum and wax matrix with a density of 1.69 gm/cm^3, was selected to simulate a clay earth media. Nevada Type 47 sand was selected to simulate sandy, alluvial soil. This sand is a fine-grain, high-purity, quartz sand with an uncompacted density of 1.53 gm/cm^3. For experiments performed in this program, the sand was kept dry and in an uncompacted state. Separate test beds were made for the two test materials. The test beds were pits sunk in the ground with the top surface level with the surrounding soil. These pits were 8-feet square by 4-feet deep and were enclosed in a 2-inch-deep concrete apron at the surface level.

As tests were performed in the plasticene material, it became evident that crater size was strongly dependent on clay temperature. Attempts were made to characterize the dependency of plasticene strength on temperature variations. Unconfined

compressive strength, shear strength, and ball drop penetration tests were performed in an attempt to obtain a clearer view of plasticene behavior. Unfortunately, the data were difficult to interpret because of creep. Plasticene strength is apparently extremely strain-rate and temperature dependent and cannot be well characterized in an essentially static test, such as an unconfined compressive strength test or a shear strength test. The ball drop data, being less affected by creep, appears more promising.

1.1 PERMANENT CLOSE-IN DEFORMATION AND DISPLACEMENT TESTS

The first experimental test series examined the permanent, close-in deformations and displacements that occur as a result of crater formation. Surface displacements were measured by placing wooden pegs (1/16-inch in diameter by approximately 3/4-inch long) as markers in the clay or sand and measuring their pre- and post-shot distance from a permanent bench mark. The centerline of the shot, relative to the bench mark, was also measured before the shot, and thus the radial displacement could be obtained. Crater profile and volume were obtained by using a crater contour gauge. Since the craters were symmetrical, a profile taken through the centerline of the crater was sufficient to determine crater volume. Figure A1 is a photograph of the crater contour gauge over a symmetrical sand crater. Since the sand craters were relatively large, the contour gauge was limited to taking a profile along a radius from the center.

Close-in crater displacement and deformation were obtained by placing a series of multicolored columns vertically beneath the centerline of the shot. In the plasticene media, the

Figure A1 Crater contour gauge in rack over a crater in sand.

columns were prefabricated into a slab of plasticene (Figure A2), which was placed into the test bed. Molten clay was then poured around the slab to ensure a voidless fit (Figure A3), and the explosive was placed on the centerline of the slab. Following the shot, the slab containing the columns was removed from the test bed and was sectioned along the centerline to obtain a pictorial representation of the close-in, permanent deformation (see Figures A4 through A8).

The close-in deformation of the sand test bed was obtained by placing multicolored columns of epoxy-loaded sand along the centerline of the shot. The sand surrounding the columns (and the columns themselves) was loaded with 1 percent, thermosetting, powdered epoxy. After the test, an aluminum box was forced gently around the area containing the conditioned sand and the crater centerline. This box and the sand in it were then heated until the epoxy was cured, and then the competent sand was removed for sectioning and inspection (see Figures A9 through A12).

To determine whether or not the 1-percent epoxy loading alters the crater formation processes, a shot was fired in the sand test bed, but with no epoxy in the sand. The results from this test showed that a loading of 1 percent, powdered epoxy in the sand has no effect on crater formation. A comparison of the crater profiles is shown in Figure A13).

Surface displacement records were taken by placing wooden pegs (approximately 1/16-inch diameter by 3/4-inch length) as markers and measuring their pre- and post-shot distance relative to a permanent bench mark. These pegs were protected from movement caused by the airblast effects by a large steel and wood cover that was placed over the row of pegs, almost but not quite touching the sand. Crater profile and volume were obtained by using a crater contour gauge.

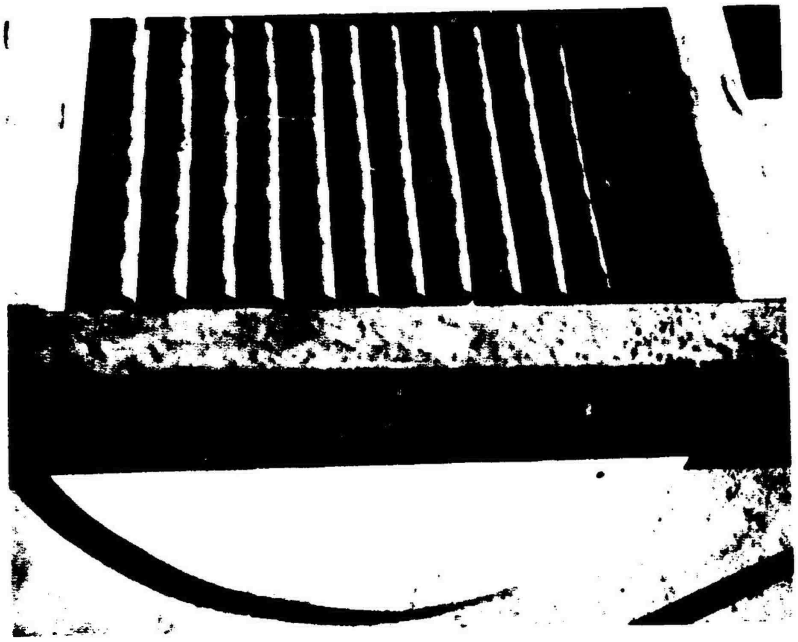

Figure A2 Multicolored columns of plasticene before being made into a slab for placement in the test bed.

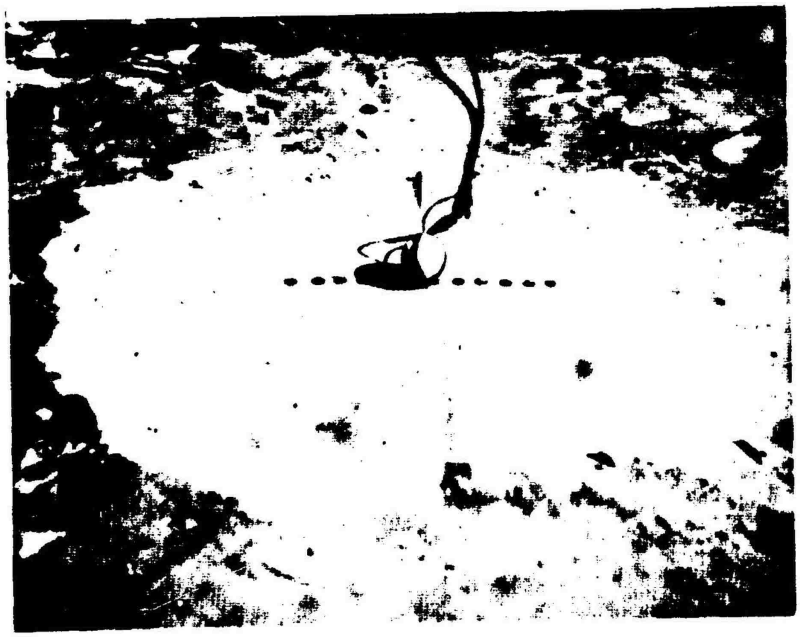

Figure A3 Columns in place in test bed with 2-inch-diameter sphere of C-4 ready for firing.

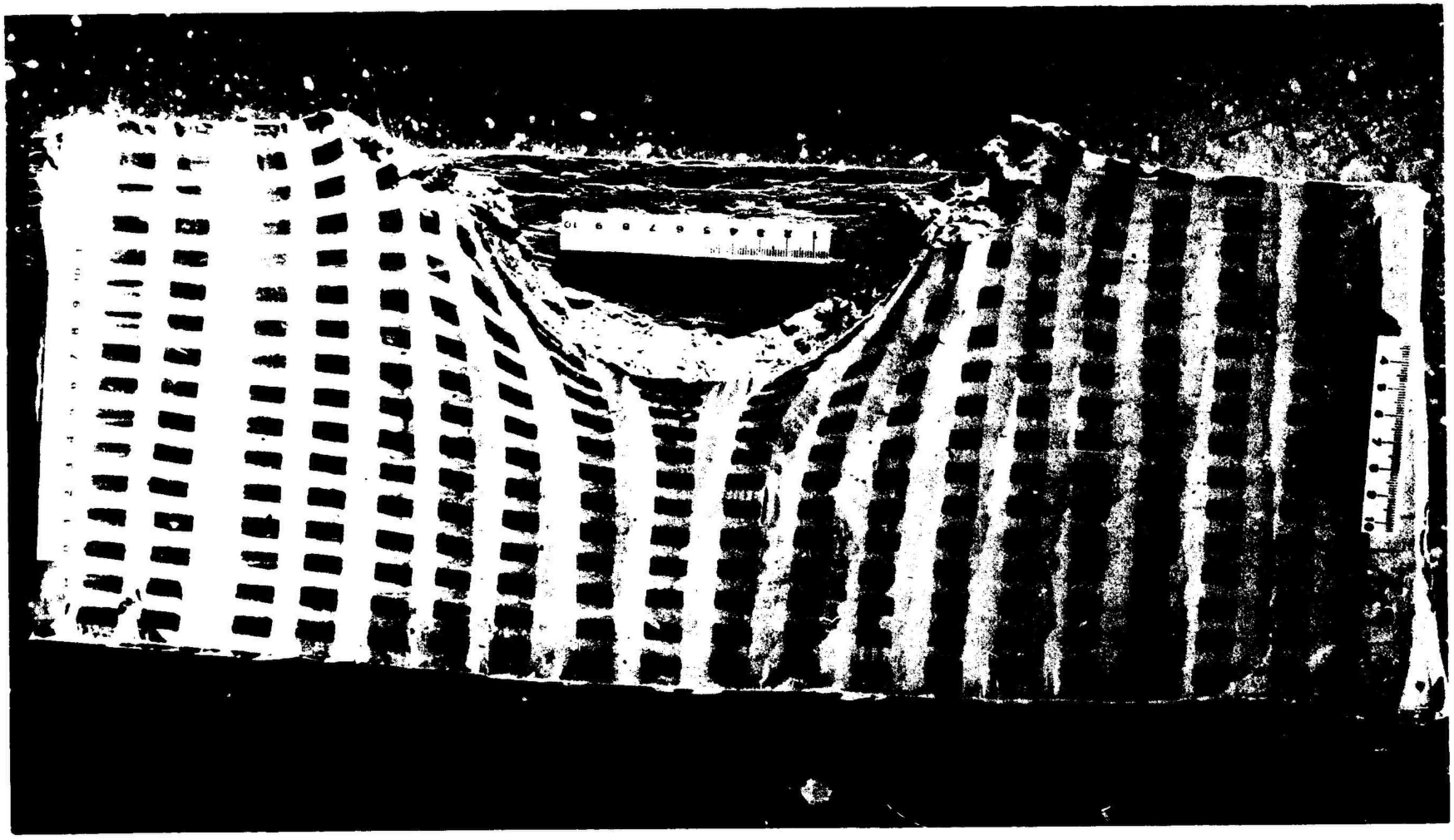

Figure A4 View of crater in plasticene sectioned to show colored column illustrating permanent displacement and deformation.

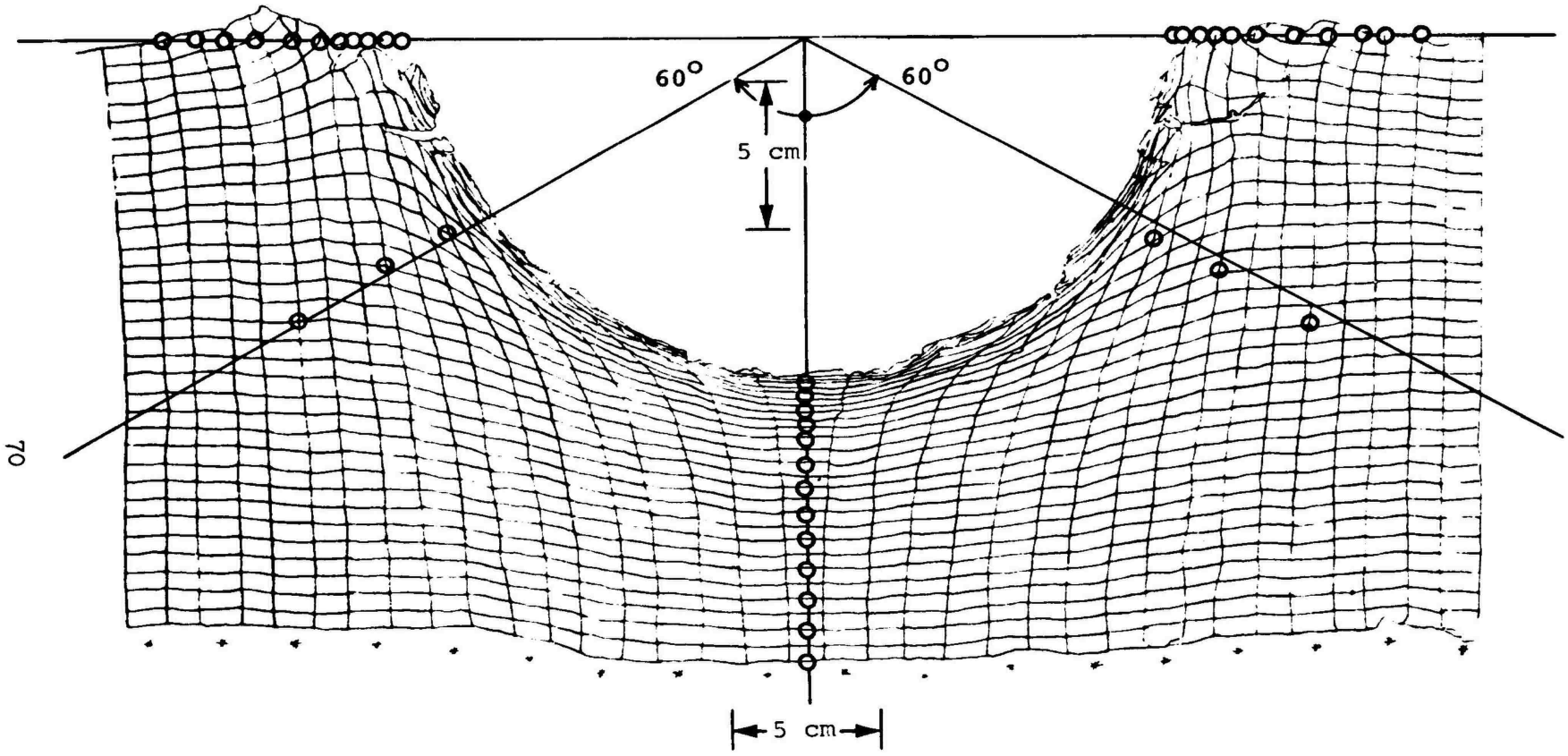

* Denotes colored column in clay during experiment

Figure A-5 Experimental data, shot Z-C2, 2-in.-diam C-4 sphere, tangent to surface of clay. Clay temperature = 76°F. The circled points are analyzed in Section 4 of main text.

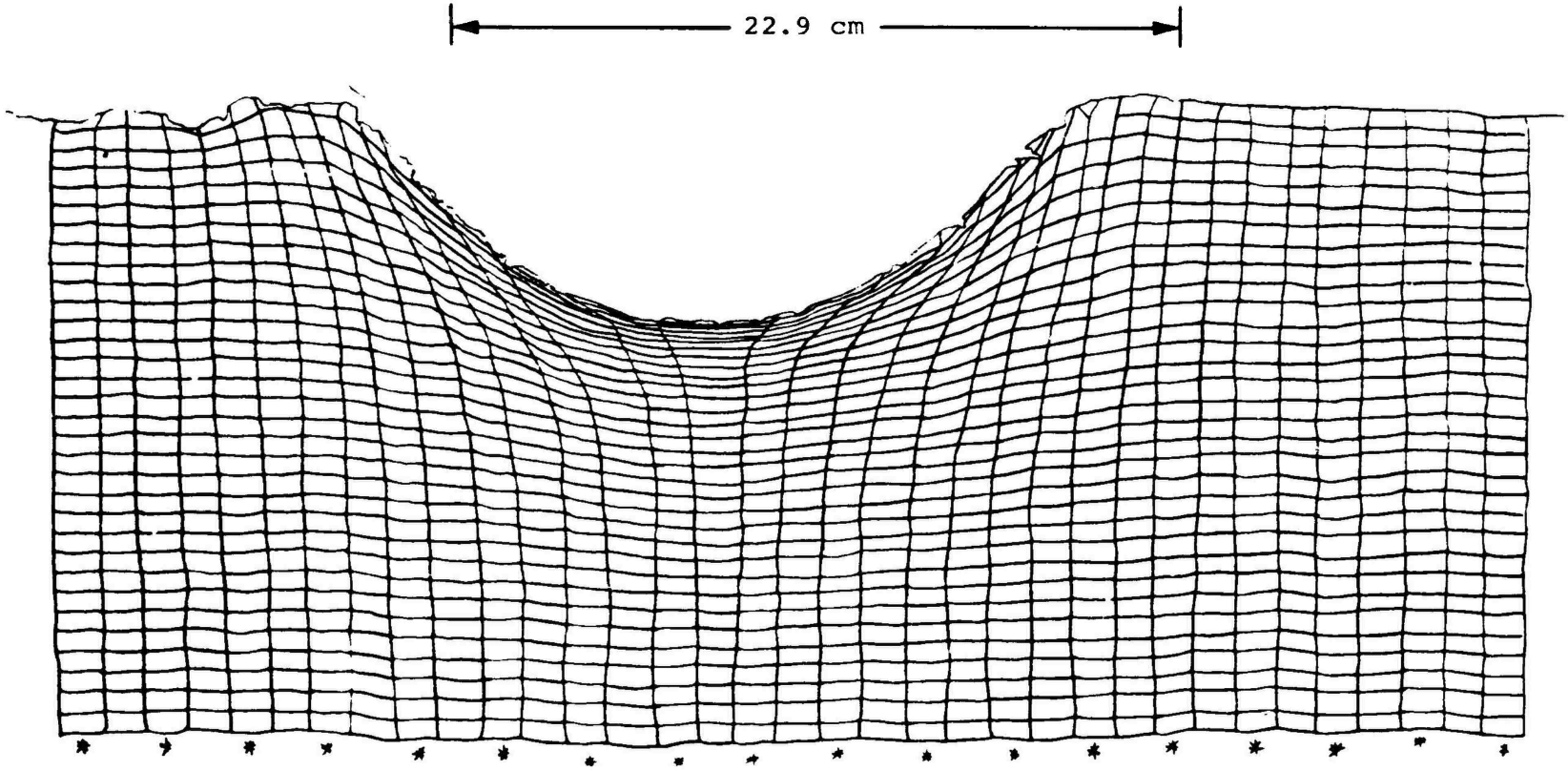

* Denotes colored column in clay during experiment

Figure A-6 Experimental data, shot Z-C3, 2-1/2-in.-diam C-4 sphere, elevated 1-1/4-in. above surface. Clay temperature not recorded.

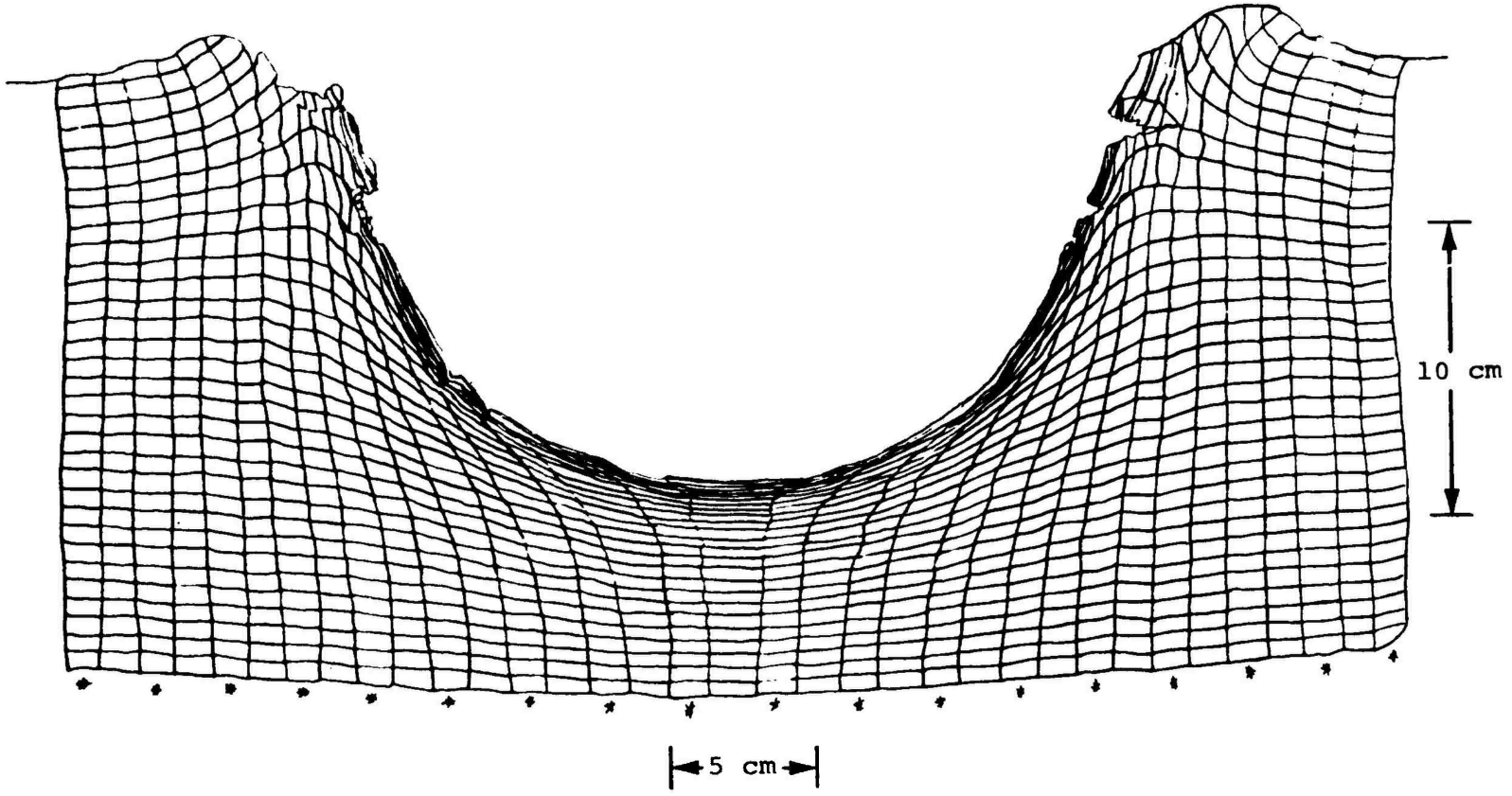

* Denotes colored column in clay during experiment

Figure A-7 Experimental data, shot Z-C4, 1-3/8-in.-diam C-4 sphere, half buried in plasticene clay. Clay temperature = 90°F.

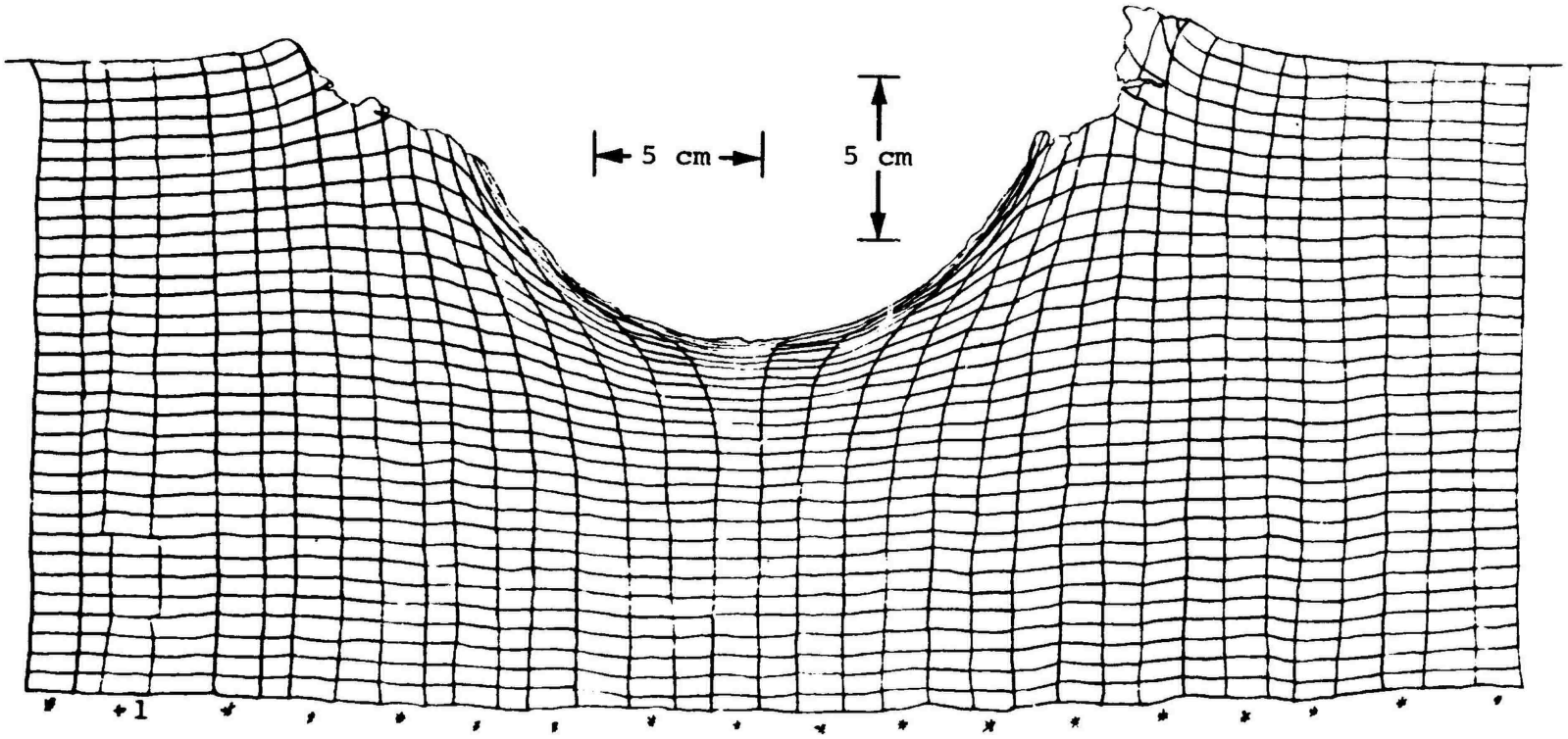

* Denotes colored column in clay during experiment

1 Anomaly in this column assumed to have occurred in fabrication

Figure A-8 Experimental data, shot Z-C5, 1-3/8-in.-diam C-4 sphere, half buried. Clay temperature = 63.5°F.

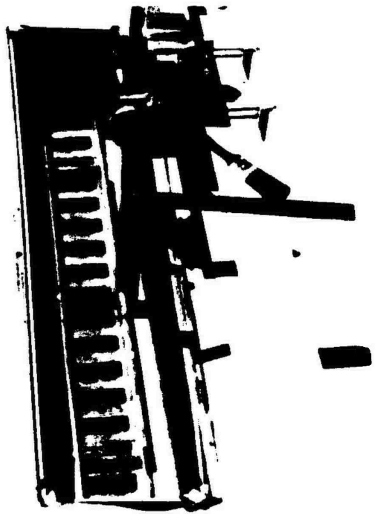

Figure A9 Fixture for placing multicolored sand columns in position in test bed.

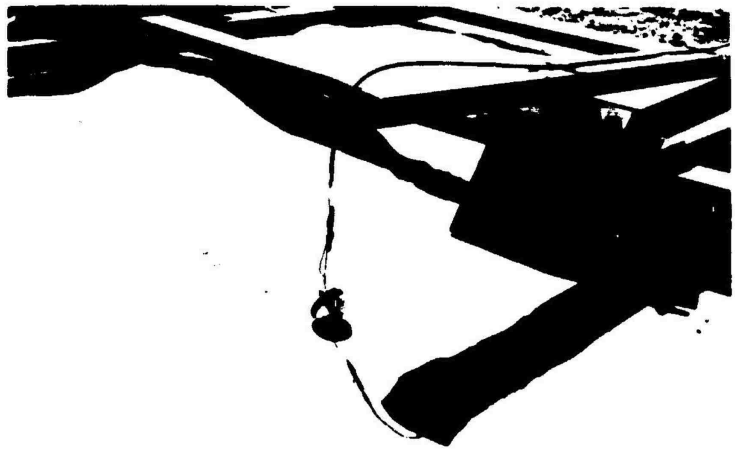

Figure A10 Sand test bed ready for experiment.

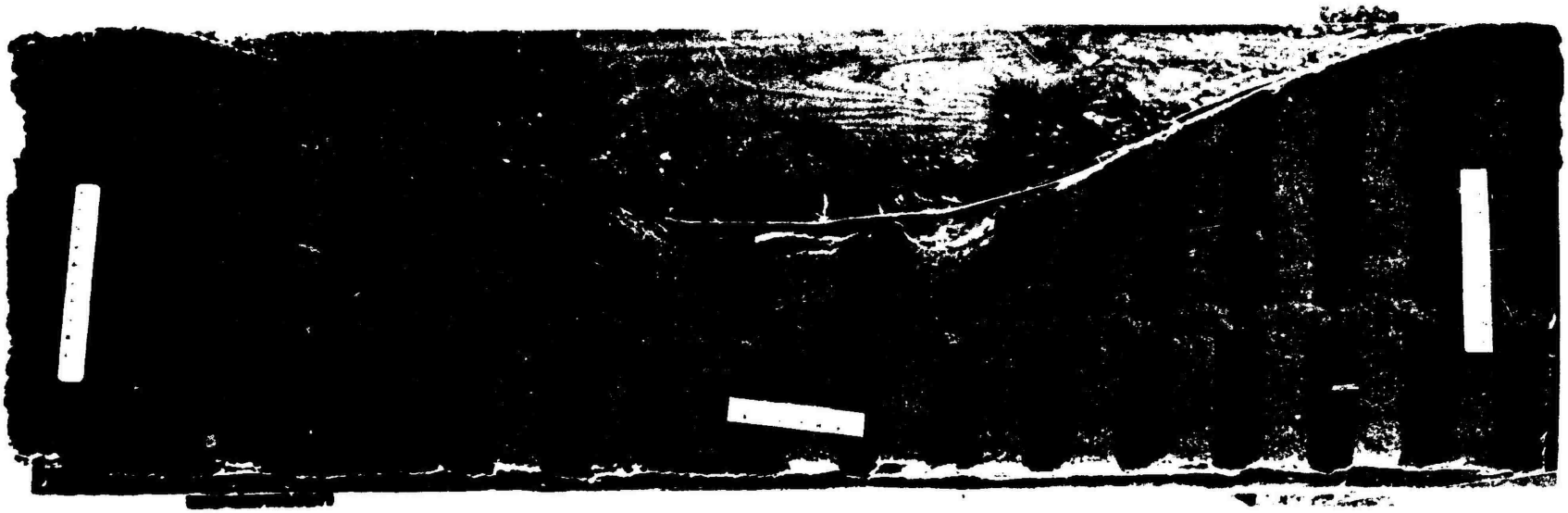

Figure A11 View of crater in sand sectioned to show colored columns illustrating permanent displacement and deformation.

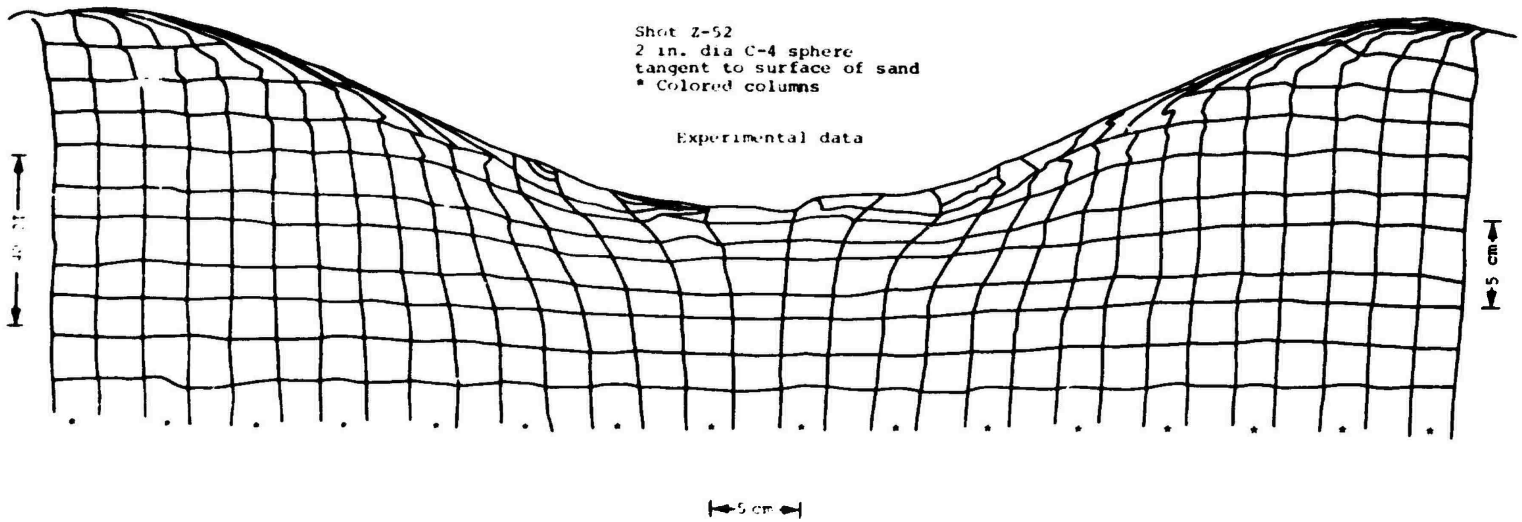

Figure A-12 Sand crater, shot Z-52 (tangent sphere).

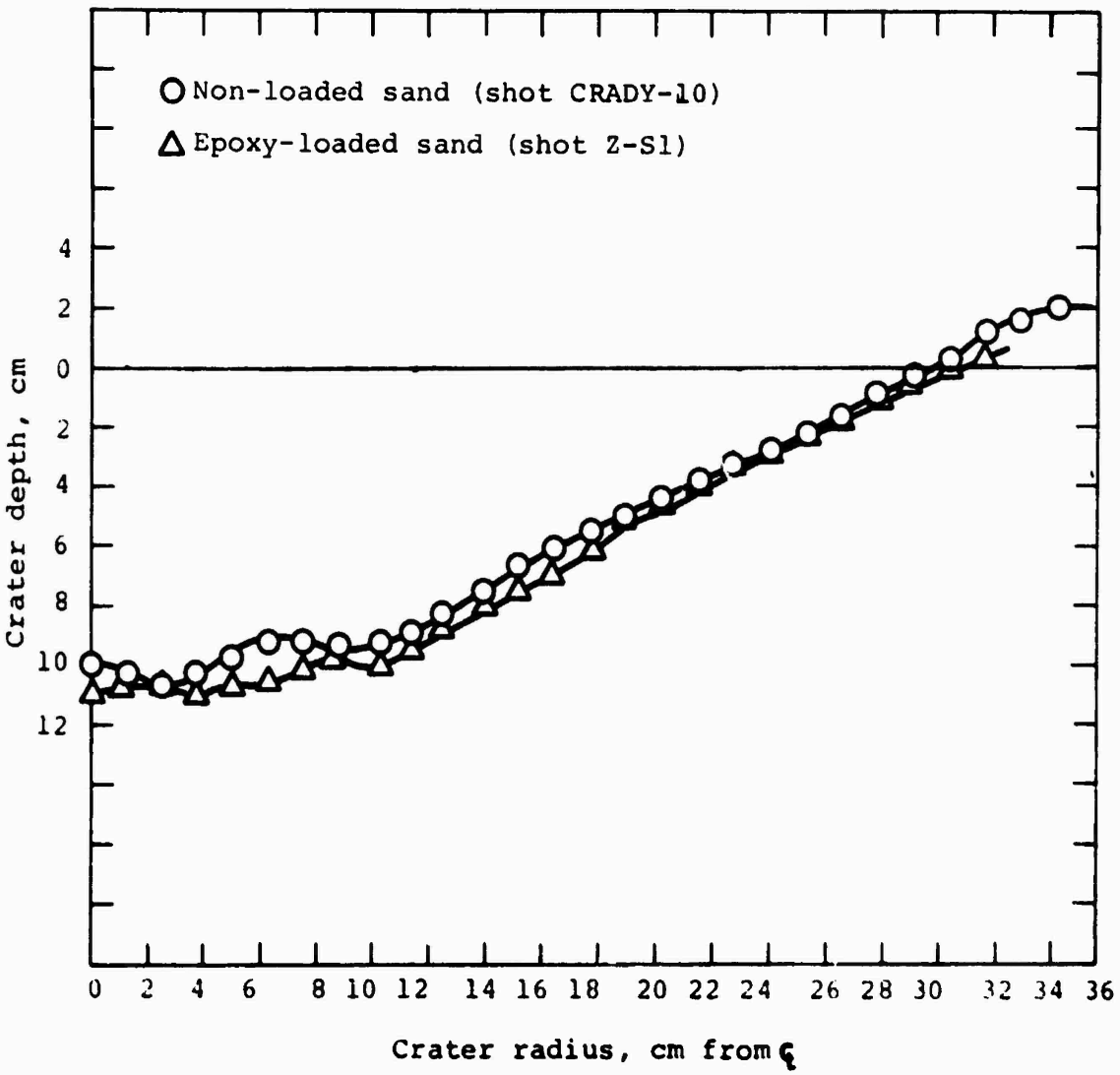

Figure A-13 Effects of epoxy loading on crater formation (pure sand versus sand loaded with 1-percent powdered epoxy) Crater formed with a 2-inch-diameter sphere of C-4 tangent to surface of sand.

Surface, permanent displacements are shown plotted against crater radius in Figures A14 through A18. For these plots, both displacement and original radius were divided by crater volume to the one-third power. The straight line through the data is a fit to the results obtained by Cooper.

It can be seen that the half-buried, spherical, explosive cases of Figures A14 and A15 (corresponding to shots Z-C5 and Z-C4 at temperatures of 63.5°F and 90°F) give results that are in fair agreement with Cooper's data. The surface tangent cases of Figures A16 and A18 also yield fair agreement. The elevated shot case of Figure A17 shows a much different range dependency than that of the surface burst data of Cooper, a result that is not surprising.

The plasticene crater experiments corresponding to scaled-up versions of the calculations ELK 67, 66, and 69 employed high-explosive charge diameters of 1.375, 2.0, and 2.5 inches, respectively, to obtain crater sizes that utilized the test bed efficiently. The corresponding scale factors of length to relate the ELK experimental charge sizes to the respective ELK calculations are 0.573, 0.394, and 0.315 before detonator correction. When the type RP-2 detonator, its volume, and its high-explosive content are taken into account, the previous scale factors are changed slightly to become 0.579, 0.3945, and 0.3153, respectively. The results, including the results of the sand experiment which were not calculated, are shown in Table A1.

Figure A19 displays two experimental crater sections for each of the scaled experimental data of ZC-6, ZC-5, and ZC-7 for the 76°F cases corresponding to the calculations ELK 67, 66, and

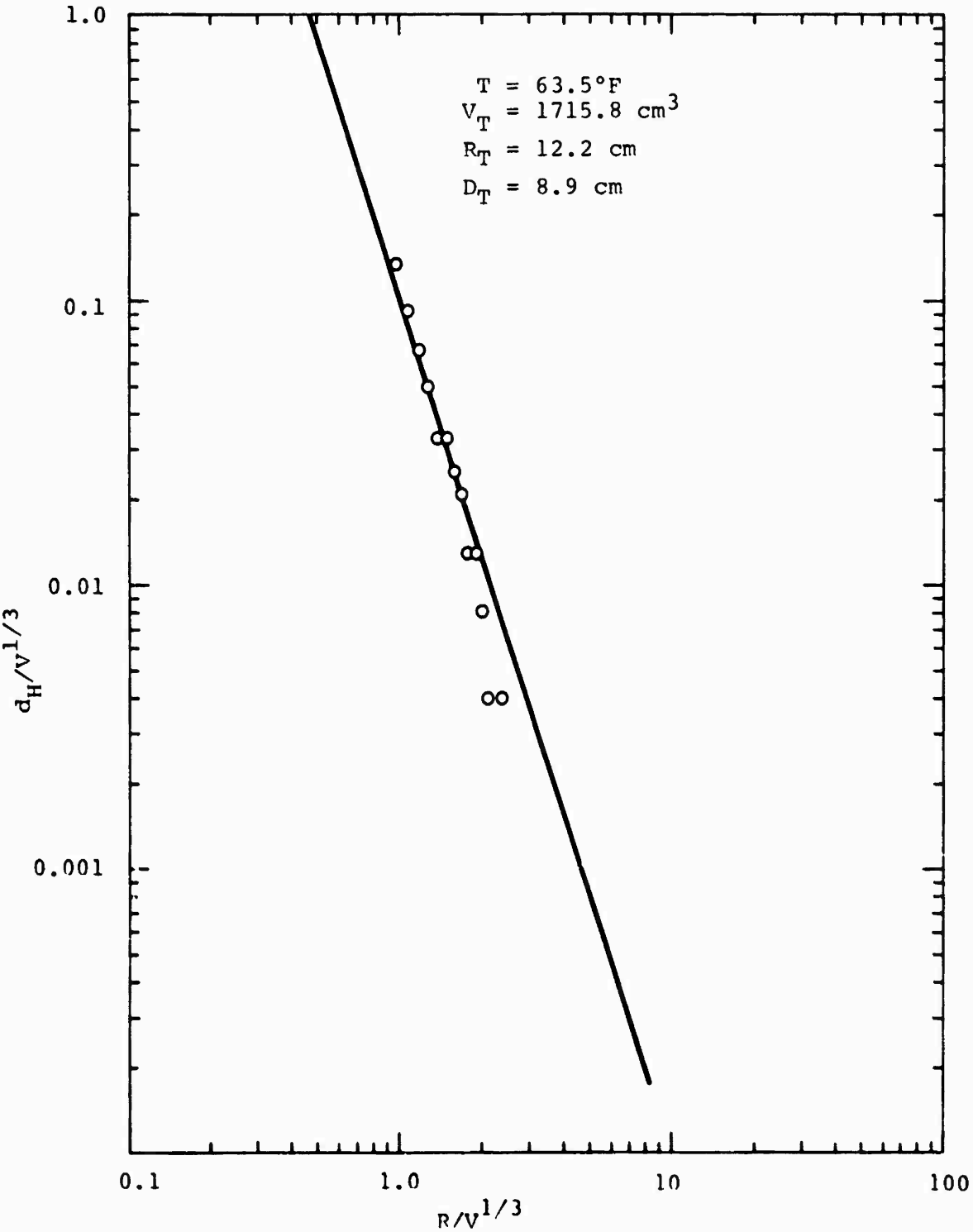

Figure A-14 Shot Z-C5, surface horizontal displacement versus range (both scaled by cube root of crater volume) in plasticene 1-3/8 in. diam C-4 sphere, half buried.

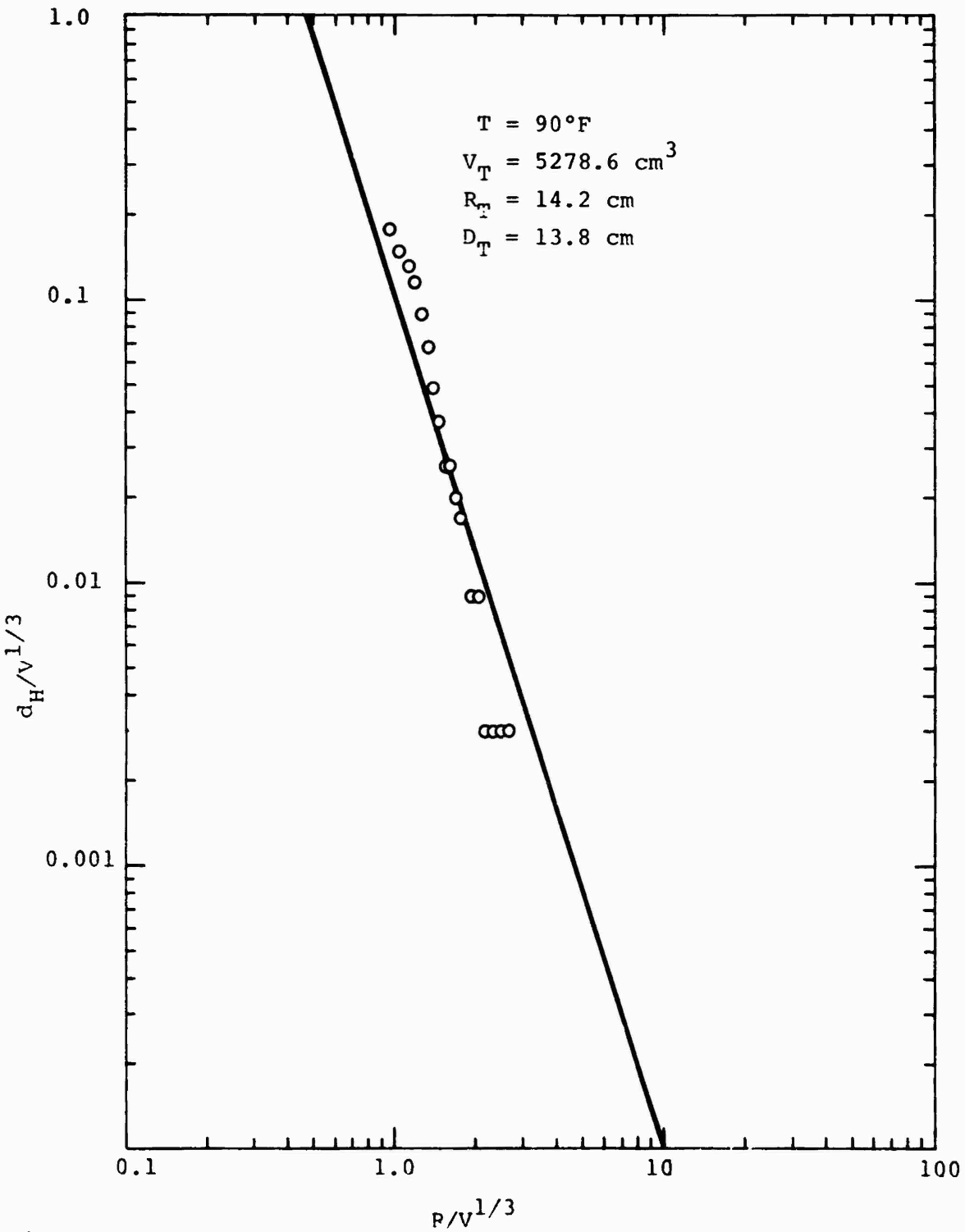

Figure A-15 Shot Z-C4, surface horizontal displacement versus range (both scaled by cube root of crater volume) in plasticene 1-3/8 in. diam C-4 sphere, half buried.

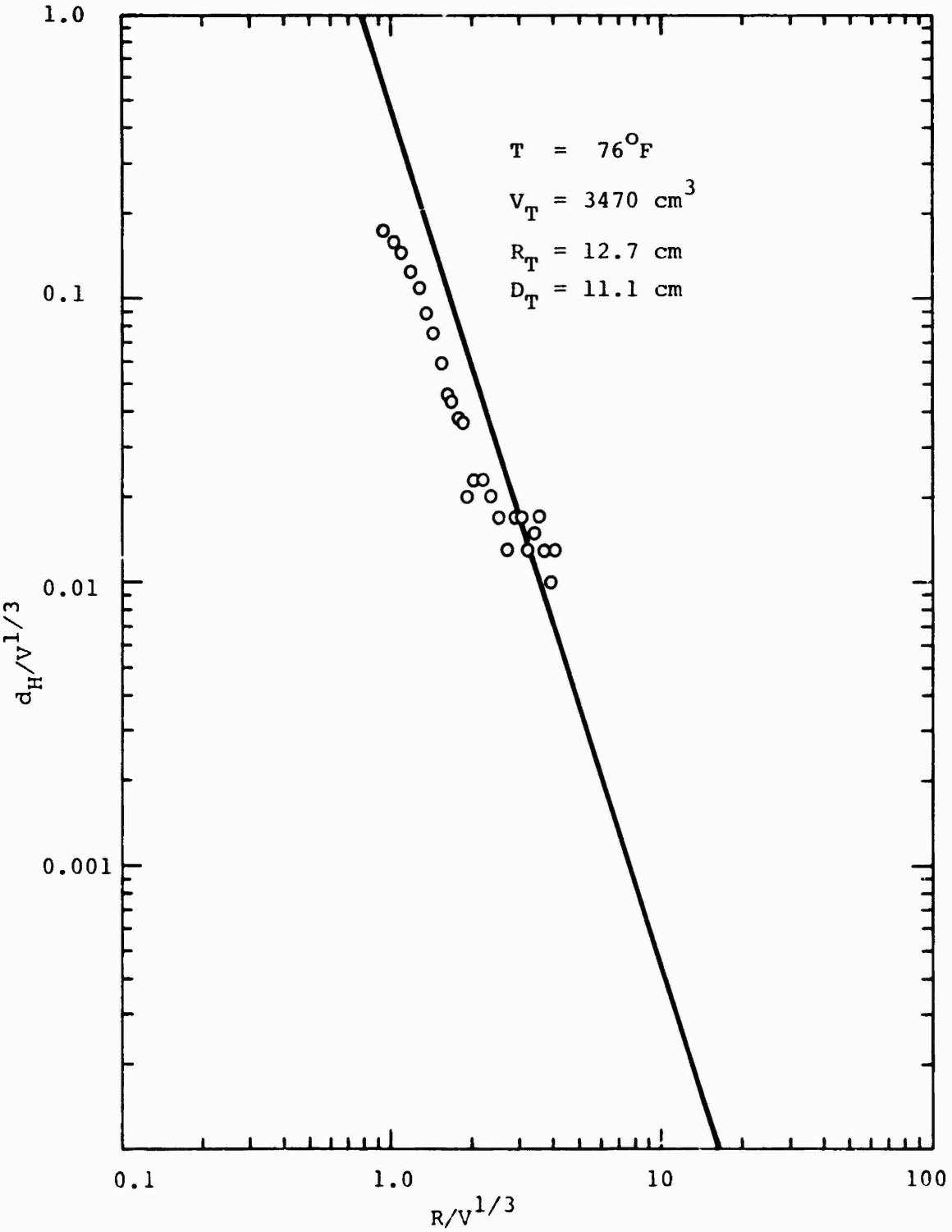

Figure A-16 Shot Z-C2, surface horizontal displacement versus range (both scaled by cube root of crater volume) in plasticene 2-in.-diam surface tangent, C-4 sphere.

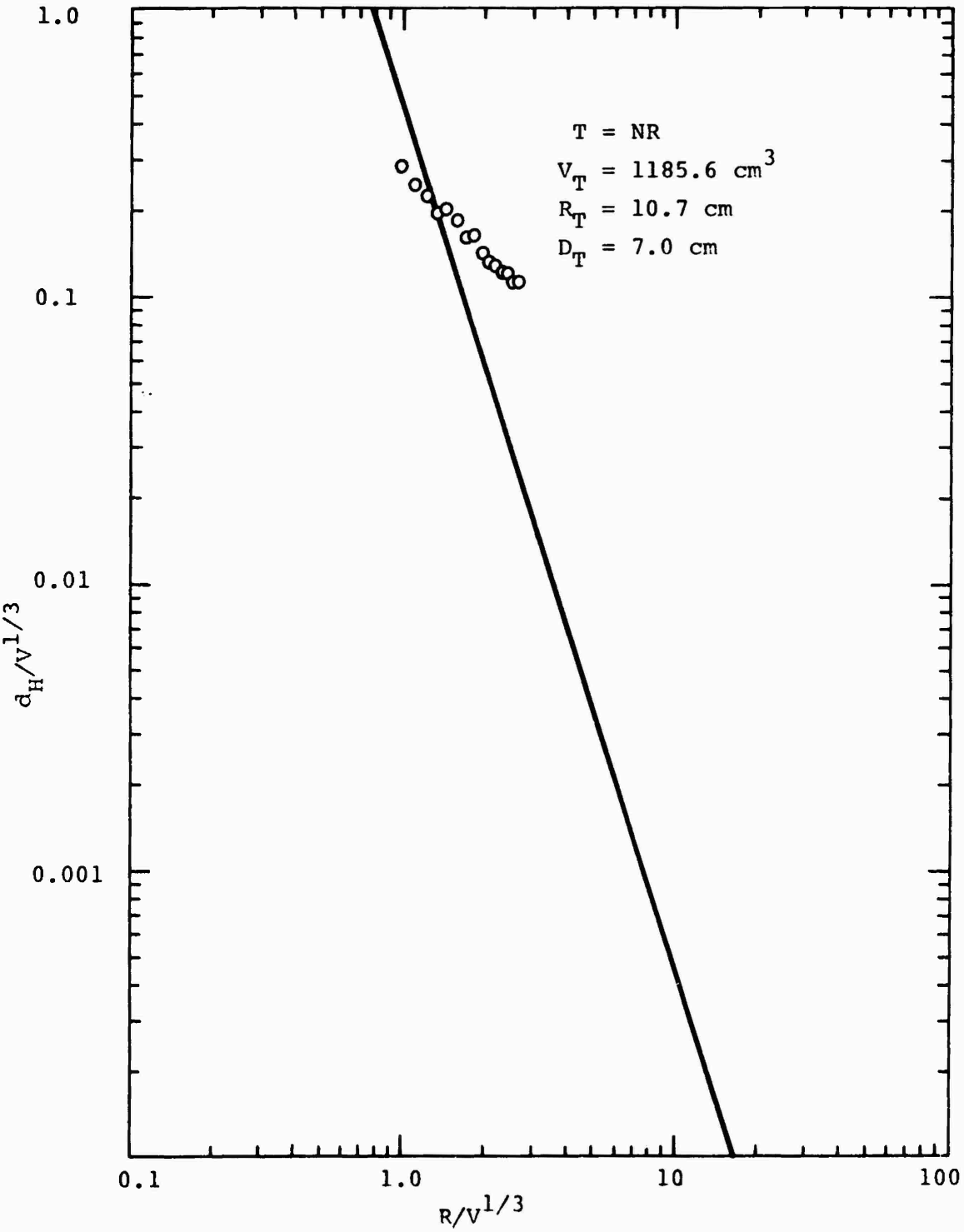

Figure A-17 Shot Z-C3, surface horizontal displacement versus range (both scaled by cube root of crater volume) in plasticene elevated 1 radius.

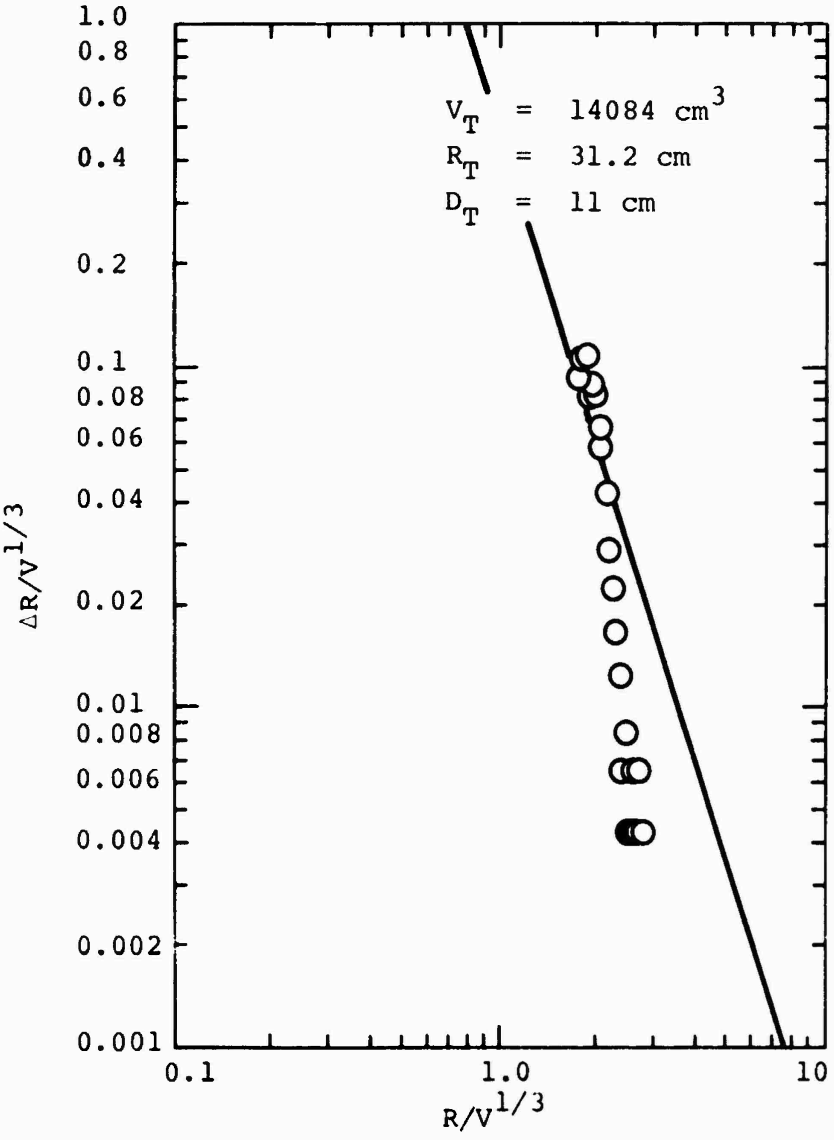

Figure A-18 Shot Z-S1, surface horizontal displacement versus range (both scaled by cube root of crater volume) in sand 2-in. diameter C-4 explosive sphere placed tangent to surface.

TABLE A1

SUMMARY OF EXPERIMENTAL TEST RESULTS

Test material	Shot name	Clay temp. (°F)	R_{HE} (inches) HE radius	HOB/R_{HE}	R_c (cm) Crater radius	D_c (cm) Crater depth	R_c/D_c	V_c (cm^3) Crater volume	M_e (gm) Ejecta mass	M (gm) Lip upthrust mass	Length scale factor(d)	Scaled to R_{HE} = 1 cm: R_c' (cm)	D_c' (cm)	V_c' (cm^3)	M_e' (gm)	M' (gm)	$M_e'+M'$ (gm)	M_c' (gm)(e)
Clay	Z-C4	90	0.6875	0	14.2	13.8	1.03	5278	N/A	N/A	0.579	8.22	7.99	1024	N/A	N/A	N/A	1731
Clay	Z-C5	63.5	0.6875	0	10.7(b)	8.9	1.20	1716	N/A	N/A	0.579	6.20	5.15	333	N/A	N/A	N/A	563
Clay	Z-C6	76.5	0.6875	0	10.6(c)	10.2	1.04	2227	N/A	N/A	0.579	6.14	5.90	432	N/A	N/A	N/A	730
Clay	Z-C2	76	1.0	1	12.7	11.1	1.14	3470	N/A	N/A	0.3945	5.01	4.38	213	N/A	N/A	N/A	360
Clay	Z-C7	76	1.25	2	11.2	9.0	1.24	1963	N/A	N/A	0.3153	3.53	2.84	61.5	N/A	N/A	N/A	104
Clay	Z-C3	(a)	1.25	2	10.7	7.0	1.53	1186	N/A	N/A	0.3153	3.37	2.21	37.2	N/A	N/A	N/A	63
Sand	Z-S1	N/A	1.0	1	31.2	11.0	2.84	14084	N/A	N/A	0.3945	12.31	4.34	865	N/A	N/A	N/A	1323
Clay	Crady 20	55	0.6875	0	9.2	8.2	1.12	1164	1121	624	0.579	5.33	4.75	226	218	121	339	382
Clay	Crady 19	60	1.0	1	10.2	7.8	1.31	1509	951	709	0.3945	4.02	3.08	92.6	58.4	43.5	102	156
Clay	Crady 21	56	1.25	2	7.7	3.4	2.26	815	57	284	0.3153	2.43	1.07	25.5	1.79	8.9	26.9	43

(a) Not recorded
(b) Reported incorrectly in PIFR-388-2 as 12.2
(c) Reported incorrectly in PIFR-388-2 as 12.4
(d) Includes small correction for detonator
(e) Scaled crater displaced mass $M_c' = V_c' \times \rho_o$ (where ρ_o = 1.69 gm/cm^3 for clay and 1.53 gm/cm^3 for sand)

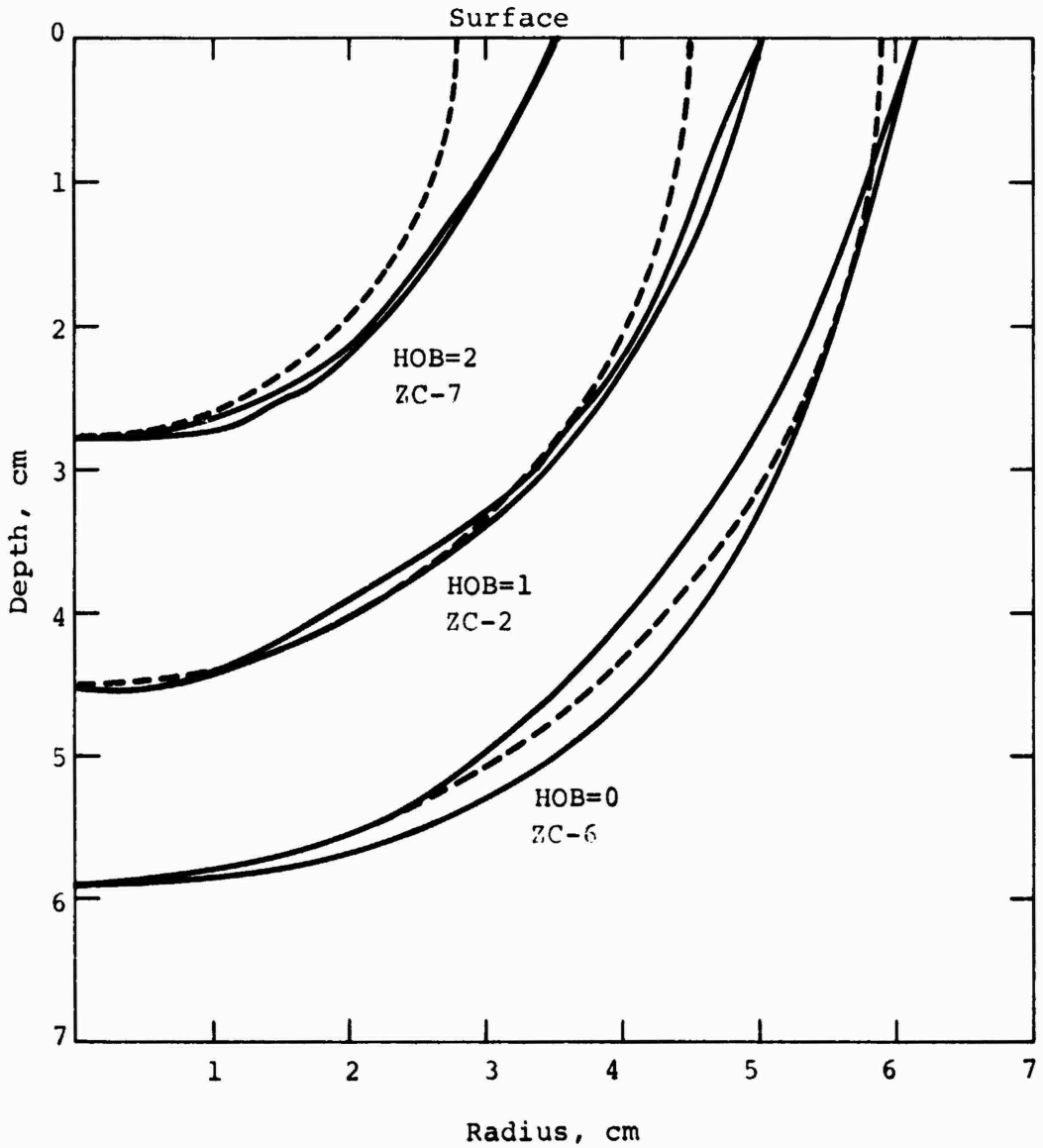

Figure A-19 Two scaled experimental sections (each) for plasticene shots ZC-6, ZC-2 and ZC-7.

69. The dashed circles show the nearly spherical shapes. The differences in the crater sections of the same experiment suggest an experimental nonreproducibility of about 0.1 cm in the "scaled" data.

1.2 CRATER EJECTA GROWTH TESTS

A second test series was performed to examine the growth of the crater ejecta "splash" and the corresponding crater lip. Independently triggered, 30 kV flash X-ray units were used to obtain time-resolved radiographs of the growth of the crater lip. Since only three X-ray units were available, the time-resolved series is necessarily constructed from successive tests. Care was taken to insure that the test bed was in the same configuration for each successive test. Fresh sand and clay were used for each shot, and the temperature of the sand was monitored to insure the equivalent temperature for each shot.

Figures A20, A21, and A22 show the sequential, time-resolved radiographs of the growth of the ejecta. Two test series were conducted in the plasticene test bed; one series was conducted in the sand test bed. The wires observable in the radiographs are electrical leads to the detonators.

Figure A23 is a graph of the minimum diameter of the ejecta "splash" versus time. The values plotted have been scaled down to match the ELK 66, 67, and 69 calculations. Table A2 tabulates the results of this experimental series, as well as the scaled-down values. It is interesting to note that the curves of the ejecta "splash" for the two tangent tests fall quite closely to each other, even though the material properties are significantly different. This observation implies a scalability of crater growth for scaled HOB geometry before strength effects appear at later times. This point is supported by computational data that will be reported later.

1-3/8-inch diameter sphere of C-4 explosi
plasticene clay

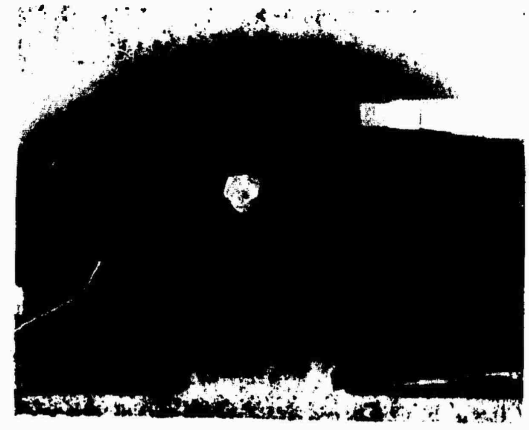

25 μsec after ZT

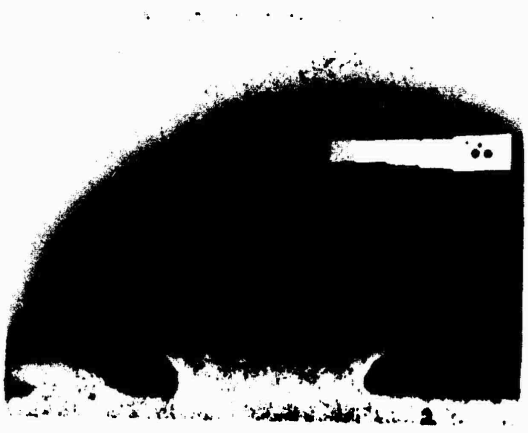

50 μsec after ZT

300 μsec after ZT

400 μsec after ZT

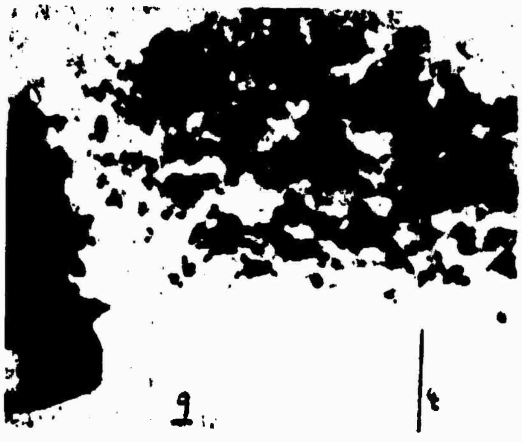

3000 μsec after ZT

5000 μsec after ZT

Figure A20 Sequential flash radiographs of crater ejecta formation in plasticene.

iameter sphere of C-4 explosive, half buried in
lay

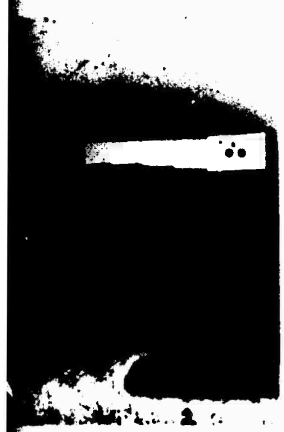

fter ZT

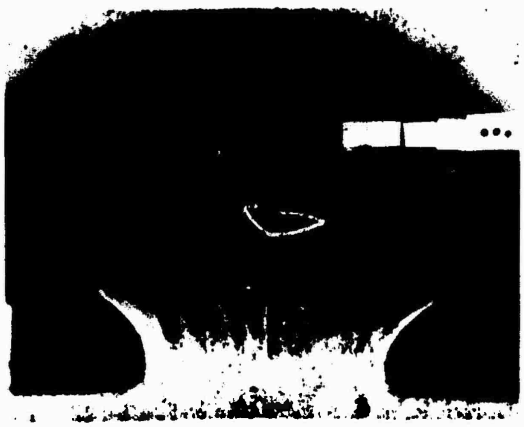

100 μsec after ZT

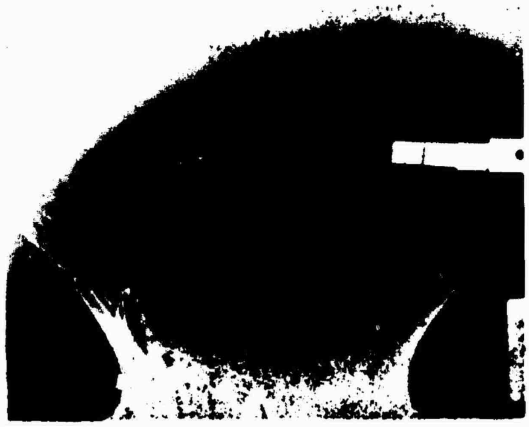

200 μsec arter ZT

after ZT

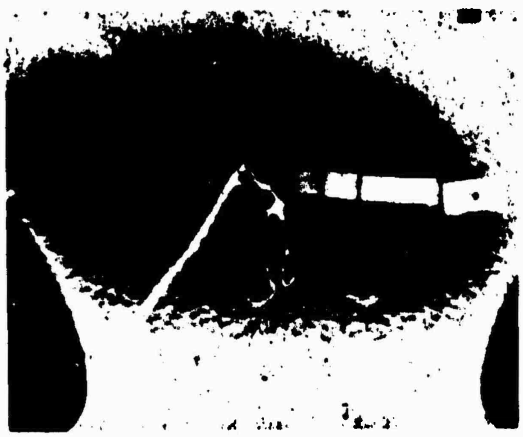

500 μsec after ZT

1000 μsec arter ZT

ec after ZT

r ejecta

2-inch diameter sphere of C-4 explosive,
plasticene clay

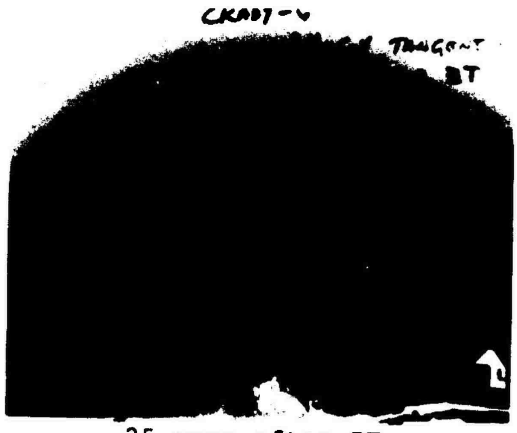

25 μsec after ZT

50 μsec after ZT

300 μsec after ZT

400 μsec after ZT

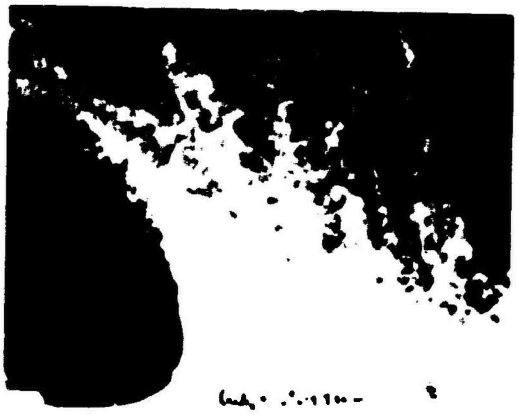

1000 μsec after ZT

3000 μsec after ZT

re of C-4 explosive, tangent to surface of

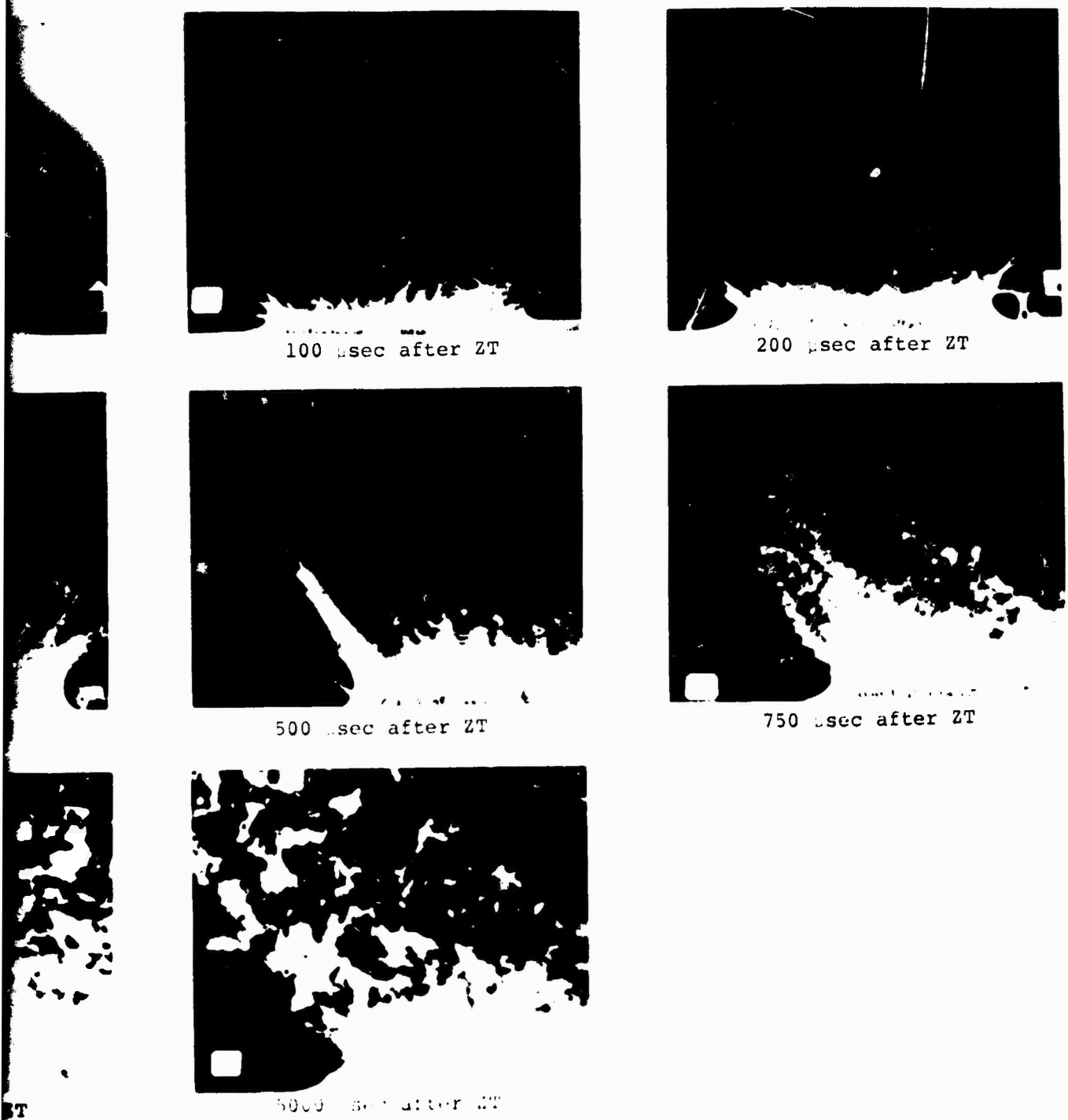

Figure A.1 Sequential flash radiographs of crater ejecta formation in plasticene.

25 μsec after ZT

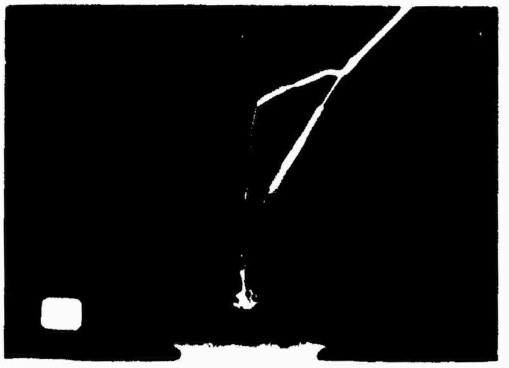

50 μsec after ZT

300 μsec after ZT

400 μsec after ZT

3000 μsec after ZT

500 μsec after ZT

Figure A22 Sequential flash radiographs of crater ejecta formation in sand.

sphere of C-4 explosive, tangent to surface, in sand

after ZT

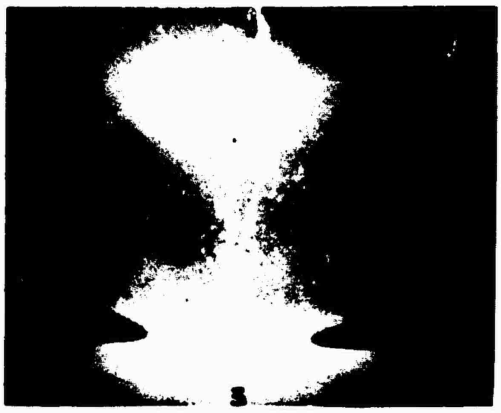

100 μsec after ZT

200 μsec after ZT

after ZT

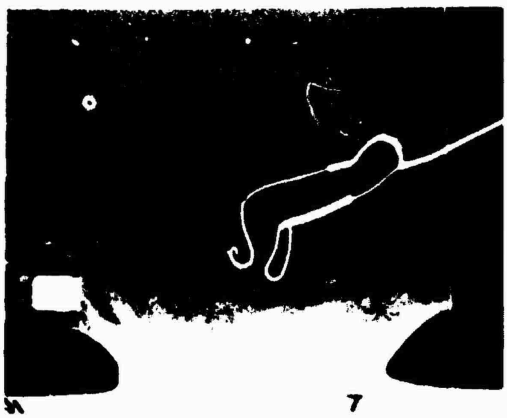

500 μsec after ZT

1000 μsec after ZT

after ZT

10,000 μsec after ZT

15,000 μsec after ZT

ejecta

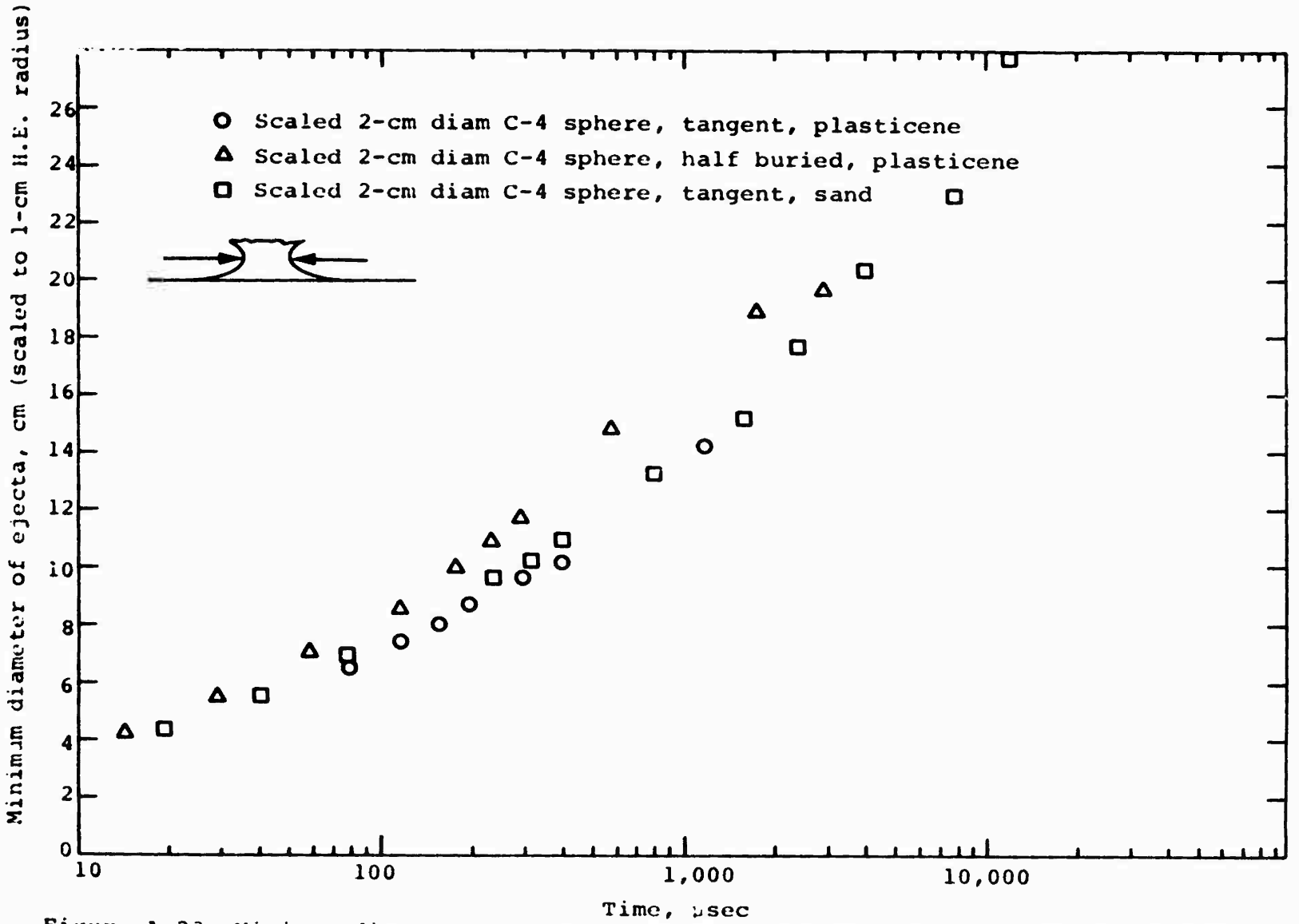

Figure A-23 Minimum diameter of ejecta "splash" versus time for three experiments.

TABLE A2

EXPERIMENTAL OBSERVATION OF CRATER EJECTA GROWTH FROM FLASH RADIOGRAPHS

Time (μsec)	1. 2-inch Diam C-4 Sphere Tangent to Surface, in Plasticene		2. 1-3/8-inch Diam C-4 Sphere Half Buried in Plasticene		3. 1-inch Diam C-4 Sphere, Tangent to Surface, in Sand		Scaled 2-cm Diam C-4 Sphere(a) Tangent to Surface in Plasticene				Scaled 2-cm Diam C-4 Sphere (b) Half-Buried in Plasticene				Scaled 2-cm Diam C-4 Sphere (c) Tangent to Surface in Sand			
	Minimum Diam of Ejecta (cm)	Height of Minimum Above Ground Zero (cm)	Minimum Diam of Ejecta (cm)	Height of Minimum Above Ground Zero (cm)	Minimum Diam of Ejecta (cm)	Height of Minimum Above Ground Zero (cm)	Scale* Factor	Time (μsec)	Minimum Diam of Ejecta (cm)	Height of Minimum Above Ground Zero (cm)	Scale* Factor	Time (μsec)	Minimum Diam of Ejecta (cm)	Height of Minimum Above Ground Zero (cm)	Scale* Factor	Time (μsec)	Minimum Diam of Ejecta (cm)	Height of Minimum Above Ground Zero (cm)
25	Not sufficiently formed		7.13	.77	5.6	0.15	0.3945				0.579	14.5	4.24	0.45	0.789	19.7	4.4	0.12
50	Not sufficiently formed		9.63	0.97	7.1	0.30	0.3945				0.579	29.0	5.58	0.56	0.789	39.5	5.6	0.24
100	Not sufficiently formed		12.27	1.67	8.7	0.57	0.3945				0.579	57.9	7.10	0.97	0.789	78.9	6.9	0.45
200	16.6	1.33	14.93	1.87	10.3	0.63	0.3945	78.9	6.55	0.52	0.579	115.8	8.64	1.08	0.789	157.8	8.1	0.50
300	19.0	1.63	17.3	2.37	12.3	0.73	0.3945	118.4	7.50	0.64	0.579	173.7	10.02	1.37	0.789	236.7	9.7	0.58
400	20.4	1.63	19.1	2.77	12.9	0.87	0.3945	157.8	8.05	0.64	0.579	231.6	11.06	1.60	0.789	315.6	10.2	0.69
500	22.5	2.52	20.3	3.13	14.0	1.00	0.3945	197.3	8.88	0.99	0.579	289.5	11.75	1.81	0.789	394.5	11.0	0.79
750	24.5	1.80	N/A	N/A	N/A	N/A	0.3945	295.9	9.67	0.71	0.579							
1000	25.9	3.80	25.7	3.87	16.9	1.03	0.3945	394.5	10.22	1.50	0.579	579	14.88	2.24	0.789	789	13.3	0.81
2000	N/A	N/A	N/A	N/A	19.3	1.80	0.3945				0.579					1578	15.2	1.42
3000	36.3	2.50	32.8	3.27	22.4	2.47	0.3945	1183.5	14.32	0.99	0.579	1737	19.0	1.89	0.789	2367	17.7	1.95
5000	Ejecta broken up	N/A	34.0	Ground level not visible	25.8	3.20	0.3945				0.579	2895	19.69		0.789	3945	20.4	2.52
10,000	N/A	N/A	N/A	N/A	29.13	2.53	0.3945				0.579				0.789	7890	23.0	2.00
15,000	N/A	N/A	N/A	N/A	35.4	3.17	0.3945				0.579				0.789	11,835	27.9	2.50
20,000	N/A	N/A	N/A	N/A	38.7	Ground level not visible	0.3945				0.579				0.789	15,780	30.5	

*Includes small correction for detonator

(a) Scaled from case 1.
(b) Scaled from case 2.
(c) Scaled from case 3.

1.3 CRATER EJECTA MASS TESTS

The final experimental test series was conducted to examine the actual mass of ejecta excavated from the test media during explosive cratering. To accomplish this, a method was developed that allowed an 18-inch-diameter plasticene hemisphere of known weight to be lowered into a prepared receptacle in the plasticene test bed. The shot was fired, and the hemisphere with crater was then removed and reweighed to determine mass loss. Figure A24 shows the receptacle ready for the hemisphere of plasticene. Figure A25 shows the plug in place and a half-buried shot ready for firing. The results of this test series are shown in Table A3.

TABLE A3

RESULTS OF EJECTA MASS EXPERIMENTS

Shot	Clay Temperature (^{o}F)	Configuration	Crater Volume (cm^3)	Ejecta Mass (gm)
CRADY-19	60	2-in. C-4 sphere tangent to surface	1509	951
CRADY-20	55	1-3/8-in. C-4 sphere 1/2 buried	1164	1121
CRADY-21	56	2-1/2-in. C-4 sphere elevated 1-1/4-in. above surface of clay	815	57

Three plasticene cratering experiments to measure ejected mass were relevant to the data base for prediction purposes. The results scaled down to the ELK 66, 67, and 69 calculations size are shown in Table A4.

Figure A24 Hemispherical receptacle in plasticene test bed coated with a thin layer of Adiprene L-100 as a mold release.

Figure A25 Hemispherical clay in place in receptacle, 1-3/8-inch-diameter C-4 sphere half buried in plasticene and ready for shot.

TABLE A4

SCALED PLASTICENE EJECTA RESULTS

Scaled Quantity	Shot Crady-20	Shot Crady-19	Shot Crady-21
HOB (cm)	0	1	2
Crater radius (cm)	5.3	4.0	2.4
Crater depth (cm)	4.7	3.1	1.1
Crater volume (cm^3)	226	92.6	25.5
Ejecta mass (grams)	218	58.4	1.79
Lip mass (grams)	121	43.5	8.90
Clay temperature (^oF)	55	60	56

It is unfortunate that the three shots of Table A4 were not at the same temperature. However, the combined data of Tables A1 and A4 afford a means of performing reasonable interpolations to relate data at a common temperature (hence at a common material strength) for comparisons to the computed data base.

APPENDIX B
STREAM TUBE ENERGY BALANCE EQUATIONS

MATERIAL STRENGTH MODEL

Although the strain field is prescribed by the steady state flow model, the distortional energies also depend on the material model. It was necessary to approximate real materials with a constant shear modulus, μ, and a constant von Mises yield stress, Y, in order to proceed.

Typical values of Y/μ vary from about 0.012 to 0.0013 going from aluminum, through Westerly granite and mild steel, to plasticene clay. Therefore, the approximation $Y/\mu \ll 1$ was used to eliminate small terms in various expressions.

The yield stress, Y, was used to limit the second invariant of stress deviation $\sqrt{3J_2'}$ in the plastic domain. Although the stress deviators were different in the axis and radius stream tubes, the values of $\sqrt{3J_2'}$ differed only a few percent at corresponding points. Therefore, the axis tube expressions for the plastic-elastic transition radius, R_*, and the plastic and elastic distortional energy densities, η_P and η_E, can be applied in both tubes with little error.

PLASTIC-ELASTIC TRANSITION RADIUS, R_*

The plastic-elastic transition radius, R_*, was expressed as a function of R_c.

$$\left[R_c/R_*\right]^{Z+1} = 1 - \exp\left|-\left(\frac{Z+1}{3Z}\right)\right|\frac{Y}{\mu}$$

Applying $Y/\mu \ll 1$, the result is

$$R_*/R_c = \left[\left(\frac{3Z}{Z+1}\right)\frac{\mu}{Y}\right]^{1/(Z+1)} \qquad \text{(B-1)}$$

which has values ranging from about 6 to 12 for Z = 2 (contained bursts) and from about 4 to 6 for Z = 3 (typical surface burst average value).

DISTORTIONAL ENERGY DENSITIES AND INTEGRALS

The plastic and elastic distortional energy densities η_P and η_E can be evaluated when Y and μ are constant. Using the approximation $Y/\mu \ll 1$, the results are

$$\eta_E(R \leq R_*) = Y^2/(6\mu)$$

$$\eta_P(R \leq R_*) = -Y^2/(3\mu) - \frac{ZY}{(Z+1)} \ln\left[1 - (R_c/R)^{Z+1}\right]$$

$$\eta_E(R_* \leq R) = \frac{ZY}{2(Z+1)} \left(\frac{3Z}{Z+1}\right) \frac{\mu}{Y} (R_c/R)^{2(Z+1)}$$

$$\eta_P(R_* \leq R) = 0$$

The stream tube volume element is $A_o R^Z\, dR$ where A_o is the cross sectional area at unit range. The distortional energies contained between R_1 and R_2 in a stream tube with $A_o = 1$ are

$$\int_{R_1}^{R_2} \eta_E(R \leq R_*) R^Z dR = \frac{YZ}{2(Z+1)^2} \left(\frac{Z+1}{3Z}\right) \frac{Y}{\mu} \left[R_2^{Z+1} - R_1^{Z+1}\right]$$

$$\int_{R_1}^{R_2} \eta_E(R_* \leq R) R^Z dR = \frac{YZ}{2(Z+1)^2} \left(\frac{3Z}{Z+1}\right) \frac{\mu}{Y} R_c^{2(Z+1)} \left[\frac{1}{R_1^{Z+1}} - \frac{1}{R_2^{Z+1}}\right]$$

$$\int_{R_1}^{R_2} \eta_P(R \leq R_*) R^Z dR = -\frac{YZ}{(Z+1)^2} \left(\frac{Z+1}{3Z}\right) \frac{Y}{\mu} \left[R_2^{Z+1} - R_1^{Z+1}\right]$$

$$- \frac{YZ}{(Z+1)^2} R_c^{Z+1} \left\{\left[\left(\frac{R_2}{R_c}\right)^{Z+1} - 1\right] \ln\left[1 - \left(\frac{R_c}{R_2}\right)^{Z+1}\right] + \ln\left(\frac{R_c}{R_2}\right)^{Z+1}\right.$$

$$\left. - \left[\left(\frac{R_1}{R_c}\right)^{Z+1} - 1\right] \ln\left[1 - \left(\frac{R_c}{R_1}\right)^{Z+1}\right] - \ln\left(\frac{R_c}{R_1}\right)^{Z+1}\right\}$$

AXIS TUBE KINETIC, GRAVITATIONAL, AND DISTORTIONAL ENERGIES

The kinetic, gravitational, and distortional energies in the axis stream tube are given by integrals of the form

$$A_o \int_{R_c}^{\infty} f(R)\, R^Z dR$$

The results are given below.

$$KE_{axis}/A_o = R_c^{1-Z} \frac{\rho\alpha^2}{2(Z-1)} \tag{B-2}$$

$$GE_{axis}/A_o = R_c^{Z+2} \frac{\rho g}{(Z+2)} \tag{B-3}$$

$$DE_{axis}/A_o = R_c^{Z+1} \frac{YZ}{(Z+1)^2} \left\{ 1 + \ell n \left[\frac{3Z}{Z+1} \frac{\mu}{Y} \right] \right\} \tag{B-4}$$

$$\cong R_c^{Z+1} \frac{YZ}{(Z+1)^2}\, 6 \tag{B-4a}$$

The logarithm term of Eq. (B-4) varies by about ±20 percent for common materials. It is replaced by the average value of 5 to obtain the Eq. (B-4a) approximation.

RADIUS TUBE KINETIC ENERGY

The radius tube kinetic energy is the same as that of the axis tube with correction terms involving R_c/RAD that cannot be evaluated unless Eqs. (11), (12), and (13) of Section 3, main text are iterated. However, since KE_{RAD} is used only in Eq. (11), it is sufficient to express the correction terms as functions of R_c^+/RAD. It can be shown that

$$\left(\frac{1}{2}\right)^{1/(Z+1)} \leq R_c^+/RAD \leq \left(\frac{1}{2}\right)^{1/(Z+2)}$$

with the lower limit corresponding to GE $\ll$ DE and the converse applying at the upper limit.

The correction terms were evaluated at these limits for values of Z = 2, 3, and 4 and it was found that KE_{RAD} (with $R_c \cong R_c^+$) could be approximated by

$$KE_{RAD} \cong 0.4\ KE_{axis} \left[1 + (Z - 2)^2\right] \qquad \text{(B-5)}$$

for application in Eq. (11) with a few percent error.

RADIUS TUBE GRAVITATIONAL ENERGY

The change in gravitational potential in the radius tube also contains terms involving R_c/RAD with values R_c^+/RAD applying in Eq. (11) and $R_c/RAD = 1$ applying in Eq. (13). Paralleling the KE_{RAD} procedure, the results are

$$GE_{RAD} = GE_{axis}\ f_{RAD} \quad \text{for Eq. (13)} \qquad \text{(B-6)}$$

$$GE_{RAD} = GE_{axis}\ f_{R_c^+} \quad \text{for Eq. (11)} \qquad \text{(B-7)}$$

where

$$f_{RAD} = \left(\frac{Z+2}{Z+1}\right)\left\{\left(\frac{1}{2}\right)^{1/(Z+1)}\left[1 - \left(\frac{1}{2}\right)^{(Z-2)/(Z+1)}\right] - \left(\frac{3}{2}\right)^{1/(Z+1)}\left[1 - \left(\frac{3}{2}\right)^{(Z-2)/(Z+1)}\right]\right\}$$

$$f_{R_c^+} \cong \left(\frac{17 - Z}{20}\right) f_{RAD} \qquad \text{(B-8)}$$

$$f_{R_c^+} \approx 0.7\ f_{RAD} \qquad \text{(B-9)}$$

Values of f_{RAD} are 0, 0.186, 0.315, 0.410, and 0.482, respectively for Z = 2, 2.5, 3, 3.5, and 4. The error in Eq. (B-8) is a few percent, rising to about 10 percent in the Eq. (B-9) approximation.

RADIUS TUBE DISTORTIONAL ENERGY

The plastic-elastic transition radius is well beyond the outer radius of the mass when $R_c^+ \leq R_c$ in the radius tube. As before, the results are the same as those of the axis tube with a correction that depends on the value of R_c/RAD. Using previous procedures, the results are

$$DE_{RAD} = 0.23\ DE_{axis} \qquad \text{for Eq. (13)} \qquad \text{(B-10)}$$

$$DE_{RAD} = 0.32\ DE_{axis} \qquad \text{for Eq. (11)} \qquad \text{(B-11)}$$

with a few percent error.

INTERIM SUMMARY

Let the subscripts i = 1,2 apply respectively to the axis and radius stream tubes and define the quantities

$$K_1 = \frac{\rho a^2}{2(Z-1)} \qquad K_2 = 0.4K_1\left[1 + (Z-2)^2\right]$$

$$G_1 = \frac{\rho g}{(Z+2)} \qquad G_2 = G_1\ f_{RAD} \text{ of Eq. (19)}$$

$$G_1' = G_1 \qquad G_2' = G_1\ f_{R_c^+} \text{ of Eq. (21) or (22)}$$

$$D_1 = \frac{YZ}{(Z+1)^2}\,6 \qquad D_2 = 0.23\ D_1$$

$$D_1' = D_1 \qquad D_2' = 0.32\ D_1$$

Equations (11), (12), and (13) give

$$R_c^+ = \left[\frac{K_i}{D_i' + R_c^+ G_i'}\right]^{1/(2Z)} \tag{B-12}$$

$$E_o = 2K_i/\left(R_c^+\right)^{Z-1} \tag{B-13}$$

$$R_f = \left[\frac{E_o}{D_i' + R_f G_i'}\right]^{1/(Z+1)} \tag{B-14}$$

where iterations are required to evaluate Eqs. (B-12) and (B-14) if the gravity term and strength term are comparable.

Equation (B-14) can be evaluated directly by employing the approximations $\langle D_i \rangle = 0.5(D_i + D_i')$ and $\langle G_i \rangle = 0.5(G_i + G_i')$ and writing Eq. (B-14) as

$$R_f = \left[\frac{2K_i \; R_f^{1-Z}}{\left(R_c^+/R_f\right)^{Z-1} \langle D_i \rangle + \left(R_c^+/R_f\right)^{Z-1} R_f \langle G_i \rangle}\right]^{1/(Z+1)}$$

The appropriate estimates of R_c^+/R_f are $\left(\frac{1}{2}\right)^{1/(Z+1)}$ and $\left(\frac{1}{2}\right)^{1/(Z+2)}$ respectively for the $\langle D_i \rangle$ and $\langle G_i \rangle$ terms.

The result is

$$R_f = \left[\frac{K_i}{\left(\frac{1}{2}\right)^{2Z/(Z+1)} \langle D_i \rangle + R_f \left(\frac{1}{2}\right)^{(2Z+1)/(Z+2)} \langle G_i \rangle}\right]^{1/(2Z)} \tag{B-15}$$